Modelling and optimisation of single junction strain balanced quantum well solar cells.

Submitted for the degree of PhD

Marianne Catherine Lynch

February 2008

Imperial College
London

Abstract

In an attempt to find the optimum number of wells for maximum conversion efficiency a pair of otherwise identical strain balanced samples, one containing 50 wells and the other 65 wells have been characterised. The 65 well sample is found to possess a lower predicted efficiency than the 50 well sample, suggesting that the optimum well number lies between these values.

Devices grown using tertiary butyl arsine (TBAs) are found to possess comparable conversion efficiencies to the control cells grown using arsine and slightly superior dark IV characteristics, indicating that TBAs may be substituted for arsine without loss of device efficiency.

It is proposed that the $n_1 = 1$ dark current of strain-balanced multi-quantum well (SB-MQW) solar cells is comprised of two components, one arising from recombination in the wells in addition to the Ideal Shockley current. Good agreement between the output of this model and experimentally determined intercepts of the $n_1 = 1$ dark currents is observed. The radiative dark current arising from recombination in the wells is found become increasingly dominant as the wells grow deeper.

Expressions for the strained bandgaps are derived. A value for the conduction band offset is determined using the difference in energy between the heavy and light hole exciton peaks in low temperature photocurrent scans and found to be 0.53±0.03.

An absolute calculation for the absorption coefficient is incorporated into the quantum efficiency model and values for the heavy and light hole in-planes masses are obtained. The

model is found to underestimate the level of absorption in the intrinsic region by an amount consistent with estimates of the magnitude of the reflection from the back surface. The conversion efficiency of a sample predicted using a modelling program is compared to an independently obtained value. Good agreement is observed between the two results.

Acknowledgements

First and foremost I would like to thank my supervisor, Professor Keith Barnham, for giving me the opportunity to do a PhD in his group and for being the most enthusiastic, inspirational and kindest supervisor anyone could wish for. Infinite thanks to Paul Stavrinou for his patience in explaining **k.p** theory to a neophyte, and for allowing me to use his MATLAB code for the work in Chapter 5 of this thesis. I'm also very grateful to Ian Ballard for his boundless wisdom in everything relating to practical experiments and lab apparatus. I'm greatly indebted to James Connolly for much useful discussion regarding SOL, FORTRAN and computer modelling in general. All of them have had the dubious pleasure of proof reading all or part of this thesis, thus saving me from future embarrassment. Also, I'd like to thank the EPSRC for funding me during my PhD and the C. R. Barber Trust for enabling me to go to a number of excellent conferences.

Thanks to all the past and present members of the Imperial College Quantum Photovoltaics group; Massimo, Amanda, Tom, Dave, Andreas, Dan, Markus, Ben and Rahul, and everyone in H724 for their companionship at lunchtimes and after work over the past three years.

I'm very grateful to John Roberts, Geoff Hill, Rob Airey and Cath Calder at the EPSRC Centre for III-V Technologies who grow and process the majority of the devices studied in this thesis. Also, huge thanks to Massimo Longo of the Istituto Nazionale per la Fisica della Materia, Parma, Italy for the opportunity to study his devices grown using tertiary butyl arsine.

Thanks to Bookham Laboratories for providing the TEMs in Chapter 5.

Thanks beyond measure to all at the Cardinal (especially Louise, Dr de Silva and Chris), all at Heatherwood (especially Dr Clifford, Dr Gall, Dr Saad and Helen Plenty), Dr Leach and Karen Paige for helping me through a difficult time.

Outside of university I'd like to thank Abi, Almudena, Andy, Beccy, Charlie, Emily, Mary, Mina, Rajvi and Tamsin for their friendship and support and especially thank Michelle, Danny, Emma and Fleur for being splendid flatmates.

Finally, I am hugely grateful to my parents; to my Father, for his unfailing love and support all through my long journey to becoming a doctor; and to my Mother, who sadly will never read this but remains always my first and best teacher. This thesis is dedicated to them both.

Contents

List of Figures

List of Tables

1 The growth of the PV market

1.1 The need for renewable energy sources

For many years the scientific community has speculated on the effect of the large volumes of carbon dioxide released into the atmosphere. Although there is not yet complete agreement on the environmental consequences of the large increases in CO_2 production seen in recent decades, evidence is mounting that the increase in global temperature caused by greenhouse gases is responsible for dramatic changes in weather patterns, including hurricanes and droughts, together with rising sea levels caused by the melting of the polar ice caps.

Many widely respected international companies and government bodies are now in agreement with the sentiments expressed in the Third Assessment Report of the Intergovernmental Panel on Climate Change, that there is increasing evidence that climate change and human activities are inextricably linked [1]. In 2005 the United Nations Framework Convention on Climate Change warned that "a new kind of climate change is now on the way, foreshadowing drastic impacts on people, economies and ecosystems" [2]. Additionally, Lord Browne (the CEO of BP), admitted at the Launch of the 2006 Statistical Review of World Energy that "in BP we don't believe we can ignore the mounting evidence, the weight of scientific opinion and the risks of a fundamental change in the Earth's climate" [3].

If this were insufficient motivation for trying to break our dependence on fossil fuels there is also the fact that these energy sources will eventually be exhausted. Clearly, if modern

rates of energy consumption are to be maintained we must seek to generate more power from less polluting and sustainable sources such as wind, hydroelectric and solar power.

A possible alternative to fossil fuels is nuclear fission. This is often considered to be a more environmentally viable option for power generation although considerable amounts of CO_2 are released in the mining and milling of uranium ore. There are several major obstacles to be overcome before nuclear power can become a safe and economically viable alternative to fossil fuels. Firstly, there is the problem of safely disposing of nuclear waste which will remain hazardous for many thousands of years to come. Also, nuclear power plants may become targets for terrorist attacks. However, one of the most compelling arguments against the use of nuclear power is economic, with the cost of safely decommissioning nuclear power plants often extremely high [4].

1.2 Photovoltaics

Photovoltaics (PV), the production of electricity from solar radiation, is both non-polluting and sustainable. Worldwide, the PV market has expanded rapidly over recent years, with a cumulative installed capacity of 2.6 GW achieved by the end of 2004 [5].

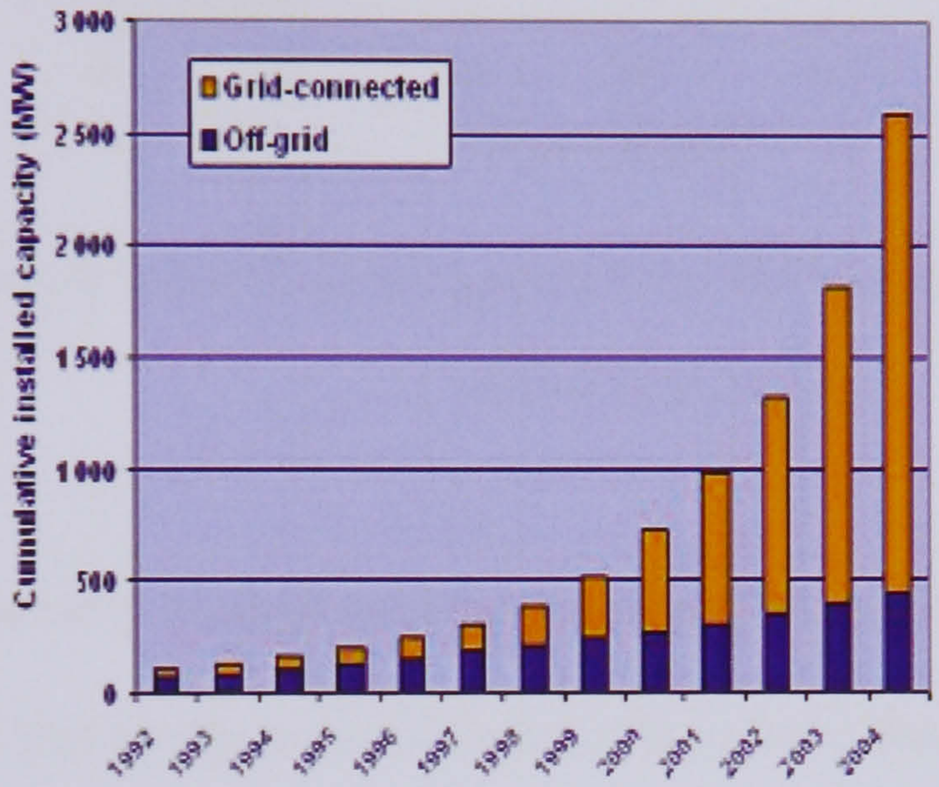

Figure 1.1: Growth of the worldwide PV market from 1992 to 2004 [5]

1.3 Economics of photovoltaics

Currently, commercially available photovoltaic systems are usually based on first generation devices. These devices are high efficiency photovoltaic cells such as monocrystalline silicon cells and have correspondingly high production costs of around US$3/Wpeak, significantly higher than that of electricity generated using conventional non renewable resources (estimated at US$1/W) [6].

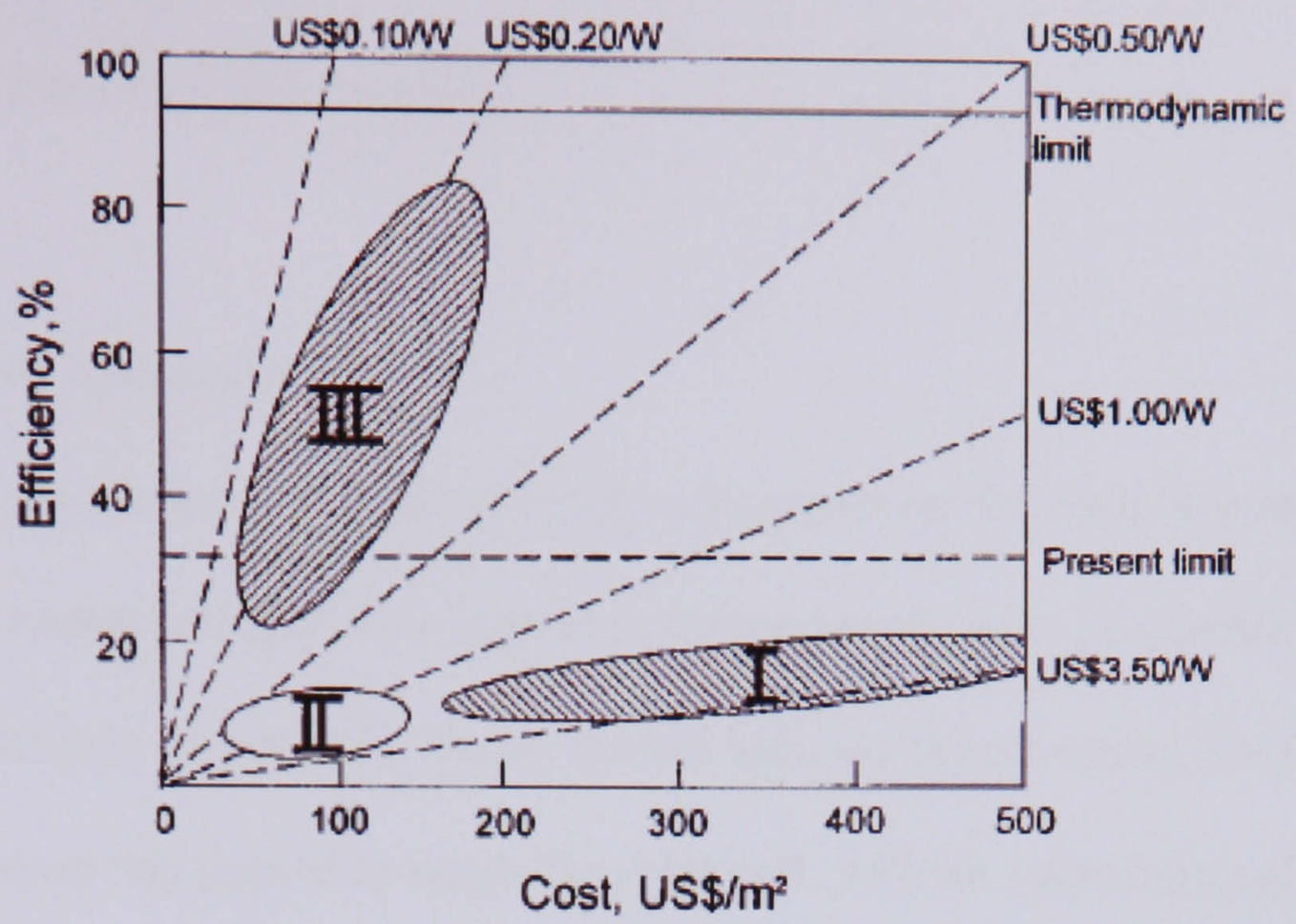

Figure 1.2: Conversion efficiency and cost for first, second and third generation photovoltaic devices [6]

The economic viability of photovoltaics may be increased by utilizing devices comprised of thinner cells and less costly materials even if they have somewhat lower conversion efficiencies - second generation devices such as thin film cells. However, the most advanced photovoltaic devices attempt to retain the low cost of second generation technologies while dramatically improving device efficiency by utilizing more sophisticated cell designs including multi-junction devices, hot carrier cells and intermediate bandgap devices.

This thesis focuses on quantum well solar cells, one of the most promising high efficiency cells belonging third generation PV. Such high efficiency cells are suitable for use in concentrator systems, where low cost optics are used in combination with small areas of photovoltaic devices, leading to a lower overall cost of energy production.

1.4 Introduction to Photovoltaics

1.4.1 The Solar Spectrum

Although the precise incident solar spectrum anywhere on the Earth's surface is affected by local weather conditions and atmospheric pollution levels, a set of standard spectra have been developed (see Figure 1.4). These spectra indicate the air mass (AM) through which the solar radiation has passed to reach the solar cell, with air mass being given by

$$AM = \sec(\theta) \tag{1.2}$$

where θ is the solar zenith angle [7]. Air mass 1.5 is normally used as the standard terrestrial spectrum.

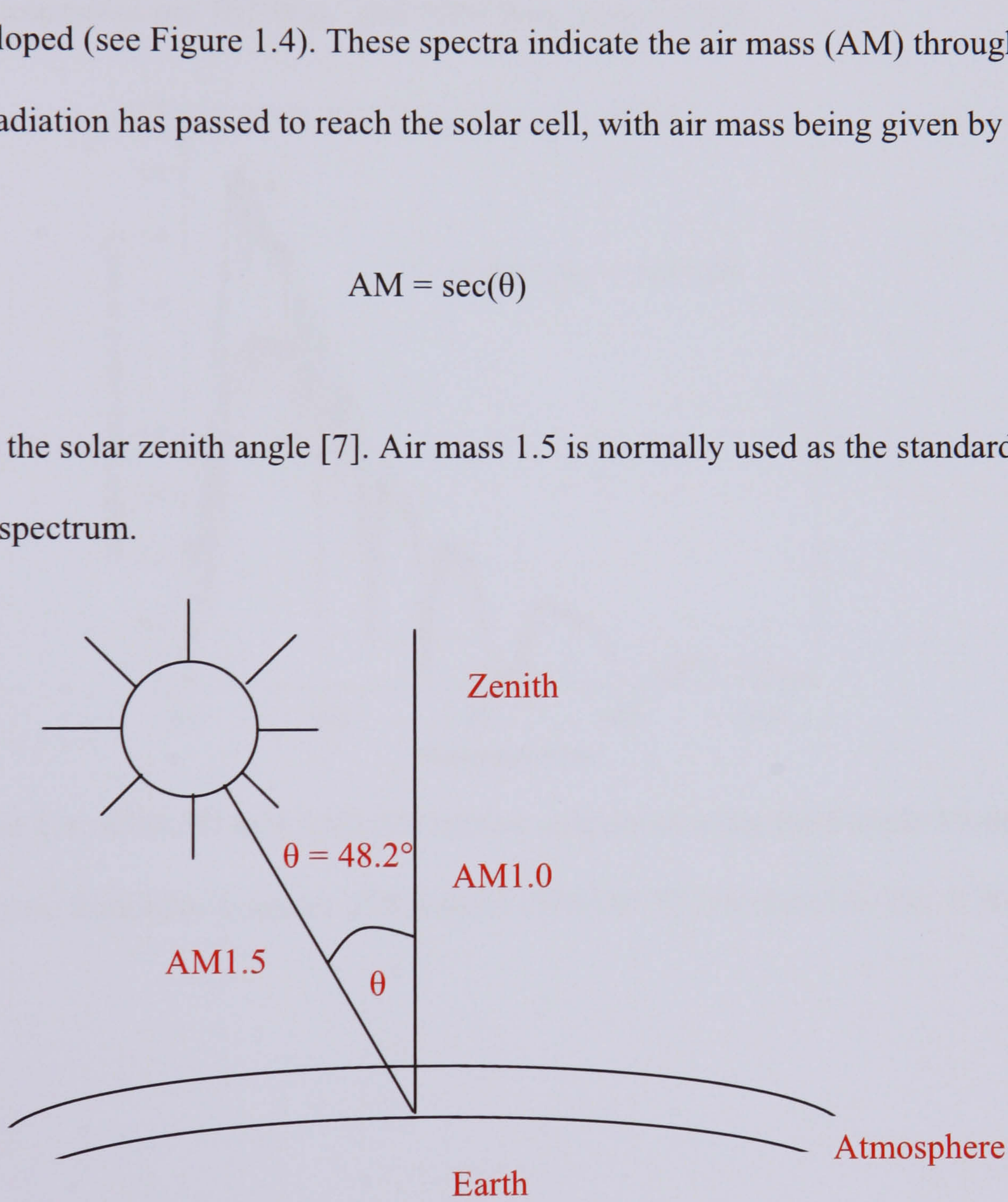

Figure 1.3: The solar zenith angle shown here for the AM1.5 spectrum

A particular spectrum may also be described as global or G, indicating a high proportion of diffuse radiation, or direct or D, indicating only normal incidence light is included in the spectrum. Direct spectra are commonly used in the modelling of concentrator systems as the optics in such systems are only capable of collecting a small amount of diffuse light [8]. The AM1.5D and AM1.5G spectra are usually defined such that the unconcentrated or "1 sun" light intensities are 767 Wm^{-2} and 1000 Wm^{-2} respectively.

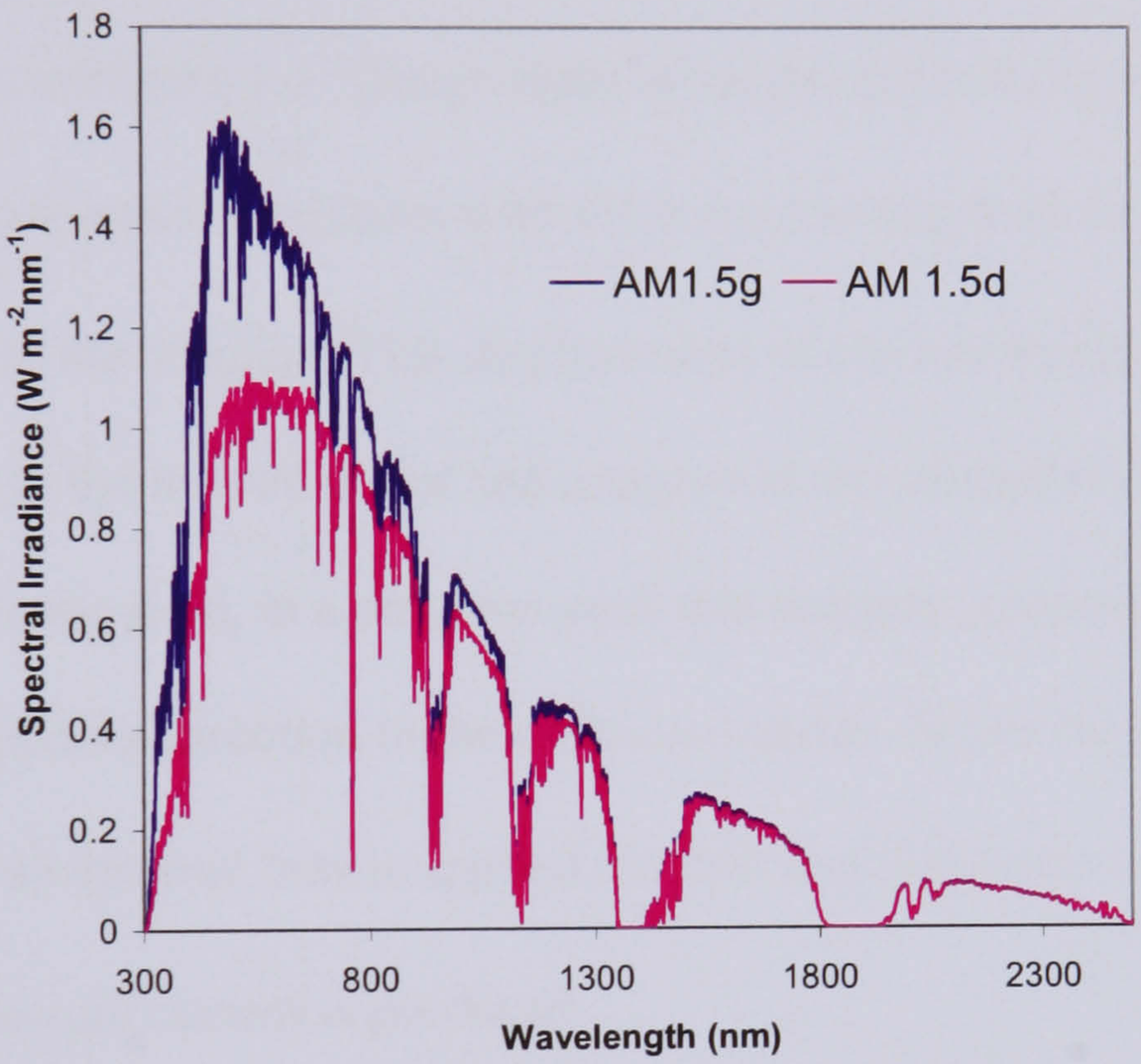

Figure 1.4: AM1.5G and AM1.5D spectra calculated using the Simple Model for Atmospheric Radiative Transfer of Sunshine (SMARTS) calculated by Dr. T. Tibbits [9]

1.5 The Physics of Solar Cells

1.5.1 The p-n junction

The simplest form of a photovoltaic device is a p-n homojunction, which consists of two layers of the same semiconductor that are oppositely doped. A band diagram of such a junction is shown in Figure 1.5. The gradient of carrier concentration causes majority carriers to diffuse across the junction with electrons moving from the n to the p region and holes from the p to the n region. This displacement of carriers leaves behind two layers of fixed charge due to the ionised donor and acceptor atoms around the junction. This gives rise to an electrostatic field, in a direction such that minority carriers drift across the junction in the opposite direction to the diffusion current. When the junction is at room temperature and no external bias is applied the drift and diffusion currents are in equilibrium and no net current is produced.

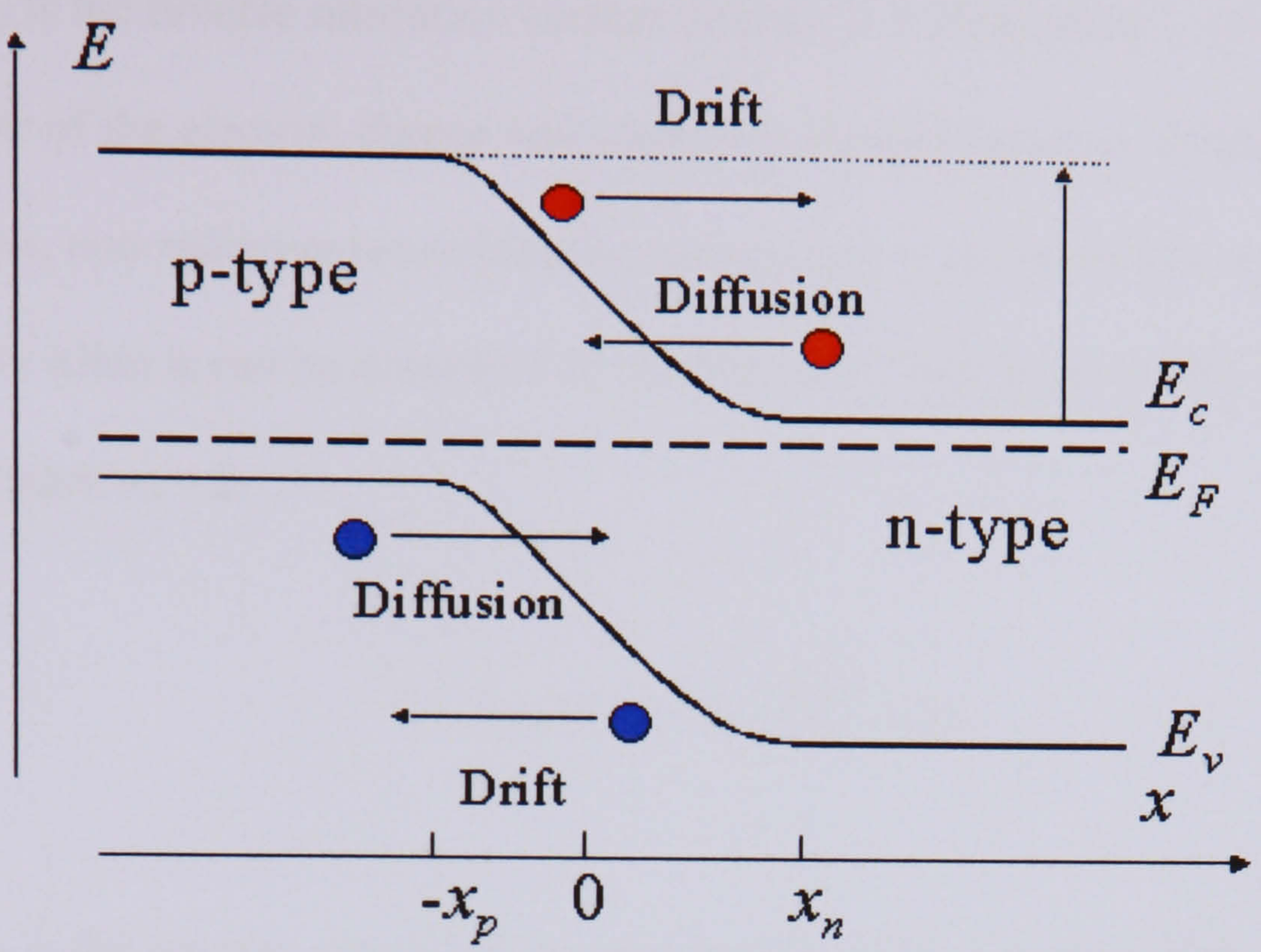

Figure 1.5: The pn junction under equilibrium. The conduction and valence bands are denoted by E_c and E_v respectively. The Fermi level is denoted by E_F and the depletion region extends from χ_n to $-\chi_p$ [8]

1.5.2 Dark Current

When the p-n junction is forward biased the electrostatic field within the junction is reduced, causing an increase in diffusion current such that the diffusion and drift currents are no longer equal. The net current produced is termed the dark current. In an ideal cell the only loss mechanism is the radiative or non-radiative recombination of injected minority carriers with majority carriers in the p and n regions (ideal Shockley behaviour). The dark current is then described by the Ideal Shockley equation.

$$J_{Ideal}(V) = J_{01}(e^{\frac{qV}{n_1 kT}} - 1) \qquad (1.3)$$

where J_{01} is the reverse saturation current density, k is Boltzmann's constant, q is the magnitude of the electron charge and where the ideality factor n_1, is unity [10]. However, in real diodes, non radiative recombination also occurs in the depletion region, often through trap levels when it can be described by the Shockley Hall Read (SHR) model, which has an ideality factor $n_2 \sim 2$.

$$J_{SHR}(V) = J_{02}(e^{\frac{qV}{n_2 kT}} - 1) \tag{1.4}$$

where J_{02} is the reverse saturation current density of the Shockley Hall Read current [11]. In a real solar cell the total dark current is the sum of the ideal and SHR currents

$$J_{dark}(V) = J_{01}(e^{\frac{qV}{n_1 kT}} - 1) + J_{02}(e^{\frac{qV}{n_2 kT}} - 1) \tag{1.5}$$

The dark current of a real solar cell is also affected by two kinds of parasitic resistances; series resistance (caused by resistance within the solar cell), and shunt resistance (caused by current leakage [14]). The effects of series and shunt resistance are illustrated in Figure 1.6 with shunt resistance observed at low voltages and series resistance observed at high bias.

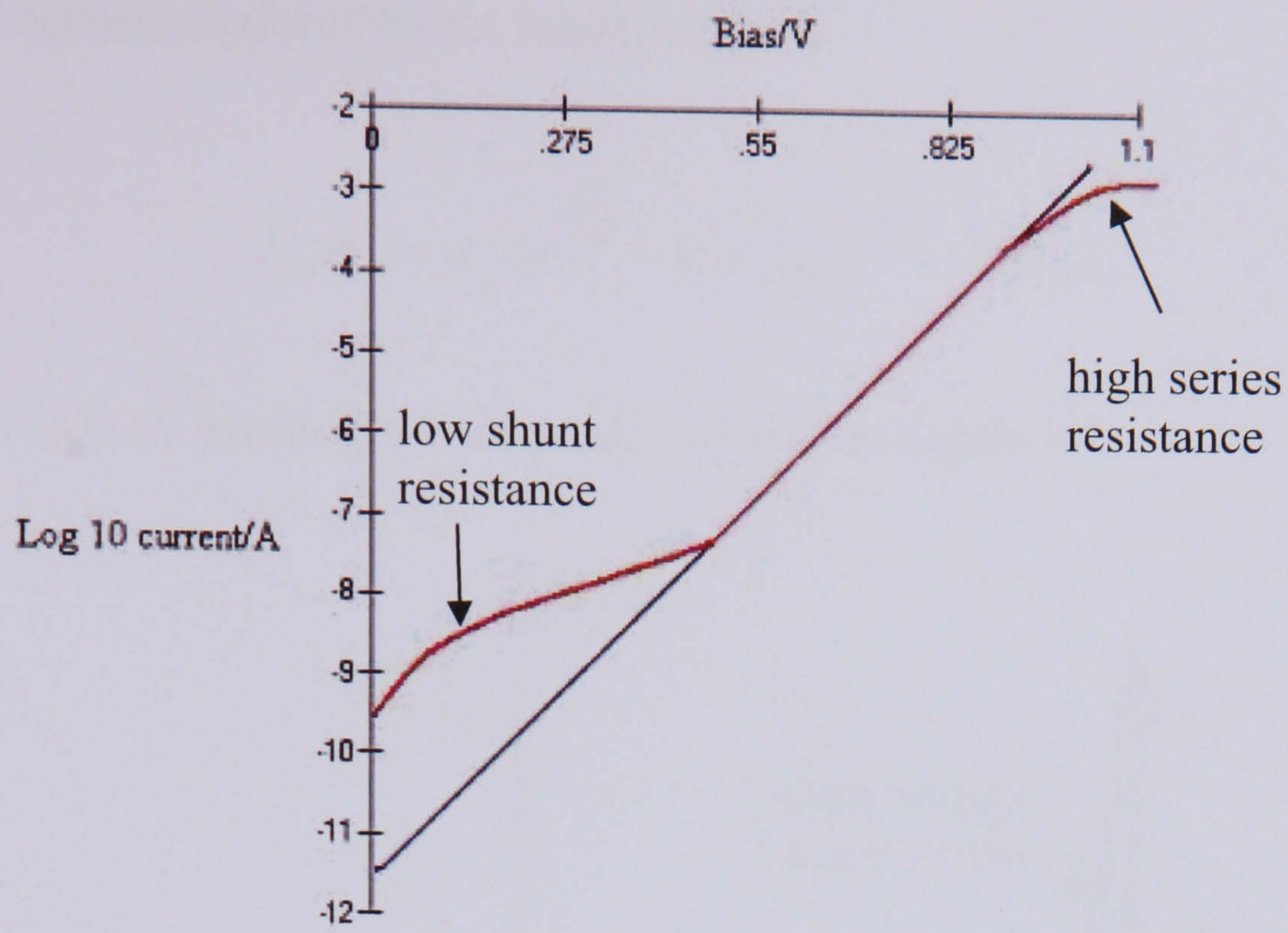

Figure 1.6: The dark IV curve for a real solar cell (red line) and an ideal device (blue line)

1.5.3 Photocurrent

When the junction is illuminated, incident photons with energy greater than E_g can excite electrons across the energy gap to the conduction band. The electrostatic field within the junction causes electrons to migrate. Minority carriers in p and n regions diffuse to the field region and these carriers produced in the depletion region drift to their respective majority carrier regions, thus creating a photo-generated current that acts in the opposite sense to the dark current. The photocurrent is dependent on the photon flux incident on the junction and quantum efficiency (the ratio of generated and collected electron-hole pairs to incident photons). The short circuit current density of the photo-generated carriers is given by

$$J_{sc} = |q| \int_{E_g}^{\infty} QE(E) b(E) dE \qquad (1.6)$$

where *QE(E)* is the quantum efficiency and *b(E)* is the incident photon flux [8].

The total current produced by the junction is now

$$J_{tot}(V) = J_{01}(e^{\frac{qV}{\eta_1 kT}} - 1) + J_{02}(e^{\frac{qV}{\eta_2 kT}} - 1) - J_{sc} \qquad (1.7)$$

A typical light IV profile for a solar cell is shown in Figure 1.7.

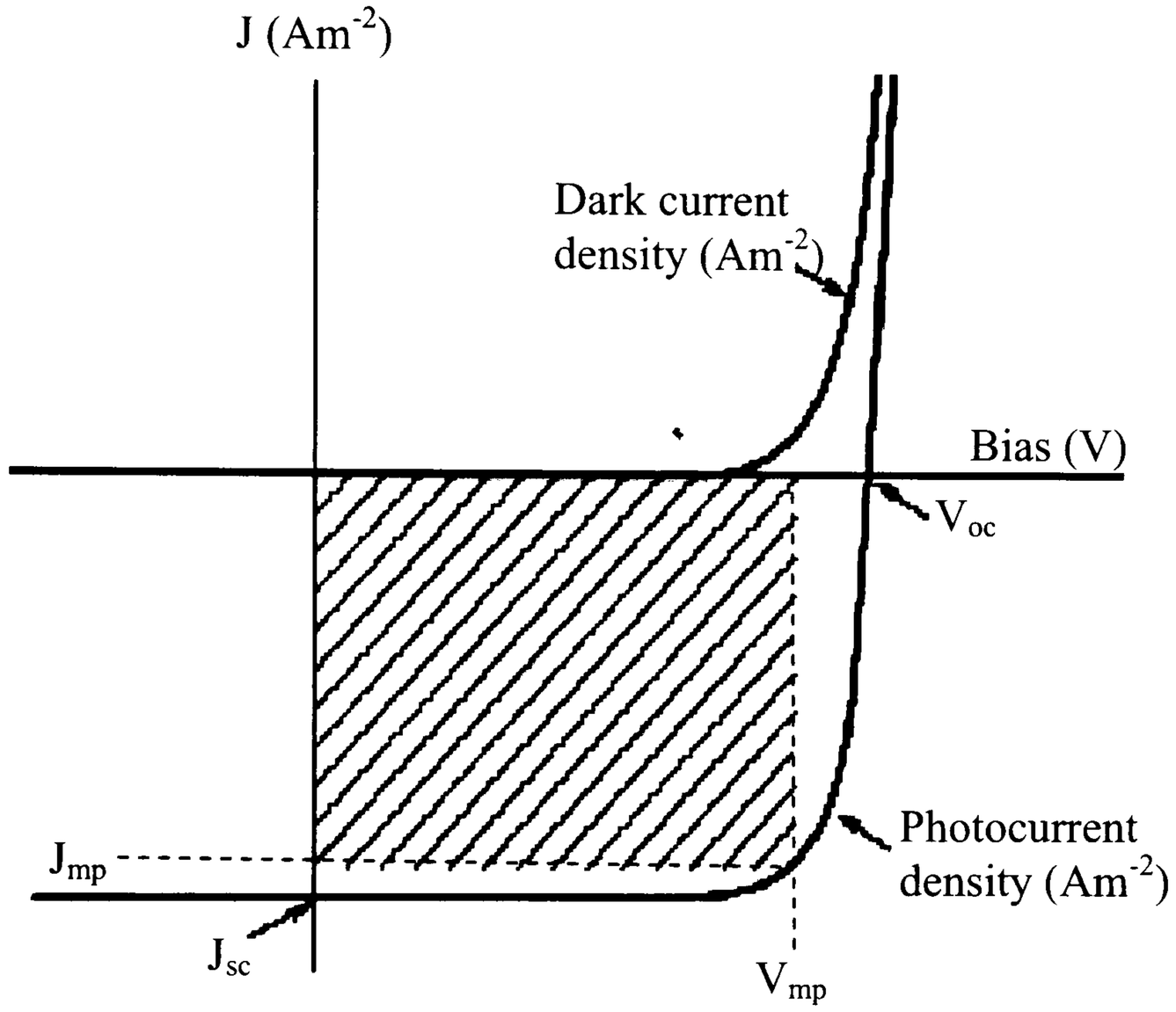

Figure 1.7: Light IV profile for a typical solar cell.

As indicated in Figure 1.7 the voltage at which the photocurrent is exactly cancelled by the dark current is termed the open circuit voltage (V_{oc}) and the current density and voltage corresponding to the greatest power output are named the maximum power voltage and current density (V_{mp} and J_{mp} respectively).

1.5.4 Cell Efficiency

The efficiency of a solar cell is simply the ratio of electrical power generated to the power incident on the device (P_{in}).

$$\eta = \frac{V_{mp} J_{mp}}{P_{in}} \tag{1.8}$$

The area of the maximum power rectangle that is covered by the IV profile is described by the fill factor (FF), which is given by

$$FF = \frac{V_{mp} J_{mp}}{V_{oc} J_{sc}} \tag{1.9}$$

and gives rise to an alternative form of Equation 1.8

$$\eta = \frac{FFV_{oc} J_{sc}}{P_{in}} \tag{1.10}$$

1.5.5 Effect of Band-gap on Cell Efficiency

The size of the band-gap of the material used to make a solar cell has a dramatic effect on the short circuit current and the dark current of the device. This is because, as the cell can only absorb photons with energies greater or equal to the bandgap, the smaller the bandgap of the cell the more photons can be absorbed and the greater J_{sc} will be. However, V_{oc} is also dependent on the size of the bandgap, due to the relationship between reverse saturation current and E_g

$$J_{01} \propto exp\left(\frac{-E_g}{n_1 kT}\right) \tag{1.11}$$

As stated in Equation 1.10, the overall efficiency of the cell is dependent on the product of J_{sc} and V_{oc}. For this reason it is necessary to compromise between a large band-gap material that produces a low J_{sc} and a high V_{oc} and a small band-gap material that has a low V_{oc} and large J_{sc}. The optimum band-gap for AM1.5 spectra has been calculated to be 1.18eV at 30 suns concentration [12]. The two material systems with band-gaps closest to this optimum value are InP and GaAs, which possess bandgaps of 1.34eV and 1.42eV respectively (see Figures (1.8 and 1.9). GaAs is generally used in solar cell fabrication in preference to InP because GaAs substrates are cheaper and less brittle and growth on GaAs is consistent with the even cheaper Ge substrates.

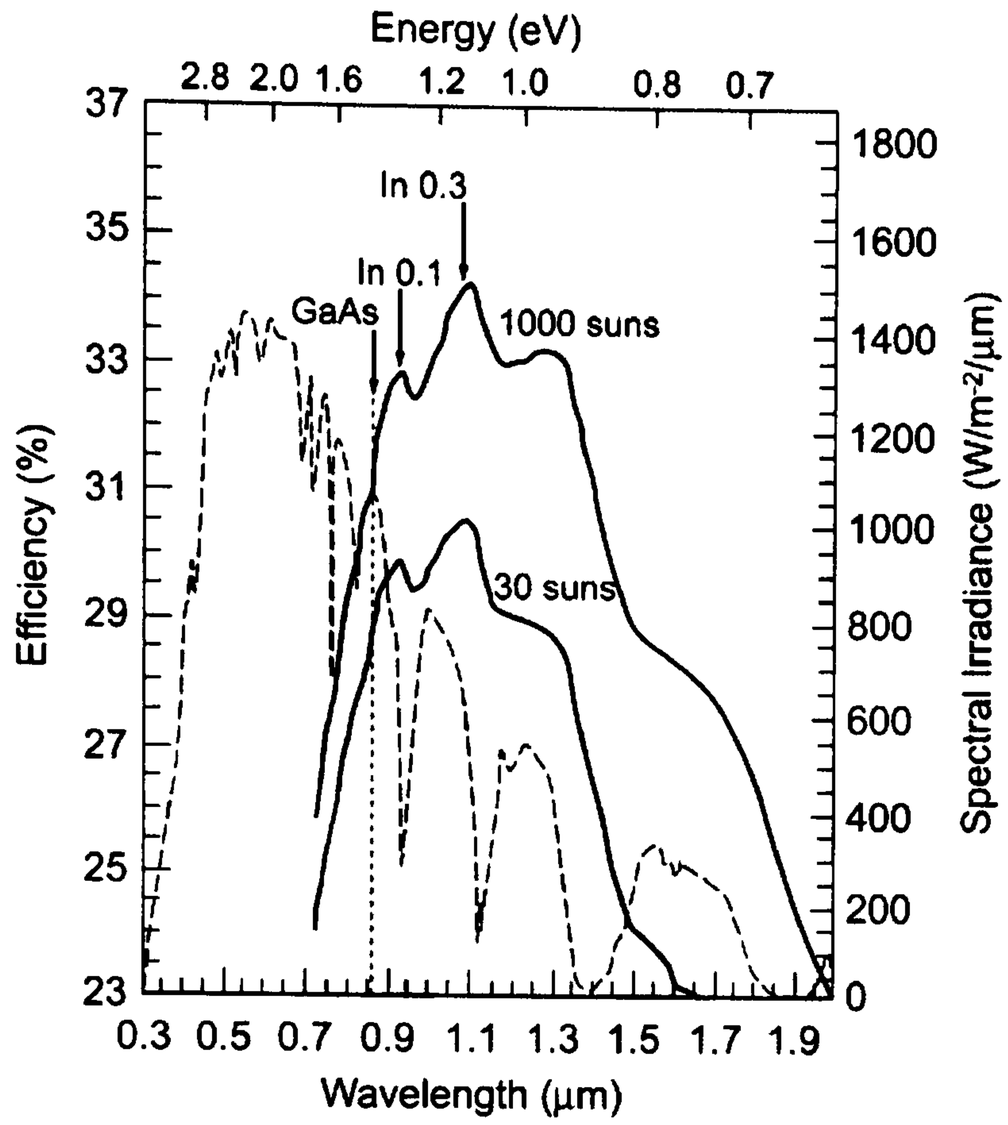

Figure 1.8: Variation of cell efficiency as a function of bandgap energy and wavelength for the AM1.5 spectrum at 30 and 1000 suns concentration [12]

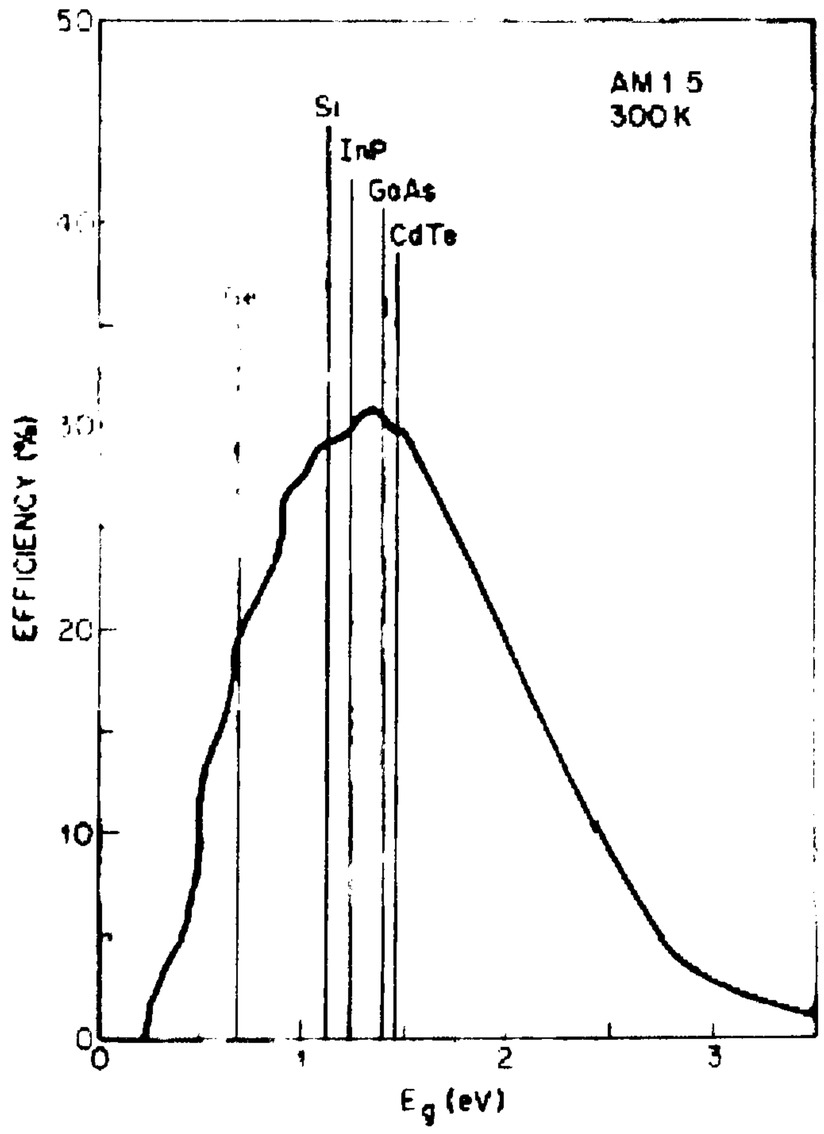

Figure 1.9: Variation of cell efficiency as a function of bandgap for the AM1.5 spectrum at 1 sun intensity [13]

1.5.6 Upper limits to photovoltaic energy conversion

The maximum theoretical efficiency of a single junction solar cell at 1 sun concentration has been calculated to be 31% [14]. There are several loss mechanisms in solar cells that cause experimental values to be much lower than this, with the record efficiency for a GaAs pn junction cell currently standing at 25.2% at 1 sun [15]. Firstly, cell efficiency is reduced by series resistance (see Sec. 1.5.2). Additionally, carriers are lost through recombination. But the most significant limiting factor for cell efficiency is the fact that if absorbed photons have energies greater than the cell band-gap the difference in energy between the photon and the band-gap will rapidly be lost via thermalisation.

1.5.7 Introduction to Multi-quantum Well Solar Cells

MQW (multi-quantum well) cells consist of layers of lower band-gap material that are inserted into the i region of a pin diode [16]. These layers are sufficiently thin that electrons in the layer region are confined to discrete energy levels. The layers of wider band-gap material between the quantum wells are termed barriers. A band diagram of an MQW cell is shown in Figure 1.10. The wells extend the energy range of photons that may be absorbed by the cell from greater than or equal to the bulk band gap E_g to greater than or equal to the band-gap of the well material plus confinement energy, E_a, thus reducing the absorption threshold of the cell.

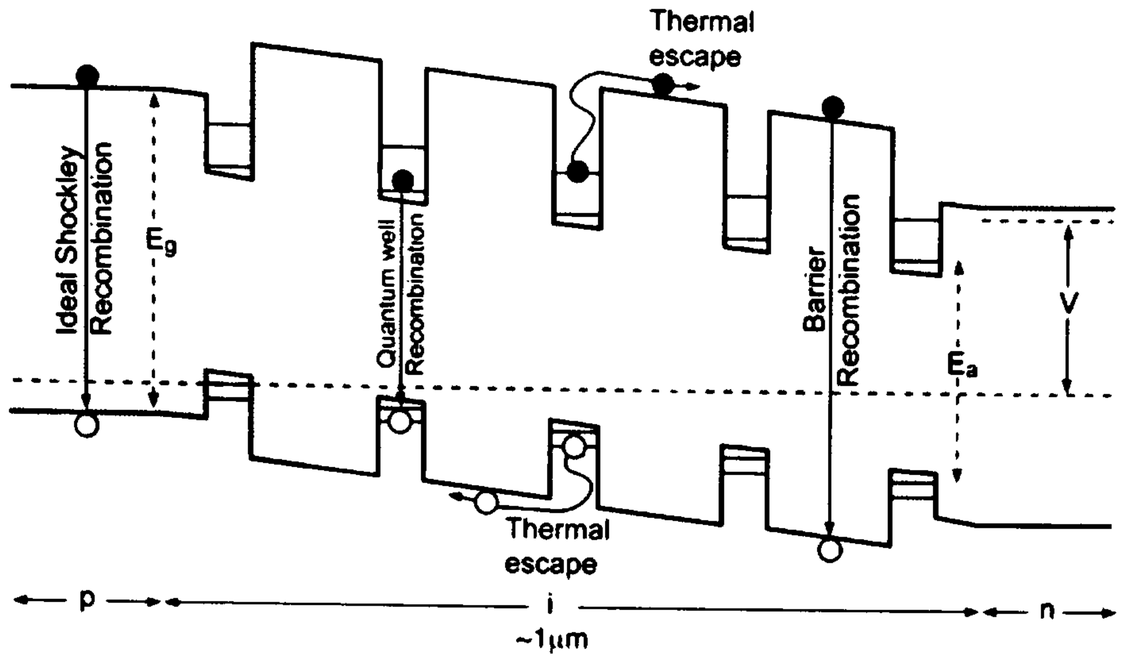

Figure 1.10. A single junction MQW cell [14].

As discussed in Sec. 1.5.5 GaAs cell efficiency can be increased if the absorption threshold can be reduced. However, there are no materials that can be grown lattice matched to GaAs and possess a lower band-gap (see Figure 1.11). Inclusion of strained quantum wells made of a material with a different lattice constant to the substrate material, such as InGaAs wells on a GaAs substrate, is possible and the introduction of a lower band-gap material will both increase the photocurrent and reduce the open circuit voltage of the cell. Provided the strained layer does not exceed a critical thickness, the lattice structure of the well layer will deform to become lattice matched with the substrate. However, if the critical thickness is exceeded the lattice of the strained layer will relax, introducing misfit dislocations which drastically reduce the open circuit voltage of the cell and hence device efficiency. It has not yet proved possible to include a sufficient number of wells in a strained InGaAs/GaAs structure to provide a large enough increase in photocurrent to compensate for the loss in open circuit voltage before relaxation occurs in the wells [17].

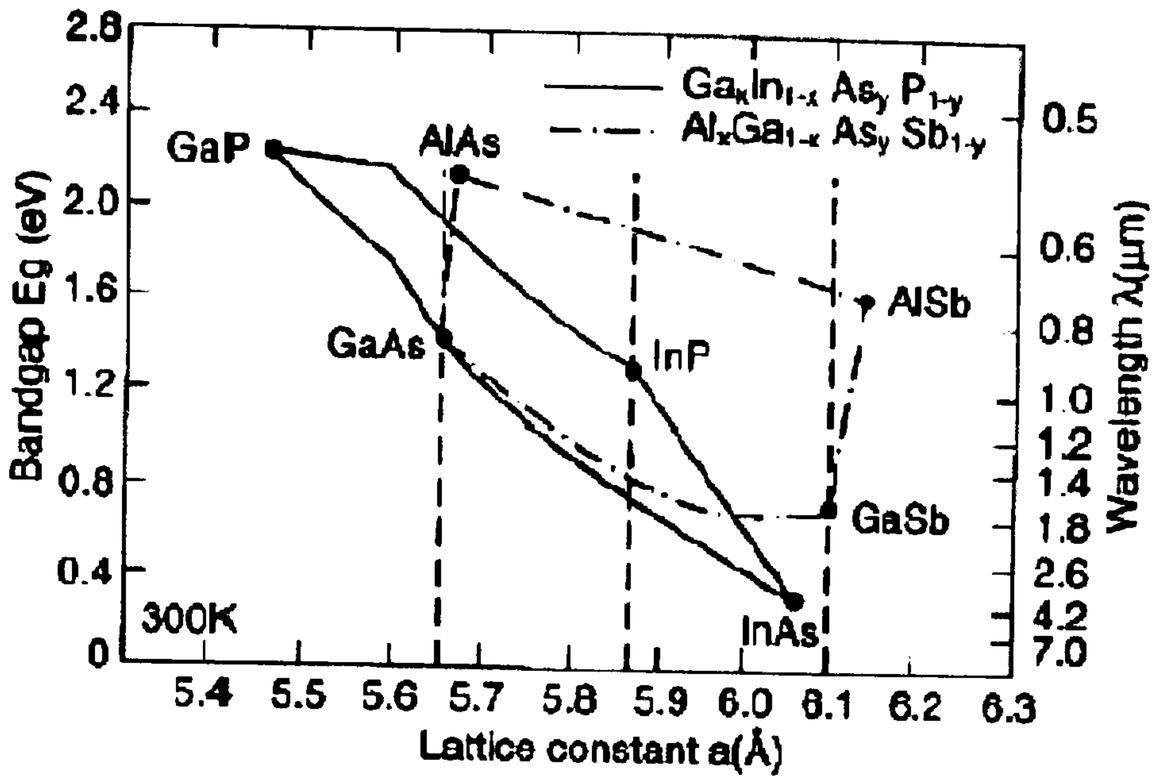

Figure 1.11. Lattice constants and bandgaps of common III-V semiconductors [13].

1.5.8 Strain balanced Multi-quantum Well Solar Cells

Strain balancing provides a method of overcoming this limit to the number of strained wells. The compressive strain in the InGaAs well layers is offset by the tensile strain in the GaAsP barrier layers, allowing the average lattice constant across the intrinsic region to match that of GaAs. Strain balancing has also been achieved in the InGaAs /InP material system [18]. Thus, the addition of enough quantum wells to sufficiently increase the device photocurrent to make the gain in J_{sc} greater the loss in V_{oc} (and hence increase overall device efficiency) becomes possible. The inclusion of strain balanced quantum wells has been demonstrated to increase device efficiency by 1.2% absolute compared to a GaAs control cell [19].

Obtaining an expression for the strain balanced condition is non-trivial. The simplest hypothesis suggests that strain balancing may be achieved when the thickness weighted

average lattice parameter of the strained layers is equal to the lattice parameter of the substrate layer [20]

$$a_0 = \frac{t_1 a_1 + t_2 a_2}{t_1 + t_2} \tag{1.12}$$

where t_1, a_1 and t_2 and a_2 are the thicknesses and relaxed lattice parameters of the compressive and tensile strained layers respectively and a_0 is the lattice parameter of the substrate layer.

Another calculation suggests that the strain balancing takes place when the strain of the two layers, weighted according to thickness and elastic constants, is matched [20].

$$a_0 = \frac{(t_1 A_1 + t_2 A_2) a_1 a_2}{a_1 A_1 t_1 + a_2 A_2 t_2} \tag{1.13}$$

where A_1 and A_2 are defined as

$$A = c_{11} + c_{12} - \frac{2c_{12}^2}{c_{11}} \tag{1.14}$$

where c_{11} and c_{12} are the elastic stiffness constants of the appropriate layer. However, the most rigorous approach to strain balancing arises from considering the tensile and compressively strain layers at their lowest energy. In this state the net stress within the double layer is zero. Therefore, the true strain balanced condition corresponds to zero in-plane stress across the strained layers. This leads to the expression given in Equation 1.15,

which is used to calculate the well and barrier layer widths and compositions for the strain - balanced samples detailed in this thesis [20].

$$a_0 = \frac{A_1 t_1 a_1 a_2^2 + A_2 t_2 a_2 a_1^2}{A_1 t_1 a_2^2 + A_2 t_2 a_1^2} \tag{1.15}$$

1.5.9 Real MQW Structures

In order to minimize the recombination of minority carriers at the cell surface a region of high band-gap semiconductor or window is often incorporated into the cell between the p region and the top surface to "reflect" minority carriers towards the depletion region. Window layers are usually made of AlGaAs as it is possible to grow AlGaAs lattice matched to GaAs (up to Al ~ 0.8). If this is the case then a further layer of low band-gap material or cap is grown over the window to prevent the AlGaAs oxidising [21].

It is also very important to maximize the amount of light that enters the cell. This is achieved by coating the cell with a layer of dielectric material that reduces the amount of light reflected from the surface of the cell; an antireflection coating. In addition, the cell requires electrical contacts so that current can be drawn from the device. The back surface of the cell can be completely covered in metal to minimize resistance to the extracted current. The front surface presents more of a problem as the contact needs to allow the maximum amount of light to reach the cell while keeping series resistance as low as possible.

The MQW cells described in this report are typically processed into two versions; a photo diode test device in which the front contact is deposited as a ring structure with a 600μm optical window in the middle, and a fully metalised device. The fully metalised device allows more accurate measurement of the dark current at high bias due to its low series resistance while the solar cell allows assessment of the quantum efficiency and light IV response of the cell. Additionally, MQW cells may also be processed as concentrator devices, in which the front contact consists of a grid of thin metal strips which minimize the contact resistance and spreading resistance in the emitter while allowing the maximum amount of light to reach the cell.

1.5.10 Overview of semiconductor band-structure

A complete band-structure of GaAs calculated using the tight-binding approximation is shown in Figure 1.12 [22]. However, when studying the optical and electrical properties of semiconductors, the remote bands are usually neglected and only the lowest energy conduction and the three highest energy valence bands are considered, as indicated by the smaller rectangle in Figure 1.12.

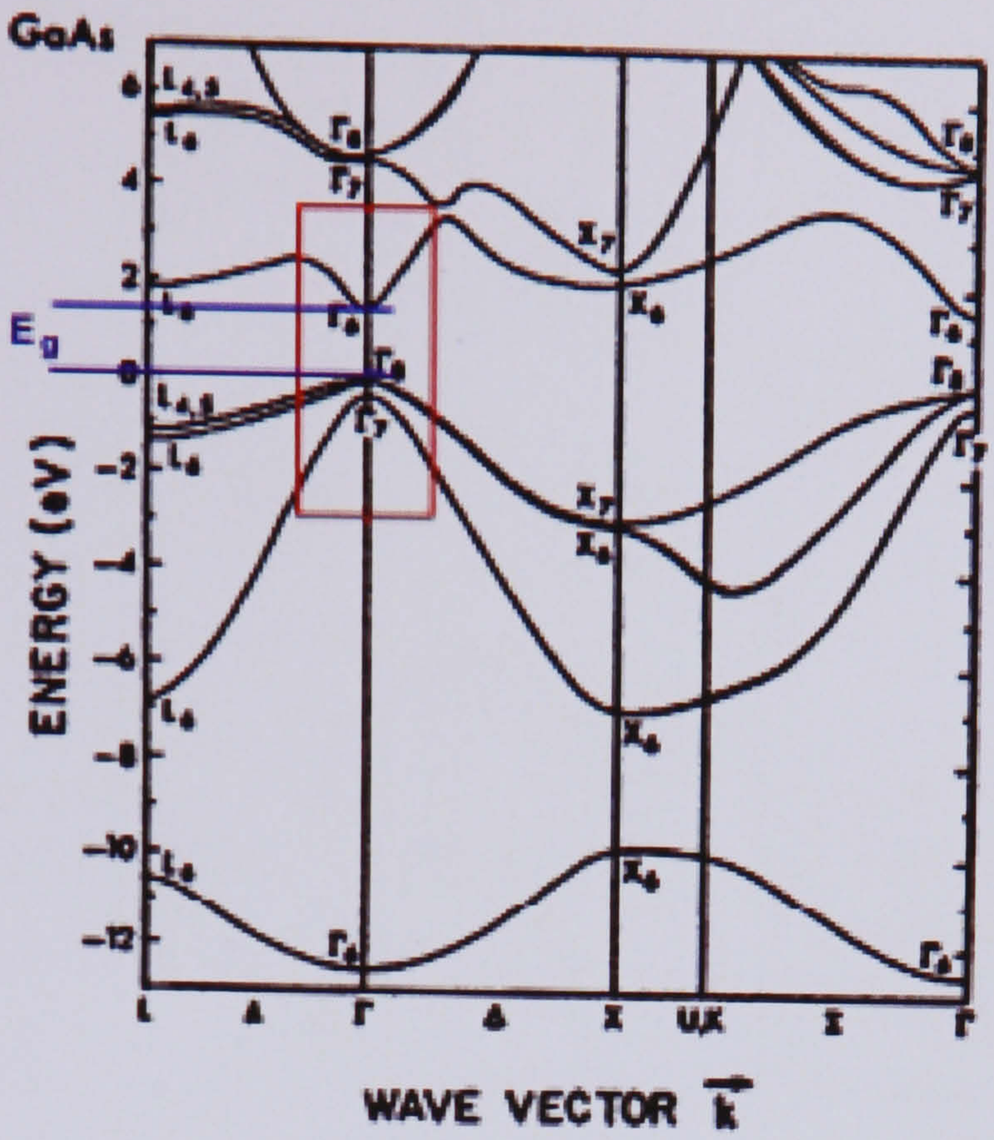

Figure 1.12: Full band-structure of GaAs calculated using the tight-binding approximation [22]

A simplified band-structure of a direct band-gap semiconductor, in which just the lowest energy conduction band and the three highest energy valence bands are considered, is shown in Figure 1.13. The two highest energy valence bands are identified as the heavy and light hole bands due to the difference in their dispersion and the corresponding difference in the effective masses of the carriers within these bands. In unstrained material the heavy and light hole bands are degenerate at the Γ point.

The third valence band is known as the spin-orbit band due to its removal from the heavy and light hole bands caused by the spin-orbit interaction [23]. The difference in energy between the heavy hole and the split-off bands is termed the split-off energy or the spin orbit splitting (Δ).

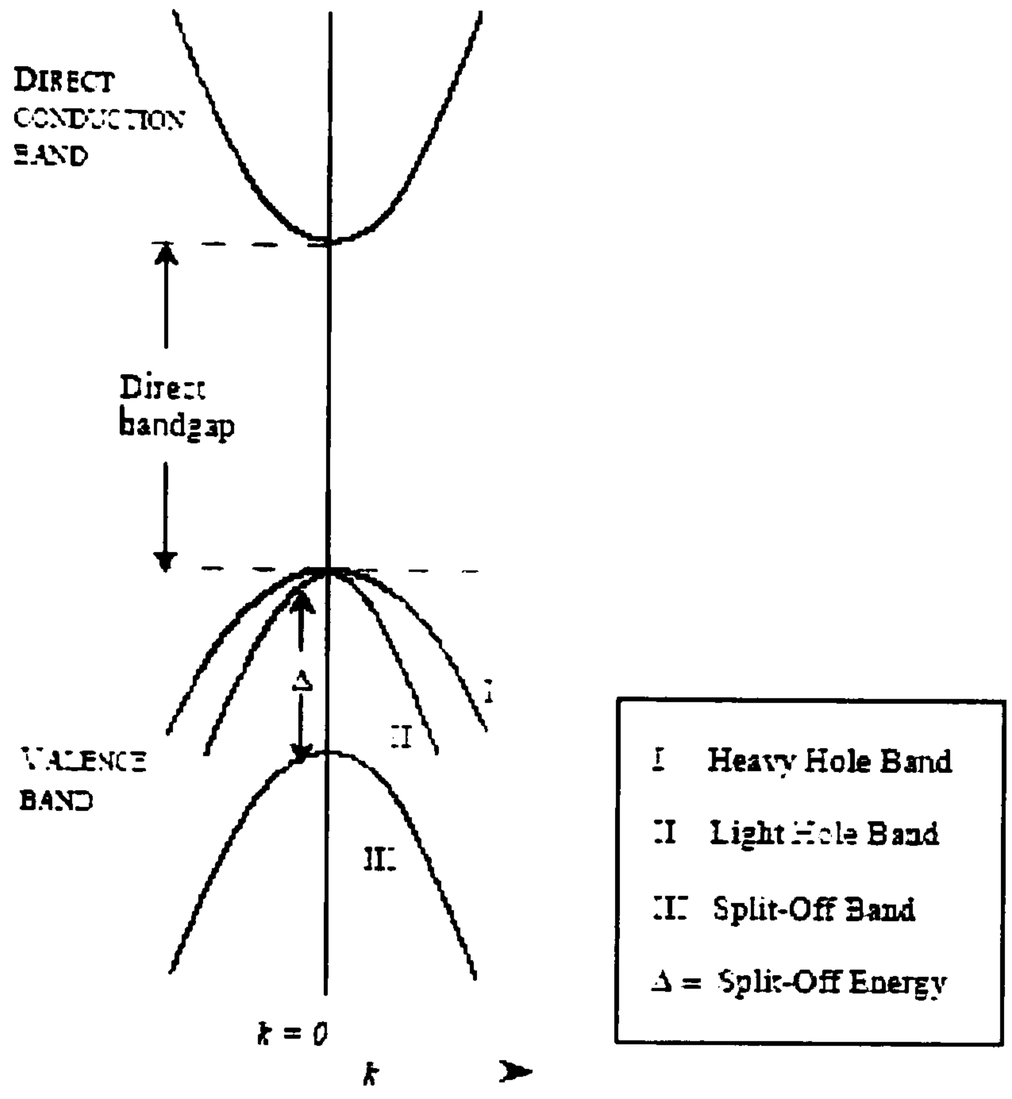

Figure 1.13: Simplified bandstructure of GaAs depicting the lowest energy conduction band and the three highest energy valance bands [24]

It should also be noted that semiconductor band-gaps decrease with increasing temperature due to the increase in atomic spacing and phonon interactions [25]. In this work the behaviour of the bandgap of GaAs has been modelled as

$$E_g(T) = 1.5192 - \frac{\left(5.405 \times 10^{-4}\right) T^2}{T + 204} \tag{1.16}$$

where T is temperature in degrees Kelvin [13].

1.5.11 Effects of quantum confinement

Quantum wells are formed by enclosing a thin layer of a semiconductor between two layers of a larger bandgap semiconductor. Quantum well structures are divided into two types according to the alignment of the band-gaps (see Figure 1.14). In type I quantum wells both

the electron and hole wells occur in the same layer of semiconductor; in type II quantum wells the electrons and hole wells are located in different layers [26].

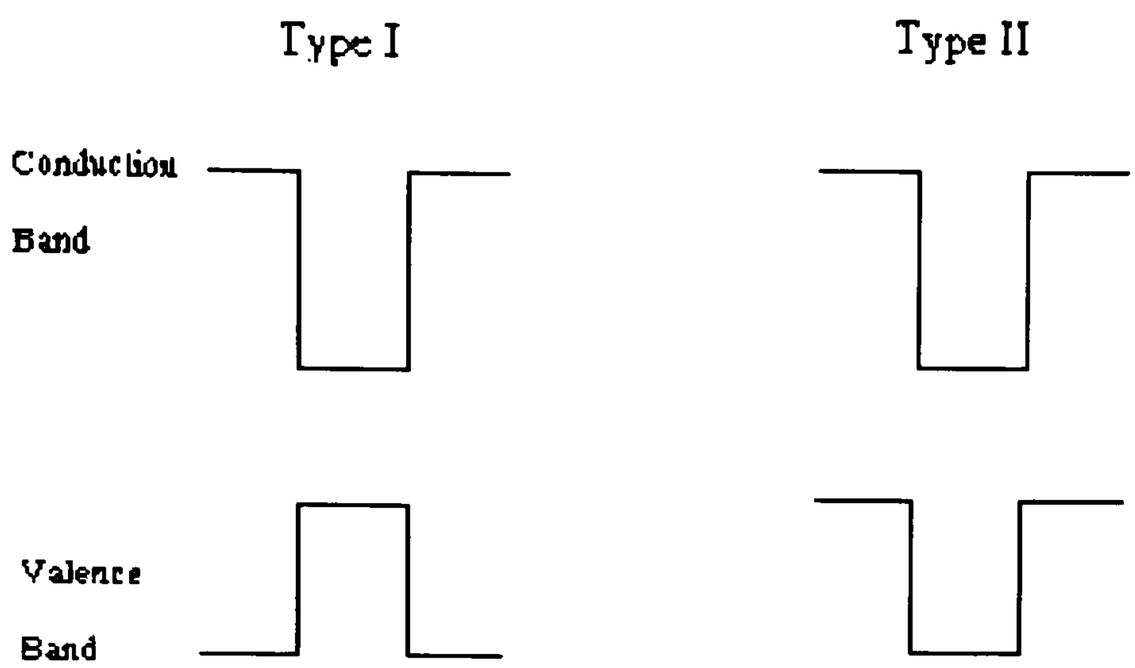

Figure 1.14. Type I and II quantum well alignments

Provided the width of the quantum well is smaller than the de Broglie wavelength of the electrons or holes the carriers are confined in the growth direction. However, the carriers are still unconfined in the x-y plane. This leads to the formation of sub-bands in the in-plane direction [27].

The energy levels in an infinite quantum well may be readily calculated using the following relationship.

$$E_n = \frac{n^2 \hbar^2 \pi^2}{2mL_w^2} \tag{1.17}$$

where L_w is the width of the quantum well and n the sub-band number. In an infinite well the wave-functions are alternating sine and cosine functions and thus for the integral of any

hole and electron wave-functions to be non-zero the index of the transitions (n) must be equal [26].

However the wave-functions for a finite quantum well do not have analytical solutions and must be solved numerically. The energy levels are given by [27]

$$\tan\left(\frac{kL_w}{2}\right) = -\frac{m_a\kappa_a}{m_b\kappa_b} \tag{1.18}$$

for odd states and

$$\cot\left(\frac{kL_w}{2}\right) = -\frac{m_a\kappa_a}{m_b\kappa_b} \tag{1.19}$$

for even states where

$$\kappa = \sqrt{\frac{2m(V-E)}{\hbar^2}} \tag{1.20}$$

and m_a and m_b are the band-edge effective masses in the well and barrier layers respectively and V is the barrier height [27].

In a finite quantum well for zero applied field the wave-functions have alternating parity and thus transitions are only allowed between levels with the same parity around the centre of the well. However, the application of an electric field breaks the symmetry of the wave-functions so that transitions between levels with opposite parities are observed.

One of the key effects of confinement is that the energy levels are removed from the band-edge. The effective band-gap of the semiconductor is therefore increased.

$$E_{g\_effective} = E_g + E_e + E_{hc} \tag{1.21}$$

where E_e and E_{hc} are the confined energies of the electron and hole respectively.

As can be seen from Equations 1.18 and 1.19, the confined levels are dependent on well width and carrier effective mass (and hence material composition). This allows the absorption of the quantum well to be controlled by varying these parameters. Additionally, the different effective masses mean that the degeneracy between the heavy and light hole bound states is lifted.

1.5.12 Absorption in quantum well solar cells

The absorption of a semiconductor depends primarily on two factors; the rate of transitions between the initial and final states and the reduced density of states for the participating bands.

For an interband transition the reduced density of states is given by [28]

$$g_{red}(E) = \frac{g_e(E)g_h(E)}{g_e(E) + g_h(E)} \tag{1.22}$$

where $g_e(E)$ is the electron density of states and $g_h(E)$ is the hole density of states, which for a two dimensional system are [28]

$$g_e(E) = \frac{m^*_{e,\|}}{\pi\hbar^2 L_w} \tag{1.23}$$

and

$$g_h(E) = \frac{m^*_{h,\|}}{\pi\hbar^2 L_w} \tag{1.24}$$

where $m^*_{e,\|}$ and $m^*_{h,\|}$ are the in-plane effective masses of electrons and holes respectively.

The reduced density of states is thus [28]

$$g_{red}(E) = \frac{m^*_{red,\|}}{\pi\hbar^2 L_w} \tag{1.25}$$

where $m^*_{red,\|}$ is the reduced in-plane effective mass which is given by

$$m_{red,\|} = \frac{m_{e,\|} m_{h,\|}}{m_{e,\|} + m_{h,\|}} \tag{1.26}$$

This gives rise to the characteristic "staircase" density of states, which, when modified to account for excitonic absorption, leads to the absorption spectra displayed in Figure 1.15.

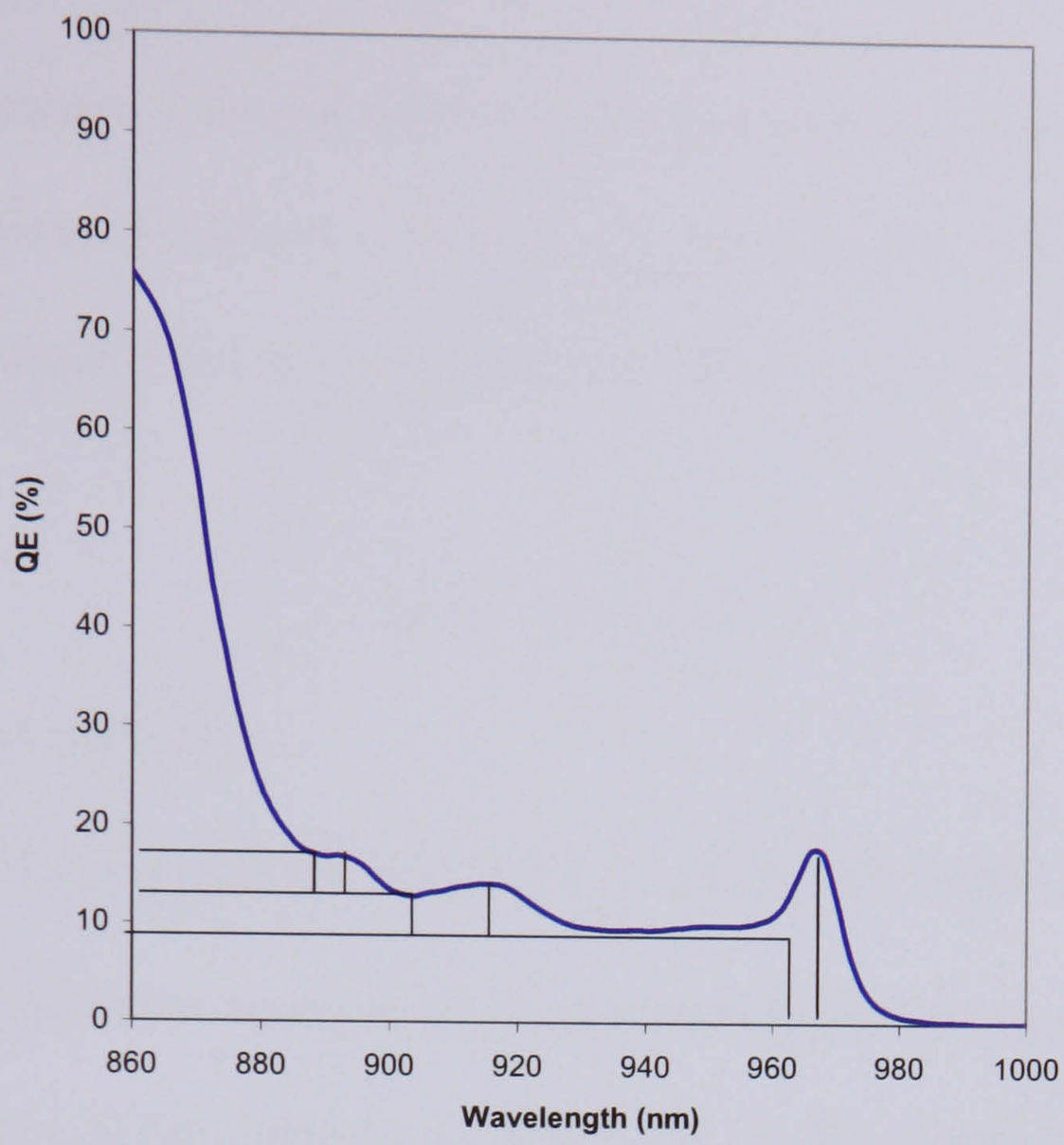

Figure 1.15: a typical density of states (black line) and absorption spectra (blue line) for a quantum well device. The spikes in the density of states and the resulting peaks in the absorption spectra are the result of excitonic absorption.

The rate of transitions between the initial and final states is governed by Fermi's Golden Rule, in which the probability of a transition between an initial state *i* and a final state *f* for a two dimensional system is expressed as [29]

$$W_{if} = \frac{2\pi}{\hbar}\left|\langle \psi_i \left| \boldsymbol{H}_1 \right| \psi_f \rangle\right|^2 \delta\left[\hbar w - E_e - E_h - E_g\right] \qquad (1.27)$$

where ψ_i and ψ_f are the wave-functions of the initial and final states respectively, $\hbar\omega$ is the energy of the incident photons and $E_e + E_h + E_g$ is the effective bandgap for absorption as in Equation 1.21. The term $\mathbf{H_1}$ represents the perturbation in the Hamiltonian caused by the interaction between the electromagnetic radiation and the atoms in the semiconductor and has the form **e.p** where **e** is the polarisation vector of the incident light and **p** is the momentum operator [29].

Due to the periodic nature of the semiconductor crystal structure, the wave-functions of the carriers can be separated into Bloch functions, *U(r)*, that represent the periodicity of the lattice, and slowly varying envelope functions *F(r)* [29].

$$\psi(r) = F(r)U(r) \tag{1.28}$$

Thus for an interband transition

$$\langle \psi_v | \boldsymbol{H}_1 | \psi_c \rangle = \langle U_c | U_v \rangle \langle F_c | \boldsymbol{e.p} | F_v \rangle + \langle F_c | F_v \rangle \langle U_c | \boldsymbol{e.p} | U_v \rangle \tag{1.29}$$

where ψ_c and ψ_v are the wave-functions of the electrons and holes, U_c and F_c are the Bloch and envelope functions of the electrons, U_v and F_v are the Bloch and envelope functions of the holes.

The symmetry of the Bloch functions must now be taken into consideration. In a direct band-gap semiconductor the conduction band has s like character and hence has even symmetry. The valence band has p like character and hence has odd parity. Therefore $\langle U_c | U_f \rangle = 0$ for interband transitions and as shown in Ref. 28

$$\langle \psi_i | \boldsymbol{H}_1 | \psi_f \rangle = \langle F_c | F_v \rangle \langle U_c | \boldsymbol{e.p} | U_v \rangle \tag{1.30}$$

The term $\langle F_c | F_v \rangle$ governs which transitions are allowed and which are forbidden. In a finite quantum well with no field applied the envelope functions of the sub-bands have alternating even and odd parity, thus a transition between a hole sub-band m and an electron subband n is only allow if

$$|m - n| = even\ integer \tag{1.31}$$

If an electric field is applied to the wells the parity of the sub-bands is altered and forbidden transitions can occur.

The term $\langle U_c | \boldsymbol{e.p} | U_v \rangle$ accounts for the effects of polarisation of the incident light. For TE polarisation

$$3\langle U_{lh} | \boldsymbol{e.p} | U_e \rangle = \langle U_{hh} | \boldsymbol{e.p} | U_e \rangle \tag{1.32}$$

where U_{lh} and U_{hh} are the Bloch functions of the light and heavy hole sub-bands respectively. For TM polarisation

$$\langle U_{hh} | \boldsymbol{e.p} | U_e \rangle = 0 \tag{1.33}$$

Thus for TE polarisation heavy hole transitions absorb three times as strongly as transitions involving the light hole and in TM polarisation heavy hole transitions are not observed [28].

References

[1] Intergovernmental Panel on Climate Change. IPPC Third Assessment Report: Climate Change, 2001.

[2] United Nations Framework Convention on Climate Change. Proceedings of the United Nations Climate Change Conference, 2005.

[3] Taken from http://www.bp.com/genericarticle.do?categoryId=98contentId=7018758. Remarks made by BP CEO Lord Browne at the launch of the BP statistical review.2006.

[4] http://news.bbc.co.uk/1/shared/spl/hi/guides/456900/456932/html/nn1page1.stm. Guide to nuclear power, 2006.

[5] Taken from http://www.iea pvps.org/isr/22.htm. Total photovoltaic power installed in IEA PVPS countries, 2006.

[6] Martin A. Green. Third Generation Photovoltaics: Ultrahigh Conversion Efficiency at Low Cost. Progress in Photovoltaics: Research and Applications, 9:p123–135, 2001.

[7] American Society for Testing and Materials, Standard number E490-73a.

[8] Dave Bushnell. "Optimization of strain compensated multi-quantum well solar cells." PhD thesis Imperial College London, 2003.

[9] Renewable resource data centre. http://rredc.nrel.gov/solar/glossary/ 2001.

[10] J. Nelson. Physics of solar cells. Imperial College Press, 2003.

[11] W. Shockley and W. Read. Statistics of Recombination of Electrons and Holes. Phys. Rev, 82:pp 835–842, 1952.

[12] J. Ward et al. Proc. 23rd IEEE Photovoltaic Specialists Conference. p650, 1993 [18] C. Henry. Limiting efficiencies of ideal single and multiple energy gap terrestrial solar cells. J. App. Phys, 51:999, 1980.

[13] S. Sze. "Semiconductor devices; physics and technology." Wiley Interscience. 1981

[14] C. Henry. "Limiting efficiencies of ideal single and multiple energy gap terrestrial solar cells." J. App. Phys, 51:999, 1980.

[15] M. Green. Solar cell efficiency tables (version (15)). Progress in Photovoltaics, 11:999, 2003.

[16] K. Barnham et al. "Quantum Well Solar Cells." Applied Surface Science, **113** (722). 1997.

[17] M. Mazzer et al. "Study of misfit dislocations by EBIC, CL and HRTM in GaAs/InGaAs lattice strained multi-quantum well p-i-n solar cells" Material Science and Engineering., **B42**, p43. 1996

[18] J. Connolly and C. Rohr. "Quantum well cells for thermophotovoltaics". Semiconductor Sci. and Tech. **18** S216-S220. 2003

[19] D. Bushnell et al. "Effect of well number on the performance of quantum well solar cells." J. App. Phys, 97:p. 124908, 2005

[20] N. Ekins-Daukes et al. "Strain-balanced criteria for multiple quantum well solar structures and its signature in X-ray rocking curves." Journal of Crystal Growth and Design. 2 (4). pp 287-292. 2002.

[21] John Roberts. Private Communication. 2006.

[22] S. Adachi. "GaAs and related materials" World Scientific Publishing. 1994

[23] J. Nelson. "Low-dimensional semiconductor structures." ed. K. Barnham and D. Vvedensky. Chapter 6. Cambridge University Press, 2001.

[24] J. Singh. "Semiconductor Devices: Basic Principles." John-Wiley, 2001.

[25] N. Ashcroft and N. Mermin. "Solid state physics." Thomson Learning. 1976.

[26] E. Johnson. "Low-dimensional semiconductor structures." ed. K. Barnham and D. Vvedensky. Chapter 2. Cambridge University Press, 2001.

[27] A. French and E. Taylor. "An Introduction to Quantum Physics." W. W. Norton and Company. 1978

[28] P. N. Stavrinou. "Opto-Electronic Components and Devices". Msc Lecture Course, 2006.

[29] F. Laugton. "Low dimensional semiconductors" MPhys Lectures. University of Bath. 2002.

2 Solar Cell Growth, Processing and Characterisation

2.1 Solar Cell Growth

The solar cells studied for this report have been grown by Metal-Organic Vapour Phase Epitaxy (MOVPE). This technique allows the production of high purity semiconductors and is particularly suitable for MQW device fabrication as it is possible to accurately control the depth and doping levels in each layer of the device.

In the growth of a typical GaAs solar cell gaseous tri-methyl gallium, $Ga(CH_3)_3$ and arsine, AH_3, are used as sources or precursors for Ga and As respectively. These are then fed into a reaction chamber containing a GaAs substrate. The chamber is heated to ~ 600°C, causing to the precursors to dissociate. The Ga and As are deposited onto the substrate surface, leaving methyl and hydrogen radicals in the gas phase where they react to form methane. This is then purged from the chamber along with any unreacted precursors. The main source of contamination in the resulting GaAs wafer is unreacted methyl radicals which further dissociate to form carbon, which can become incorporated into the wafer in place of an arsenic atom [1].

2.2 Solar Cell processing

Solar cell processing describes the additional steps required to convert a semiconductor wafer into a usable photovoltaic device. Unless otherwise stated the samples described in this work have been processed at the Centre for III-V Technologies in Sheffield. The processing method at this facility is outlined below

- The back contact is formed by evaporating a layer of an alloy of 50% In – 50% Ge followed by a layer of Au onto the back of the substrate. This is then annealed by increasing the temperature to 420 °C.
- The front surface contact is created by covering the front surface with photoresist and using a mask to define the areas of the surface that metal will subsequently be evaporated onto. A layer of Ti followed by a layer of Au is evaporated onto the wafer.
- The cap layer of the solar cell is removed using a 1:19 solution of ammonia: peroxide.
- A SiN_3 antireflection coating is deposited onto the wafer. A typical coat has a layer thickness of 45nm, a refractive index of 1.97 and is optimised at 600nm. The area over the optical window of the photocell is covered with a layer of photoresist and excess antireflection coat is removed using a CHF_3/O_2 reactive ion etch.
- Individual devices on the wafer are isolated so they share the same back contact but have separate front contacts. This is achieved using an etch of 1.1.1 solution (by volume) of hydrogen bromide: acetic acid: potassium dichromate.

- The wafer is cleaved into sets of six photocells which are then bonded to TO5 headers. Gold wires are used to connect the front contact of each device to the pins of each header.

The processing method is outlined in Figure 2.1

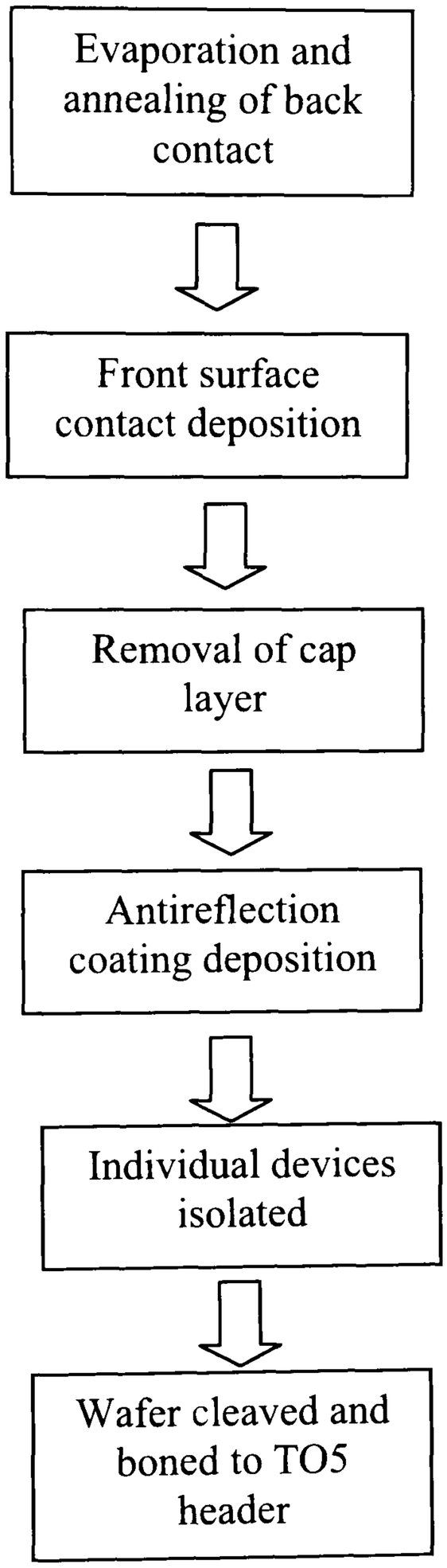

Figure 2.1: Outline of processing method

2.3 Solar Cell Characterisation

2.3.1 Dark Current Measurement

Solar cell characterisation generally begins with an analysis of the dark currents of a number of devices over a range of voltages to establish both the spread in the magnitude of the dark current (an important indication of processing quality) and the series and shunt resistances of the cell. The bias of the cell is controlled using a Keithley source measurement unit (model 238) and the resulting dark current recorded and transferred to a PC using an IEEE-488 interface bus. The cell is kept at a constant temperature of (25±0.1)°C using a Peltier plate controlled by a platinum resistance thermometer monitored using a Keithley 195A digital multimeter.

It is also possible to fit the recorded dark current data to Equation 1.5, Chapter 1, using an iterative Newton-Raphson based program designed by Dr D. Bushnell [2].

2.3.2 External Quantum Efficiency Measurements.

Devices that show appropriately low dark currents and series resistance can then be further examined by characterization of the external quantum efficiency (EQE). The equipment used in such a characterization is shown in Figure 2.2.

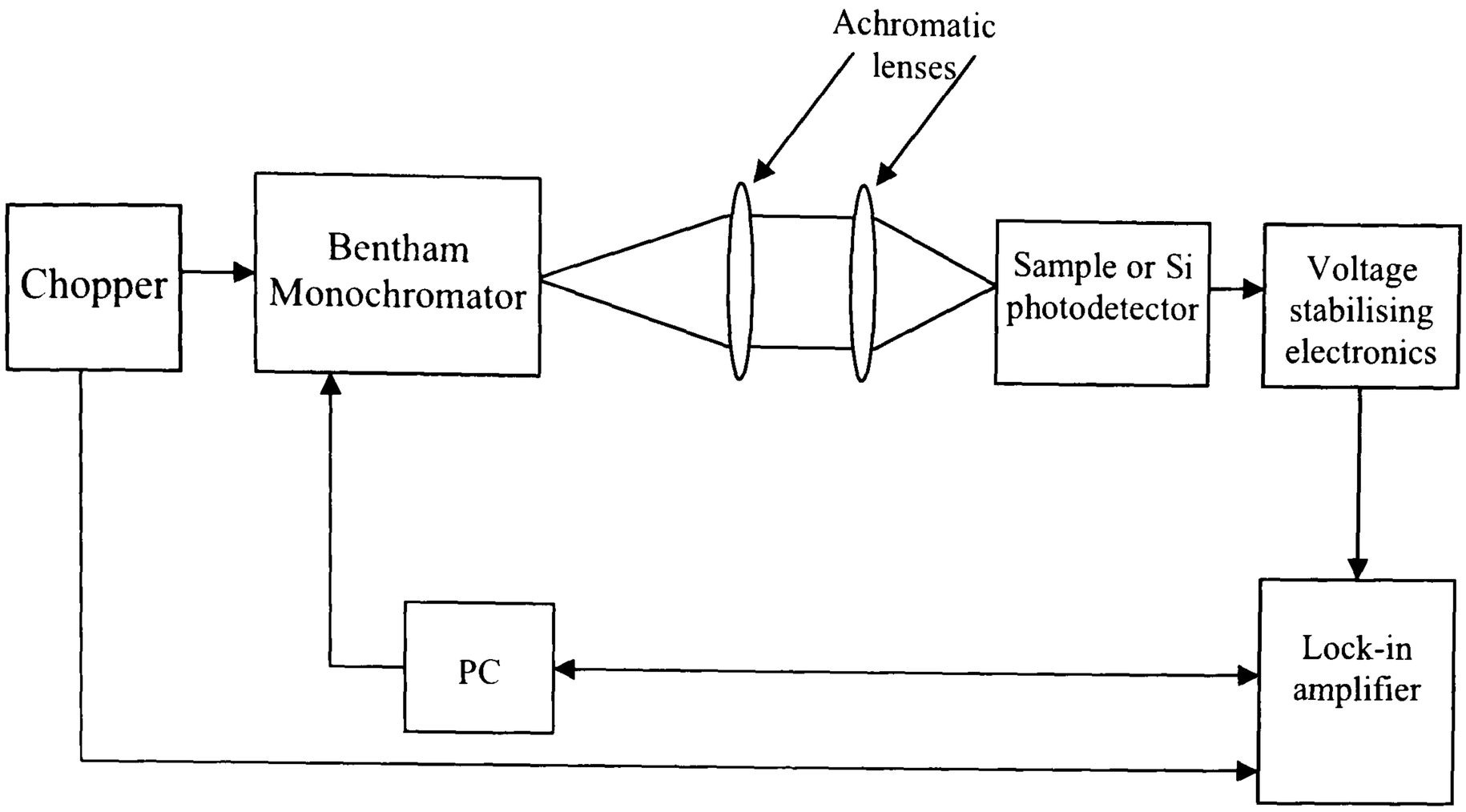

Figure 2.2: Outline of the experimental set up for external quantum efficiency measurements

Light from a tungsten filament lamp is chopped and coupled into a Bentham M300 30cm monochromator. The light emitted from the monochromator passes through a 2mm pinhole and into a pair of achromatic lenses before being focused onto the optical window of the device under investigation. The photocurrent from the device is then fed through custom built electronics (designed and built by Dr D Bushnell [2]) that fixes the voltage across the device independent of the D.C. diode current. The photocurrent is then measured using a Stanford SR510 lock-in amplifier which combines the chopped photocurrent with the chopper signal. The use of the lock-in amplifier allows background light at a different frequency to the chopped output of the lamp to be discarded, hence increasing the signal to noise ratio. The recorded photocurrent is then transferred to a PC using an IEEE-488 interface bus.

In a typical experiment the device photocurrent is measured at zero bias, between wavelengths of 400nm and 1000nm with a wavelength step of 2nm at a chopper frequency of 315 Hz. The experiment is then repeated using a silicon photodiode of known EQE. The ratio of the photocurrents of the device to that of the silicon photodiode is then multiplied by the EQE of the silicon diode to find the external quantum efficiency of the device.

2.3.3 Reflectivity Measurements.

Although the external quantum efficiency of a solar cell is a useful characterization procedure it is dependent on the quality of the AR coat on the device. It is often desirable to remove this dependence and examine the ratio of electron-hole pairs collected to photons entering the solar cell, a quantity known as the internal quantum efficiency (IQE) as this is more directly related to the device physics. To calculate the IQE the amount of light reflected from the solar cell must be measured. This is done using a similar method to the EQE measurement; the light from a tungsten lamp is chopped, fed through a monochromator and focused onto the optical window of the sample under investigation. However, unlike the EQE measurement, the light reflected from the sample is then further reflected through 90° by a beam splitter and focused onto a silicon photodiode. The photocurrent generated by the silicon diode as a function of incident wavelength is then measured using a lock-in amplifier and recorded on a PC. The experiment is then repeated using a calibrated mirror in place of the solar cell and, as in the EQE experiment described above, the results of the two experiments are ratioed to produce the reflectivity of the solar cell. Once both the reflectivity and EQE of a solar cell are known the IQE of the device can be calculated using

$$IQE(\lambda) = \frac{EQE(\lambda)}{1 - \frac{R(\lambda)}{100}} \qquad (2.1)$$

where R(λ) is the reflectivity.

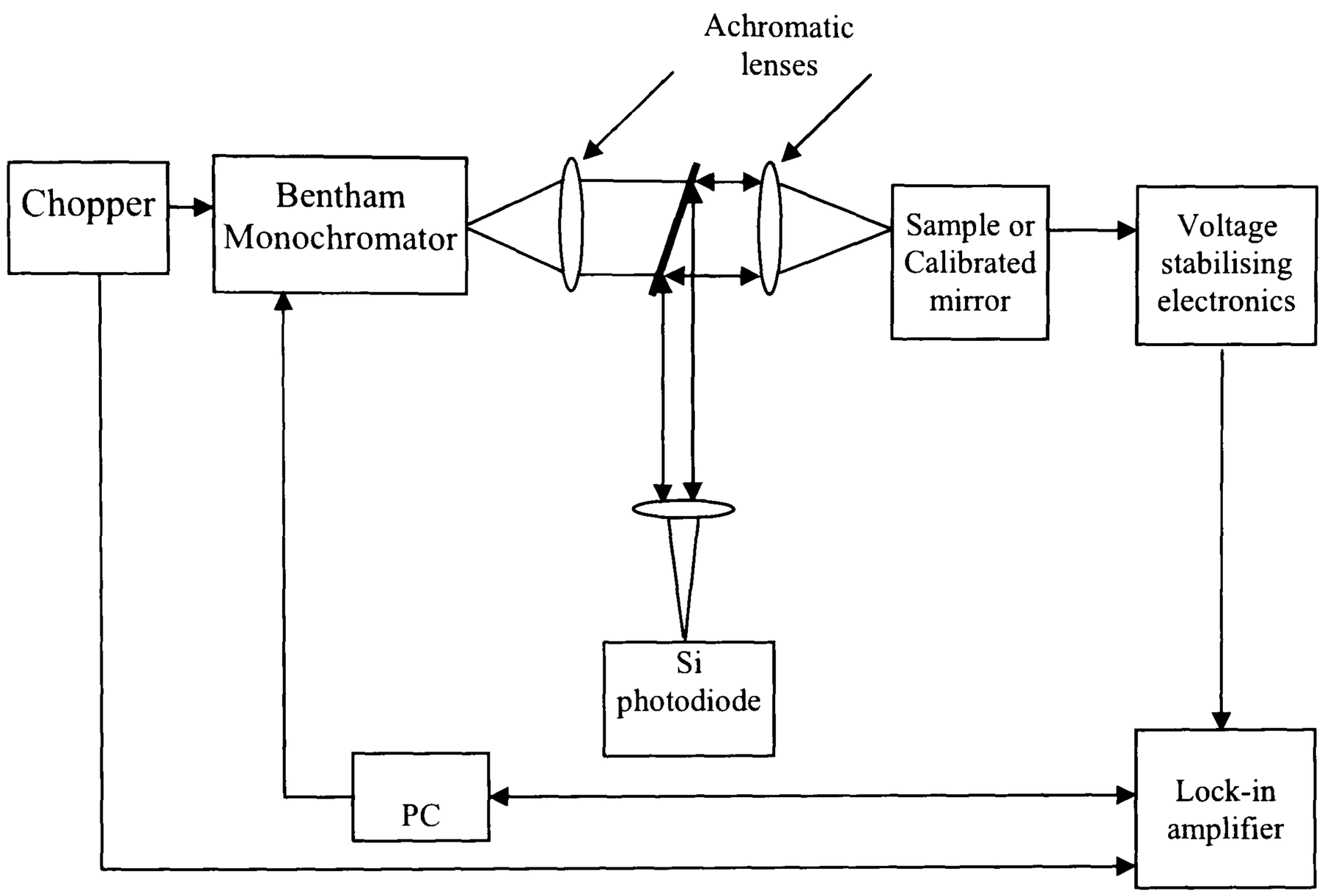

Figure 2.3: Outline of the experimental set up for reflectivity measurements

The IQE of a device may be combined with a calculated reflectivity from an idealised dual layer ZnS/MgF_2 AR coat to obtain an ideal EQE and hence an upper limit on the photocurrent that can be generated by a particular device.

2.3.4 Monochromatic IV measurements

The level of background doping present in the intrinsic region of a p-i-n junction has a direct effect on the how well the field is maintained across the intrinsic region as forward bias is applied to the sample, and hence on device performance. Provided the level of background doping remains sufficiently low (10^{14} cm^{-3}) the electric field will still extend across the intrinsic region even at high forward bias. At higher levels of background doping (10^{17} cm^{-3}) the field across the i region will fail and carrier collection will become impeded.

It is possible to ascertain the level of background doping using a monochromatic IV scan in which the photocurrent of a solar cell is measured using a similar method to the one outlined in Sec. 2.3.2. In a monochromatic IV experiment the wavelength of the illuminating light is kept constant and the photocurrent of the device being studied is measured as a function of bias. A device with low background doping will produce a constant photocurrent in both reverse and forward bias until the dark current produced by the sample becomes too large for the voltage stabilising electronics to cope with. The photocurrent produced by a sample with high background doping will be high in reverse bias and drop as forward bias is applied and the field across the i region reduces and finally disappears as illustrated in Fig.2.4.

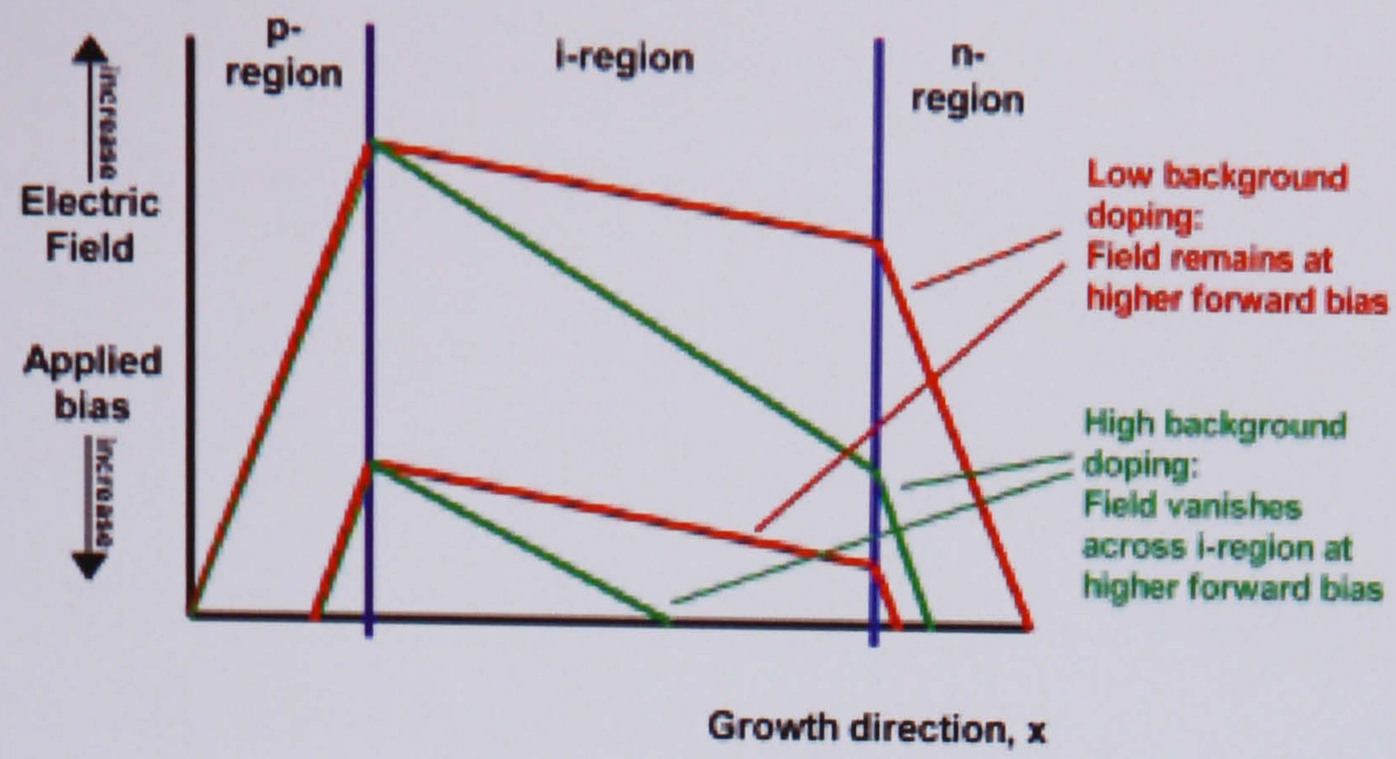

Figure 2.4: The electric field across the intrinsic region in a sample with low background doping (red line) and high background doping (green line) at short-circuit current(upper set) and forward bias (lower set) [3].

2.3.5 Light IV measurements and Additivity

Once the EQE of a device is known the short circuit current of the solar cell in a given spectrum and concentration may be calculated by evaluating Equation 1.6. The device is then illuminated using an Oriel fiber-optic illuminator and the light intensity is adjusted to produce the required short circuit current. The photocurrent generated by the solar cell is then measured as a function of bias using the method detailed in Section 2.3.1

An important test of the quality of an MQW solar cell is a condition known as additivity, in which the photocurrent produced by a solar cell is equal to the short circuit current minus the measured dark current i.e. additivity tests the extent to which equation 2.2 holds in practice.

$$J_{tot}(V) = J_{01}(e^{\frac{qV}{\eta_1 kT}} - 1) + J_{02}(e^{\frac{qV}{\eta_2 kT}} - 1) - J_{sc} \qquad (2.2)$$

This can be tested by calculating an ideal light IV curve using the short circuit current and dark current of a device and then comparing it to the measured light IV curve. This is a particularly useful test in large i region cells because if the electric field is not maintained across the i region, additivity will not hold. The open circuit voltage, maximum power voltage and current and the fill-factor of the cell are then obtained from the resulting light IV curve and can be used to project the efficiency the cell would obtain if it were illuminated by that particular spectrum.

References

[1] A. Jones. "Metalorganic precursors for vapour phase epitaxy". J. Crystal Growth **129**.1993. pp728-773

[2] D. Bushnell. "Optimisation of strain-compensated multi-quantum well solar cells." PhD thesis. Imperial College. 2003.

[3] B. Kluftinger. "An experimental study of quasi-Fermi level separations in quantum well solar cells." PhD thesis. Imperial College London. 2000

3. Device optimisation

3.1 Large well number devices

3.1.1. Introduction

As described in Chapter 1 the enhancement in spectral response caused by the addition of quantum wells to the intrinsic region of a p-i-n solar cell allows quantum well solar cells to make better use of the incident solar radiation and thus produce higher photocurrents than conventional GaAs solar cells. However the inclusion of quantum wells also leads to an increase in dark current and a reduction in open circuit voltage, although it is possible to minimise this effect using strain balanced [1,2] materials. Previous studies [3] suggested that for devices containing up to 50 strain-balanced wells the cell dark current increases less strongly with increasing well number than the photocurrent, causing overall cell efficiency to increase with rising well number. In order to produce SB-QWSCs of maximum possible efficiency it is necessary to investigate whether these trends continue as well number is increased beyond fifty, or if there is an optimum well number beyond which efficiency decreases. Also, the question of how many strain balanced well-barrier periods it is possible to grow in practice needs to be addressed. Additionally, even if the photocurrent continues to increase faster with well number than the dark current, efficiency may not continue to increase if there is a loss of field across the wells at the operating voltage as this will cause reduced carrier collection and therefore lower device efficiency.

3.1.2. Sample description

In order to examine the effects of continued increase in well number two strain balanced samples, differing only in well number, were grown as outlined in Chapter 2. The composition of these wafers is detailed in Table 3.1.1. In particular, it is important to note that the first two wafers possess the same e1-hh1 exciton wavelength (932 nm), making them directly comparable. Additionally, a second 65 well wafer with shallower quantum wells and an e1-hh1 exciton wavelength of 924 nm was also grown (see section 3.1.4).

Wafer Name	No of wells	Well width (nm)	Barrier width (nm)	Well In fraction	Barrier P fraction	e1-hh1 exciton wavelength (nm)
Qt1840	50	8.3	17.4	0.12	0.090	932
Qt1838R	65	8.3	17.4	0.12	0.090	932
Qt1858D	65	8.3	17.4	0.11	0.089	924

Table 3.1.1. Composition of devices studied

Each sample was processed as both a 1mm diameter test photocell with a SiN_3 anti reflection (AR) coating and a fully metalised device, using the method given in Chapter 2.

3.1.3. Cell characterisation

The dark currents of the fully metalised samples were measured and fitted as in Equation 4 1.

$$J_d = J_{01}(e^{\frac{-qV}{n_1 kT}} - 1) + J_{02}(e^{\frac{-qV}{n_2 kT}} - 1) \qquad (4.1)$$

where J_d is the total dark current density and J_{01} and J_{02} the reverse saturation currents of the $n_1 = 1$ and $n_2 \sim 2$ current densities [4]. The mean value of J_{01} was calculated for each wafer from fits to approximately 18 fully metalised devices with n_1 fixed at unity and n_2 allowed to vary as a free parameter.

The internal quantum efficiencies of the solar cells were determined using external quantum efficiency and reflectivity measurements as detailed in Chapter 2. This data was then used to predict external quantum efficiencies for a sample with an ideal SiN_3 AR coating by combining the internal quantum efficiencies with calculated reflectivities of an idealised SiN_3 coat, thus removing any effect on the samples of differences in the anti reflection coating. The error on the quantum efficiencies and reflectivities is estimated to be around 5%.

The light current densities of each photocell were measured in a 3000K black body spectrum with the light intensity adjusted so the device short-circuit current (J_{sc}) was equal to the predicted short circuit current under illumination from the AM1.5g spectrum using the ideal external quantum efficiency discussed above. A front surface metallization of 5% is assumed. Efficiencies and other parameters predicted in this way for quantum well solar cells have subsequently been shown to agree well with measurements obtained when the same wafer has been processed as a solar cell and measured in the appropriate simulator [1]. However, in this work the aims of these

measurements are to test if additivity holds at the relevant current level and to be able to make comparisons between cells measured under the same conditions. The fill factors, open circuit voltages and predicted AM1.5g cell efficiencies obtained from these measurements were compared to predicted values obtained from the subtraction of J_d from J_{sc}. As discussed in Chapter 2, the comparison of the measured light IV with the prediction obtained from the subtraction of the measured J_d and the J_{sc} fixed as above is a test of *additivity*. This is an important test for quantum well cells which will fail if the electric field is not maintained across the i-region [5].

3.1.4. Experimental results and discussion

3.1.4.1 Dark currents

Typical dark currents of Qt1838R and Qt1840 are shown in Figure 3.1.1. At low bias the dark current of the 65 well sample is around an order of magnitude higher than that of the 50 well sample although at higher bias the dark currents of the two cells start to converge.

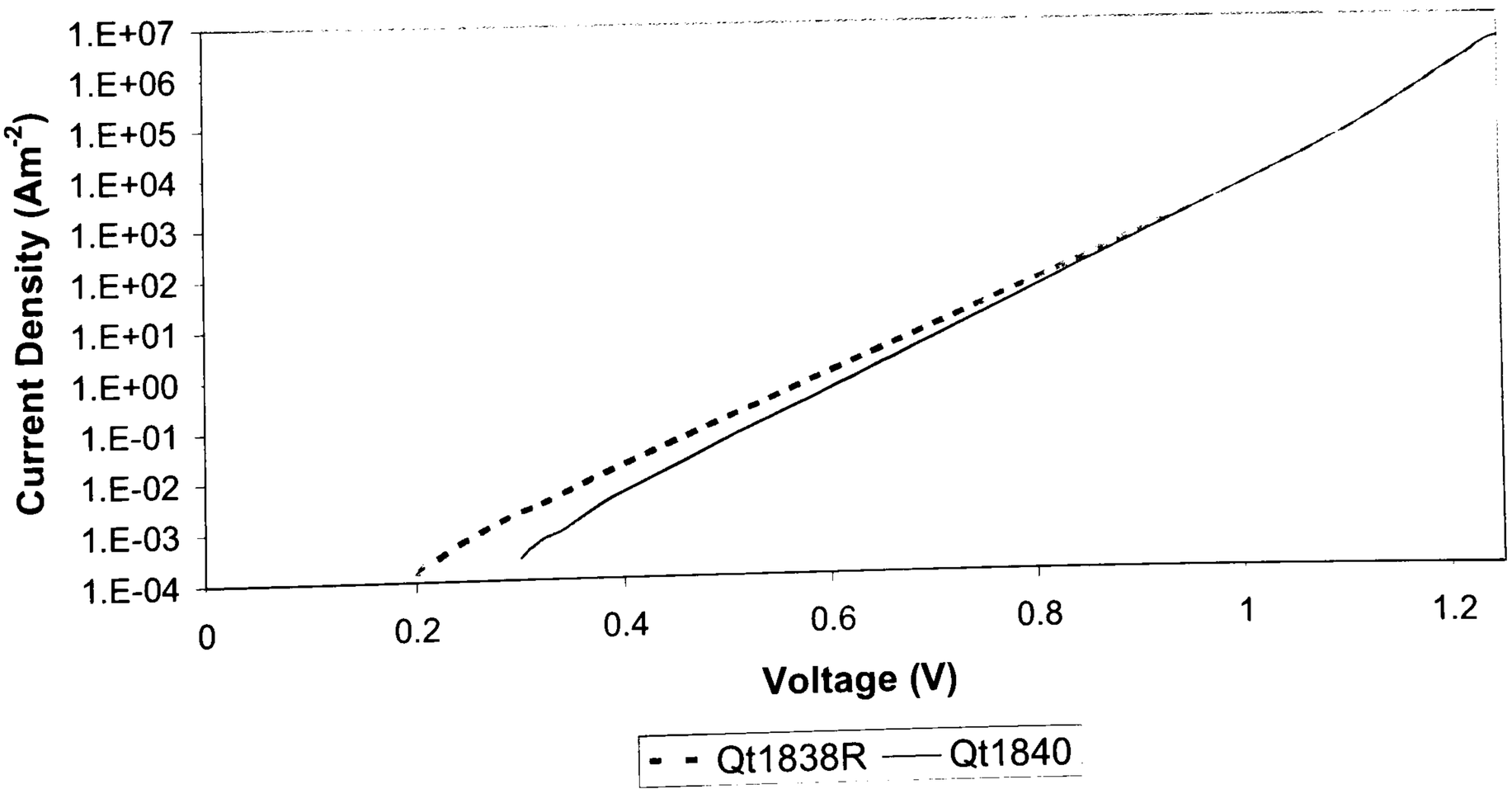

Fig. 3.1.1. Dark current densities of Qt1838R and Qt1840

The n = 1 reverse saturation current (shown in Table 3.1.2) of Qt1840 is significantly lower than that of Qt1838R, demonstrating an increase in recombination with increasing well number. This is to be expected if recombination is dominated by radiative recombination in the quantum wells as discussed in Chapter 4; i.e. as absorption increases so will the radiative recombination [6].

Sample name	No of wells	Ideality n = 1 reverse saturation current (A)
Qt1840	50	$(2.8 \pm 0.3) \times 10^{-15}$
Qt1838R	65	$(3.8 \pm 0.2) \times 10^{-15}$

Table 3.1.2. Ideality n=1 reverse saturation currents of Qt1838R and Qt1840

3.1.4.2 Photocurrents

The predicted photocurrents of Qt1838R and Qt1840 and the same within the limits of experimental error. This suggests that the increased absorption due to the larger number of wells in Qt1838R is compensated for by a slightly lower absorption in the p-region (see Fig. 3.1.2).

Sample Name	No. of wells	Predicted AM1.5g photocurrent (assuming 5% shading) (Am^{-2})
Qt1840	50	280±14
Qt1838R	65	281±14

Table 3.1.3. Predicted photocurrents of Qt1838R and Qt1840 under illumination by the AM1.5G spectrum

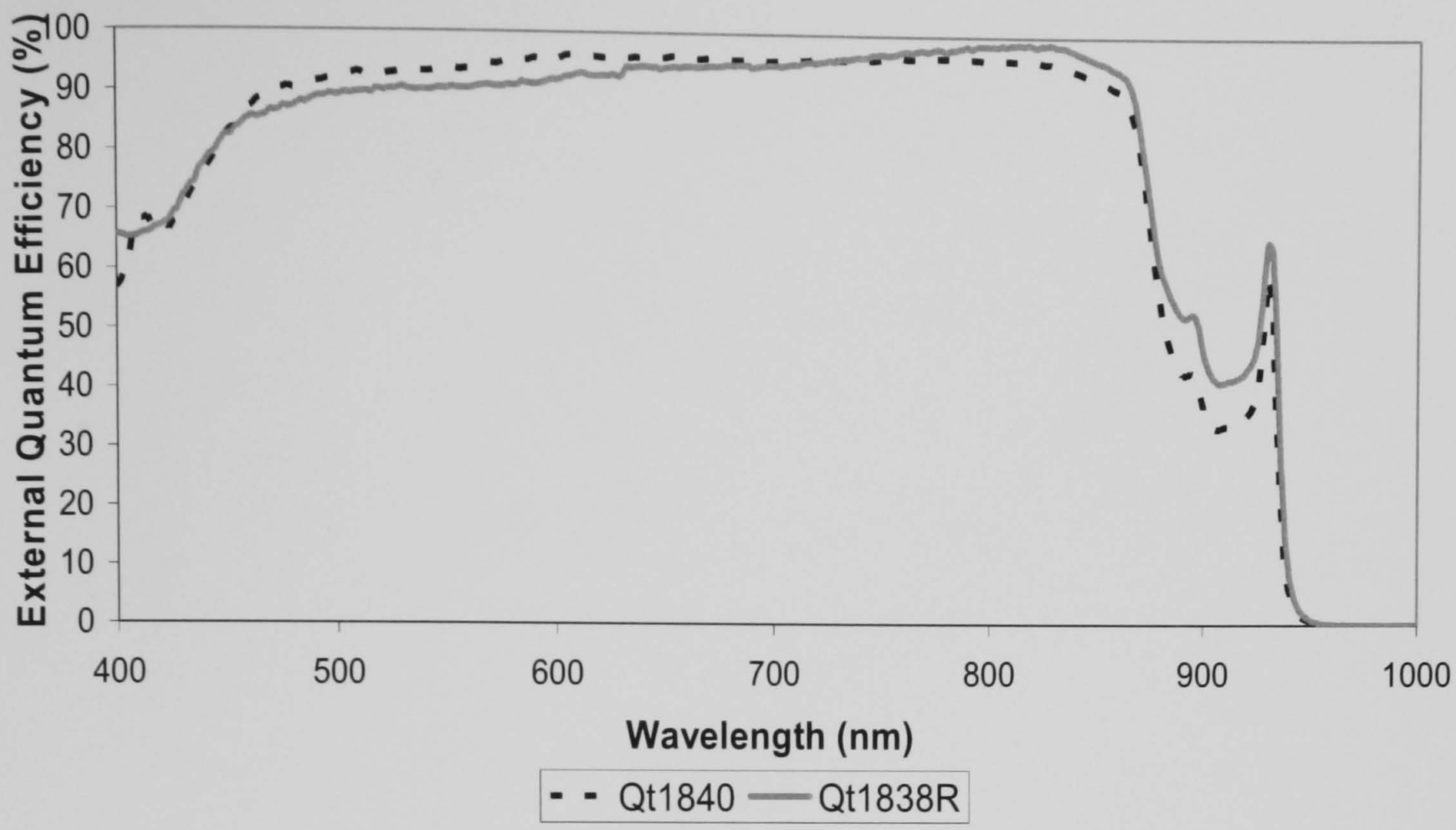

Fig. 3.1.2. Ideal external quantum efficiencies of Qt1840 and Qt1838R

3.1.4.3 Reduced wavelength 65 well cell

In addition to Qt1840 and Qt1838R, a second 65 well sample, Qt1858D, was also characterised. The composition of this cell is also detailed in Table 3.1.1.

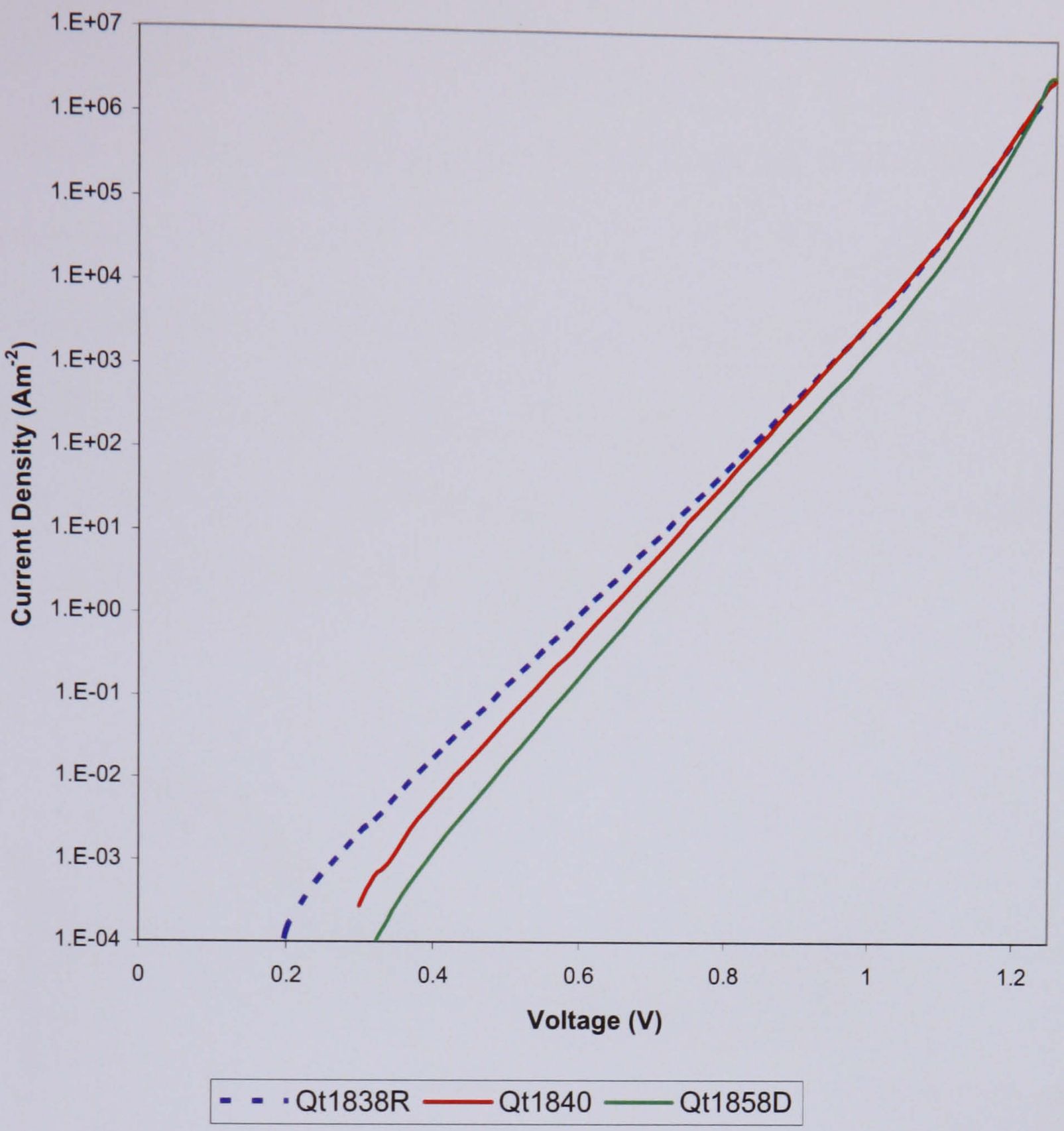

Figure 3.1.3. Dark current densities of Qt1838R, Qt1840 and Qt1858D

The dark current density of Qt1858D is significantly lower than that of both Qt1840 and Qt1838R, as expected for a cell of lower exciton wavelength and hence larger well material bandgap [5]. Although a decrease in J_{sc} would be expected with an decrease in well indium content, the predicted AM1.5G short circuit current of Qt1858D is (284±14) Am^{-2}, the same as that of Qt1840 within errors. This is attributed to the position of the exciton peak of the reduced wavelength sample, which corresponds to a region of higher intensity in the AM1.5g spectrum (see Figure 3.1.4). The small HWHM of the e1-hh1 exciton peaks of these samples are indicative of excellent material quality.

Experimental light IVs for all three samples were obtained using the method outlined in Section 2.3.5 and additivity is tested by comparing these measured light IVs to the short circuit current subtracted from the measured dark current (see Figure 3.1.5). Additivity is very well maintained throughout the light IV plot of Qt1858D, although there is a small difference between predicted and measured maximum power point photocurrent for samples Qt1838R and Qt1840, suggesting a slight loss of field across the i region of these devices (see Figure 3.1.5). Examining the mono IVs of these samples, a slight loss of field is again suggested in Qt1838R (see Figure 3.1.6).

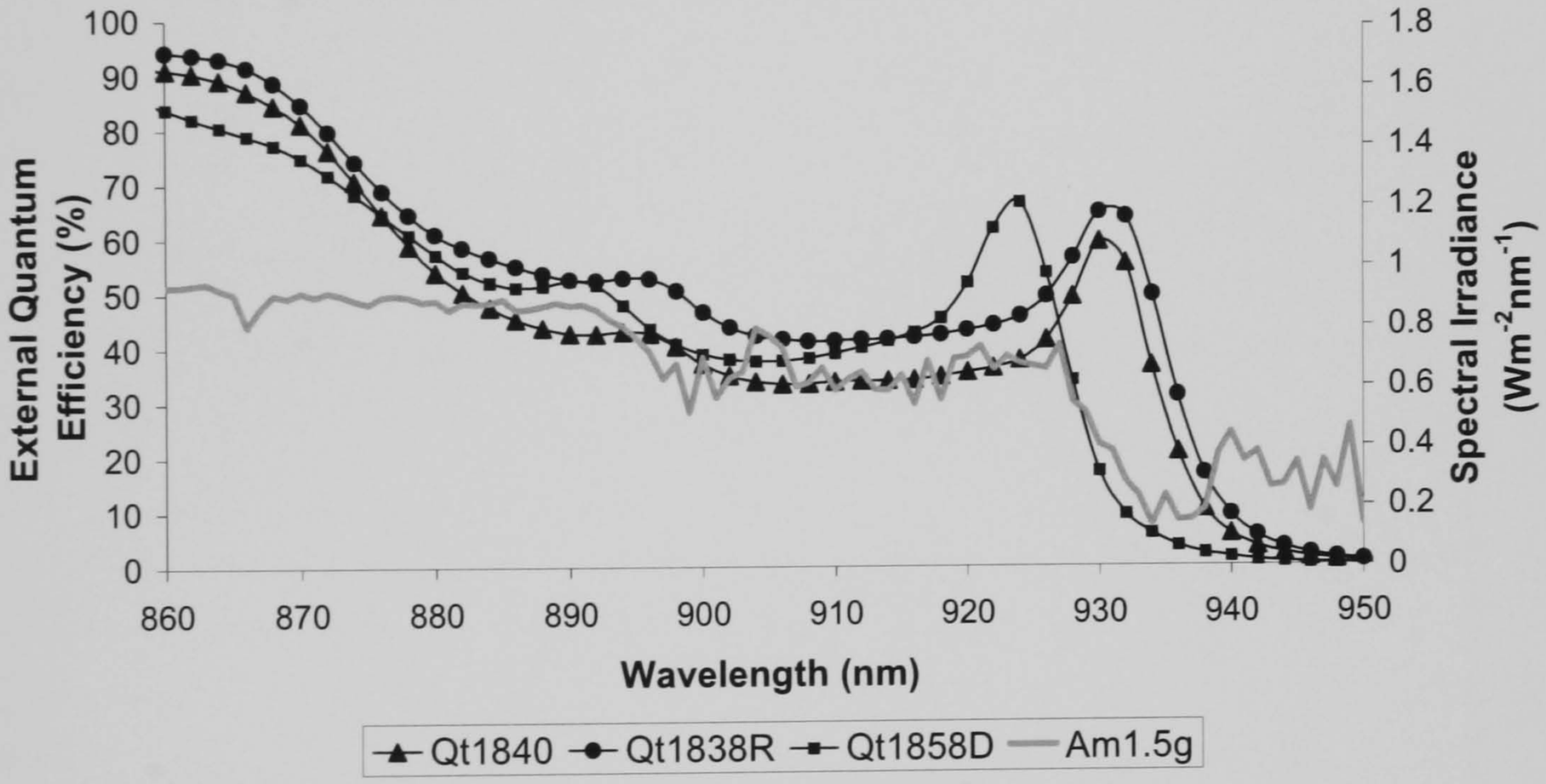

Figure 3.1.4. Ideal external quantum efficiencies of Qt1840, Qt1838R and Qt1858D together with the AM1.5G spectrum [7].

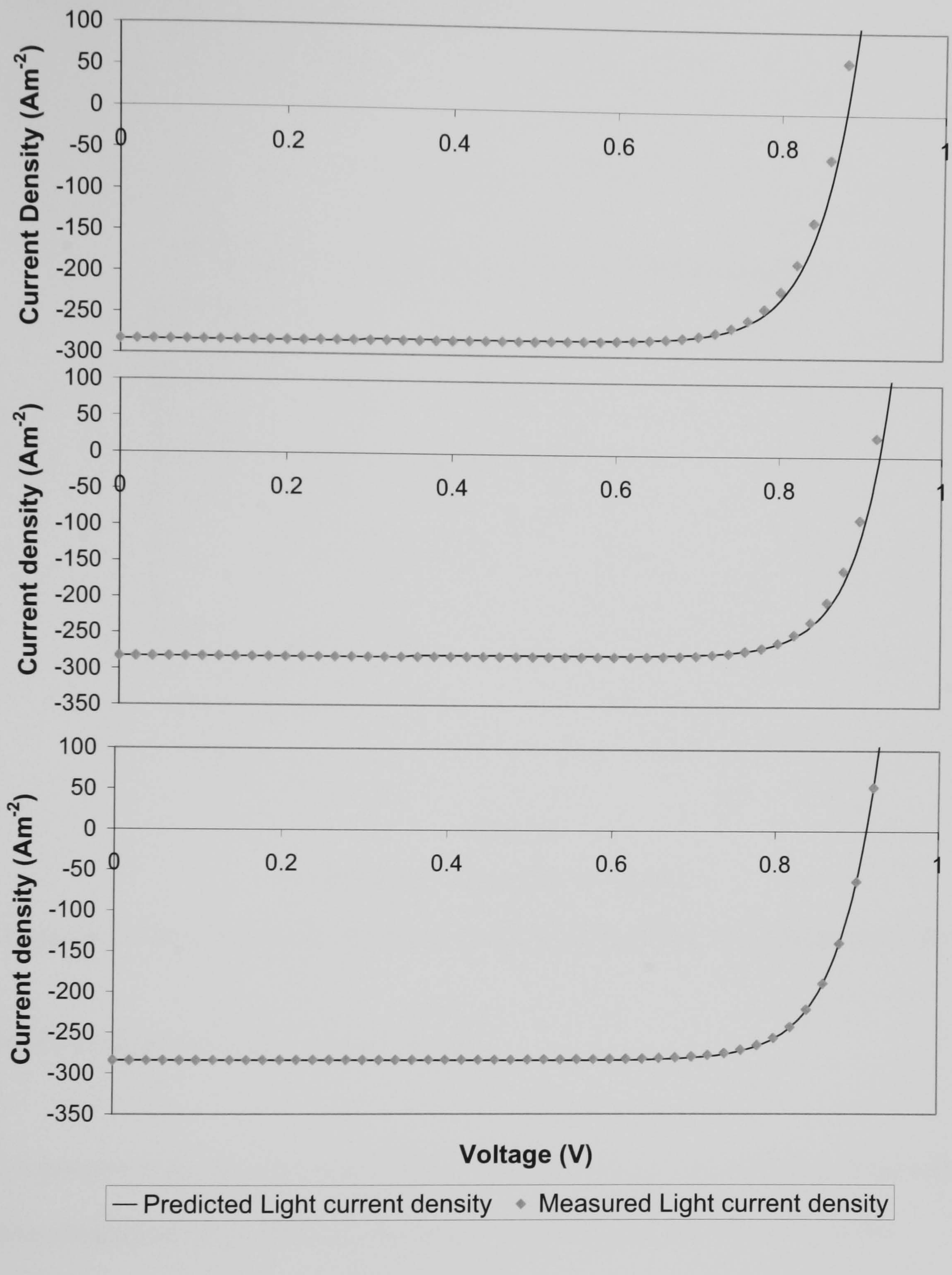

Figure 3.1.5. Predicted and measured light current densities of Qt1858D (bottom), Qt1840 (middle) and Qt1838R (top).

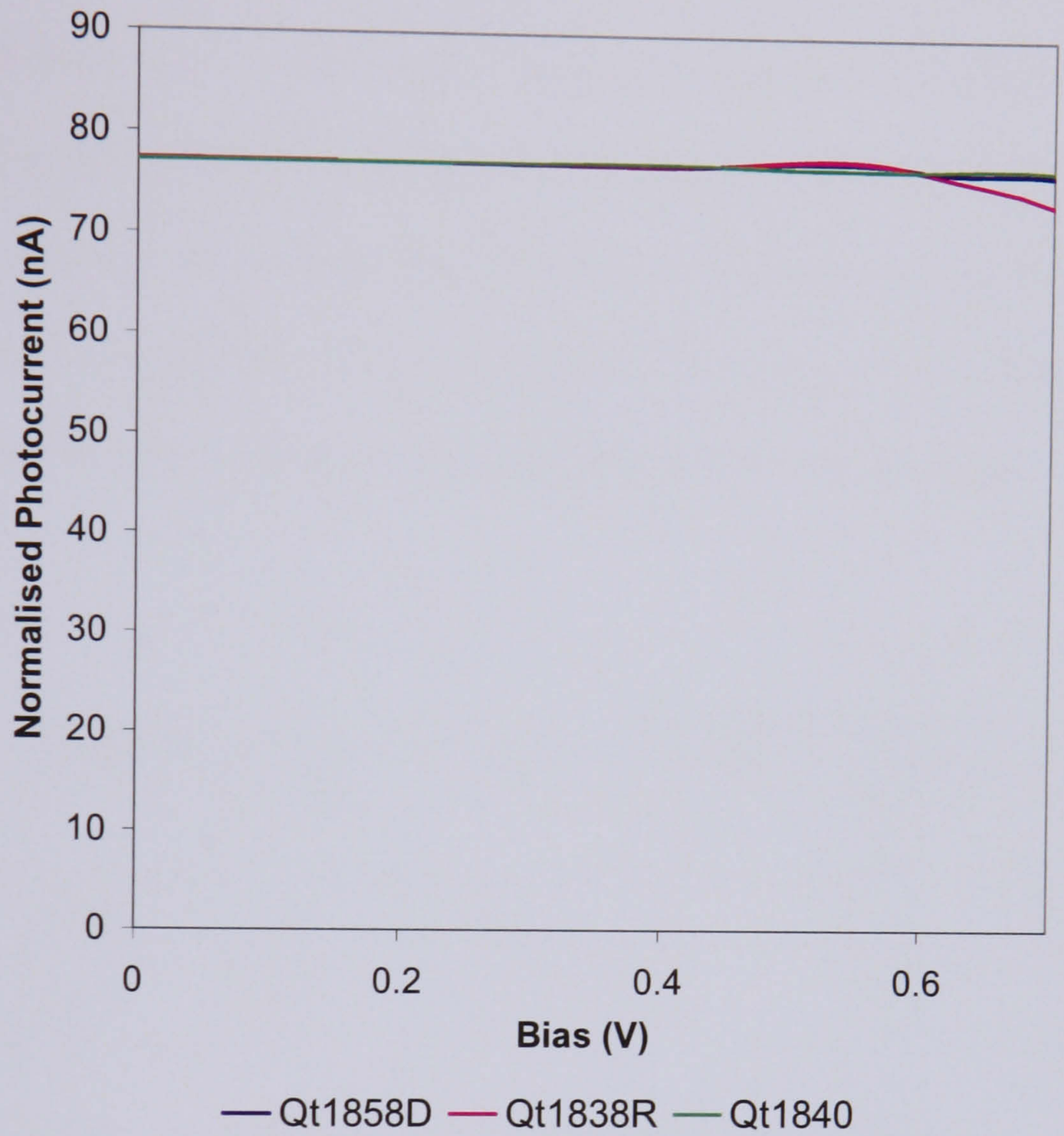

Figure 3.1.6. Monochromatic IVs taken at 600nm for Qt1838R, Qt 1840 and Qt1858D

3.1.4.4 Projected cell efficiencies at one sun

It is possible to use the experimental data to accurately predict the efficiency of the cells when illuminated by an AM1.5g spectrum provided the quantum efficiency of the devices does not change significantly with bias and the dark current densities of the devices do not change significantly with increasing cell size [1]. These are both reasonable assumptions given the good agreement between predicted and measured light currents shown in Figure 3.1.5 and the fact that the dark current density measured in small devices is likely to be higher than that obtained from large area devices due to

edge effects. For the samples with an exciton wavelength of 932 nm (Qt1840 and Qt1838R), the projected AM1.5g efficiency of the 65 well sample is lower than that of the 50 well sample (see Table 3.1.4). It would appear that the slight increase in photocurrent caused by the inclusion of more quantum wells does not compensate for the increased dark current of the 65 well sample. The projected efficiencies of the 50 well sample and the reduced wavelength 65 well sample (Qt1858D) are equal, due to both the low dark current of the reduced wavelength sample, caused by the larger bandgap of the well material, and the maintenance of the same level of photocurrent as Qt1850 caused by more wells and better utilization of the solar spectrum.

Sample	Measured V_{oc} (V)	Predicted V_{oc} (V)	Predicted J_{sc} (Am^{-2})	Measured Fill Factor (%)	Predicted Fill Factor (%)	Projected AM1.5g η (%) (assuming 5% shading)
Qt1838R (65 wells)	0.868	0.881	281±14	79.1	79.7	19.2±0.96
Qt1840 (50 wells)	0.914	0.923	280±14	80.9	81.1	20.7±1.04
Qt1858D (65 wells reduced wavelength)	0.910	0.913	284±14	79.9	80.3	20.7±1.04

Table 3.1.4. Predicted and measured open circuit voltages and fill factors and projected short circuit currents and AM1.5G efficiencies for Qt1858D, Qt1838R and Qt1840.

3.1.5. Conclusions and further work

The photocurrent of a 65 well sample with an exciton wavelength of 932 nm is found to be the same as that of an otherwise identical sample containing only 50 wells, hence this is insufficient to compensate for the higher dark current the 65 well sample possesses. This leads to the 65 well sample having a lower projected AM1.5g efficiency than the 50 well cell. This suggests that to fabricate a SB-QWSC of maximum possible efficiency it may be better to utilise other methods of increasing device absorption than

simply increasing the number of wells. One method of achieving this could be to include a distributed Bragg reflector (DBR) in the on the back of the cells to reflect unabsorbed light and and also to recycle the photons created by radiative recombination [8].

A sample with 65 wells and a reduced exciton wavelength of 924 nm has an equal projected efficiency to the 50 well sample, despite containing more wells, due to its low dark current and high photocurrent resulting from its shorter exciton wavelength which makes better use of the AM1.5g spectrum. Also additivity is demonstrated in the reduced wavelength sample, suggesting that this wafer maintains the field across the i-region at 1-sun intensities despite having 65 wells. Moreover, the excitonic features of this device conclusively demonstrate that it is possible to grow 65 strain balanced well barrier periods using MOVPE and still maintain excellent device quality. In the future several series of varying well number devices are planned for a range of well indium contents to further investigate the optimum well number and composition for SB-QWSCs.

3.2 Cells grown using tertiary butyl arsine

3.2.1 Introduction

As discussed in Chapter 2 the growth of GaAs solar cells utilises arsine (AsH_3) as a source of arsenic. However, arsine is a highly toxic material and therefore particularly undesirable for use in the fabrication of photovoltaic devices which are intended to help safeguard the environment [9]. Several other organic arsenic compounds have been considered as a replacement for arsine in the solar cell growth process. One such group of compounds are the tertiary alkyl arsines (compounds with the chemical formula $CH_3(CH_2)_xAsH_2$). The main advantage of these compounds is that they are less toxic than arsine and therefore easier to store and handle, in addition to having a reduced potential to cause environmental damage. Of the tertiary alkyl arsines, tertiary butyl arsine (TBAs) is believed to be the most suitable substitute for arsine, even though TBAs is slightly more toxic than tertiary methyl arsine and tertiary ethyl arsine, because the strength of the arsine – alkyl bond grows weaker as the alkyl group grows larger [10]. This is due to the fact that TBAs has the lowest dissociation temperature amongst these compounds, which is a beneficial property in semiconductor growth as a reduction in growth temperature minimises both dopant diffusion between different layers and the formation of point defects [11-13]. Also, because TBAs dissociates more readily than arsine, a larger number of hydrogen radicals are formed in the growth process. This lowers the level of carbon and hydrogen contamination in the resulting semiconductor because more of the hydrocarbon radicals formed during the growth process react with hydrogen to form stable hydrocarbon compounds [14]. A significant amount of research material already exists to support the hypothesis that TBAs can be used as a substitute

for arsine in the fabrication of optoelectronic devices without compromising device quality [15,16]

3.2.2 Sample details

In an attempt to assess the suitability of TBAs as a precursor material in solar cell fabrication two otherwise identical p-i-n solar cells where grown, one using arsine and the other using TBAs, and compared. The details of the composition of both samples are given in Appendix 1. Qt1228 (grown using arsine) and Gacell (grown using TBAs) were then processed as AR coated devices using the method outlined in Chapter 2.

3.2.3 Experimental Results

3.2.3.1 Dark Currents

The lowest dark current densities of Qt1228 and Gacell are displayed in Figure 3.2.1.

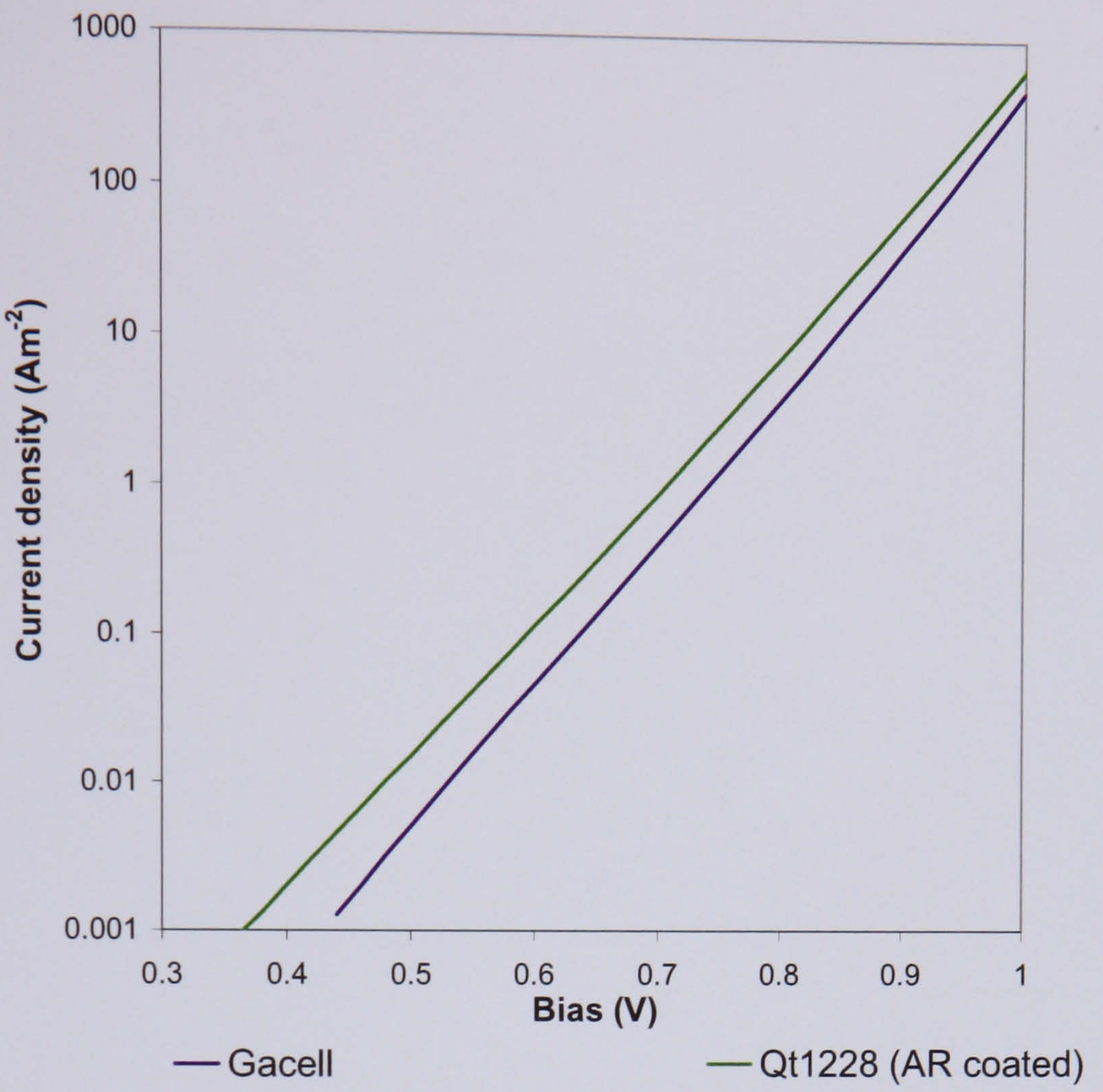

Figure 3.2.1. Dark current densities of the best devices of Qt1228 and Gacell.

The dark current density of Gacell sample is significantly lower than that of Qt1228, suggesting lower contamination levels and hence less recombination via trap states occurring within Qt1228.

3.2.3.2 Quantum Efficiencies and Reflectivities

The internal quantum efficiencies and reflectivities of the best devices of Qt1228 and Gacell are displayed in Figure 3.2.2. Also shown is the reflectivity of an ideal single layer SiN_3 AR coat optimized for 600nm.

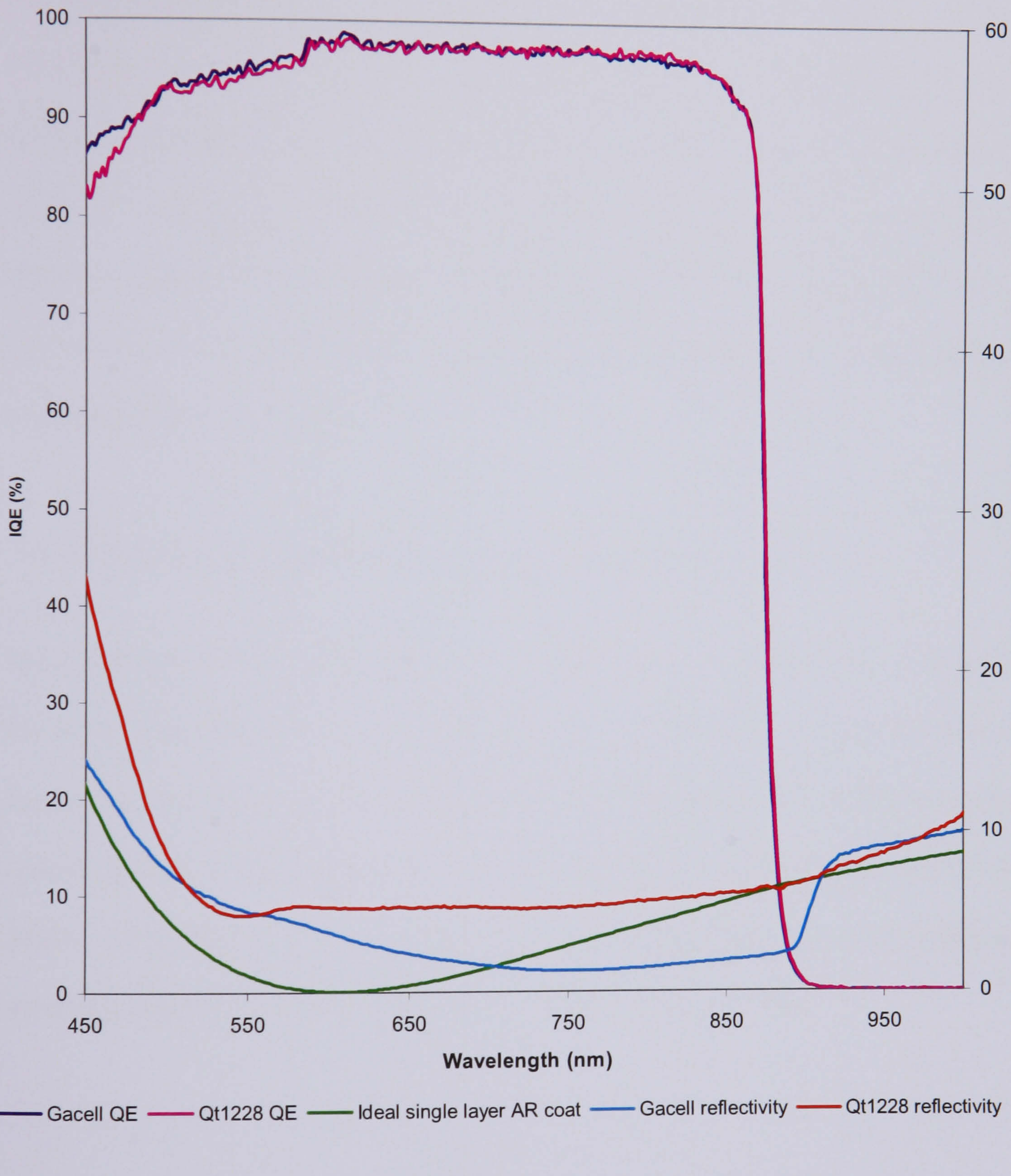

Figure 3.2.2. Internal quantum efficiencies and reflectivities for Gacell and Qt1228 and the reflectivity of an ideal single layer SiN_3 AR coat.

The reflectivity of Gacell reaches a minimum at around 750 nm, a significantly longer wavelength than in an ideal AR coat which would be optimized for 600 nm. Also, a step

in the reflectivity is seen at 900nm (although this is too long a wavelength to affect the internal quantum efficiency.) This is believed to be caused by reflection from the back surface of the double-polished GaAs substrate. The reflectivity of Qt1228 is also unusual as it reaches a minimum at approximately 5% reflectivity and remains relatively unchanged between 550 nm and 750 nm (c.f. the ideal single layer AR coat which has a reflectivity of < 1% at 600nm). The differences between the reflectivities of these samples and an ideal AR coat may be caused by a change in either the layer width or the chemical composition of the AR coat, which would lead to the coat possessing a different refractive index. Despite these differences in reflectivity the IQEs of Gacell and Qt1228 are almost identical, verifying that they possess the same structure and comparable material quality.

3.2.3.3 Light IVs, monochromatic IVs and cell efficiencies

Ideal external quantum efficiencies for both Qt 1228 and Gacell were calculated using the method described in Chapter 2 and were used to calculated the AM1.5g short-circuit current for each device. Again, a front surface metallization of 5% is assumed. Light IV curves (shown in Figure 3.2.3) were obtained for each sample and the projected fill-factors and efficiencies of each sample were calculated and compared. Additionally, monochromatic IVs of both samples were taken (see Figure 3.2.4)

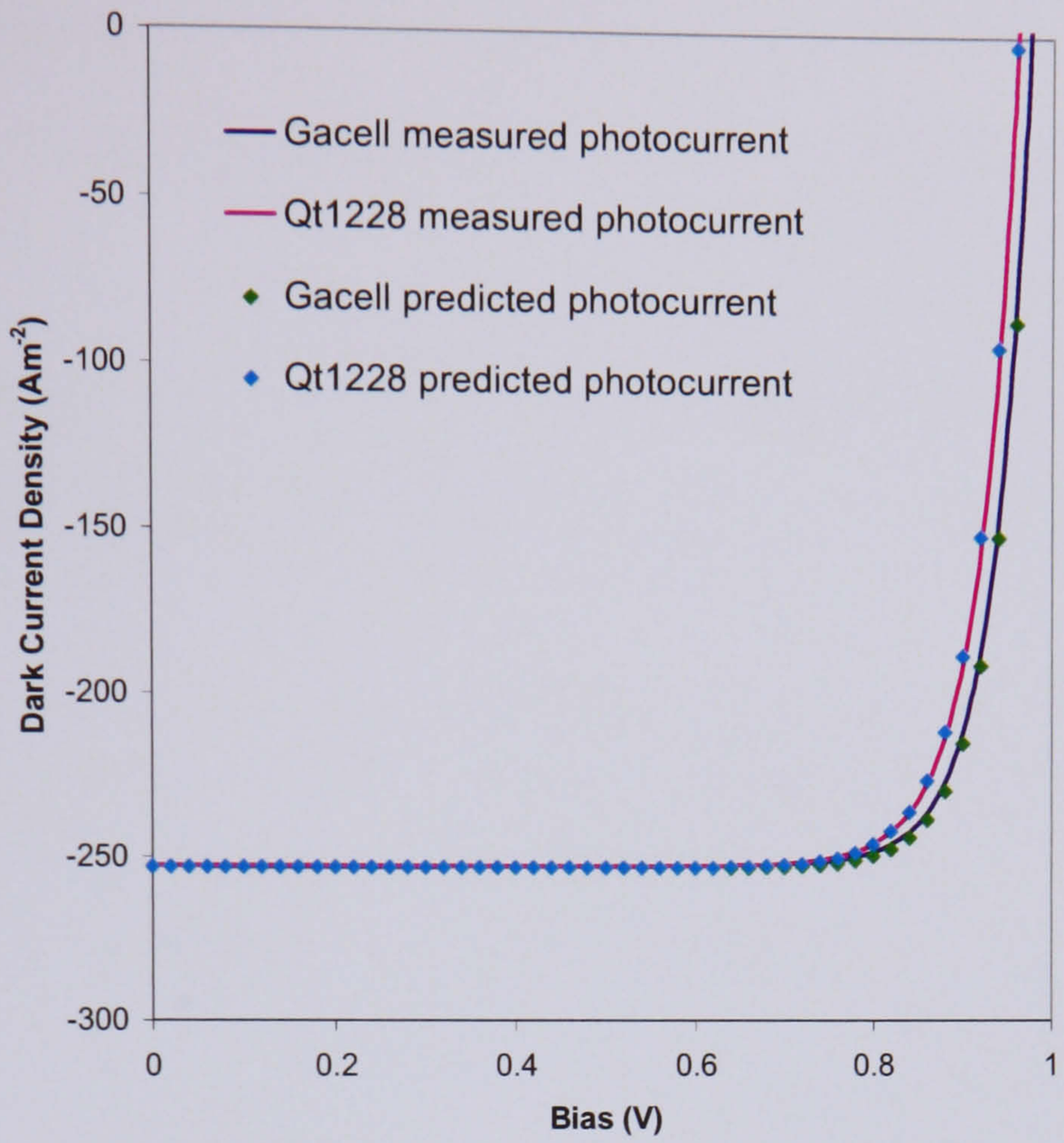

Figure 3.2.3. Light IV curves for Gacell and Qt1228

Both the monochromatic IV measurements and the fact that additivity is maintained in both samples indicate low background doping.

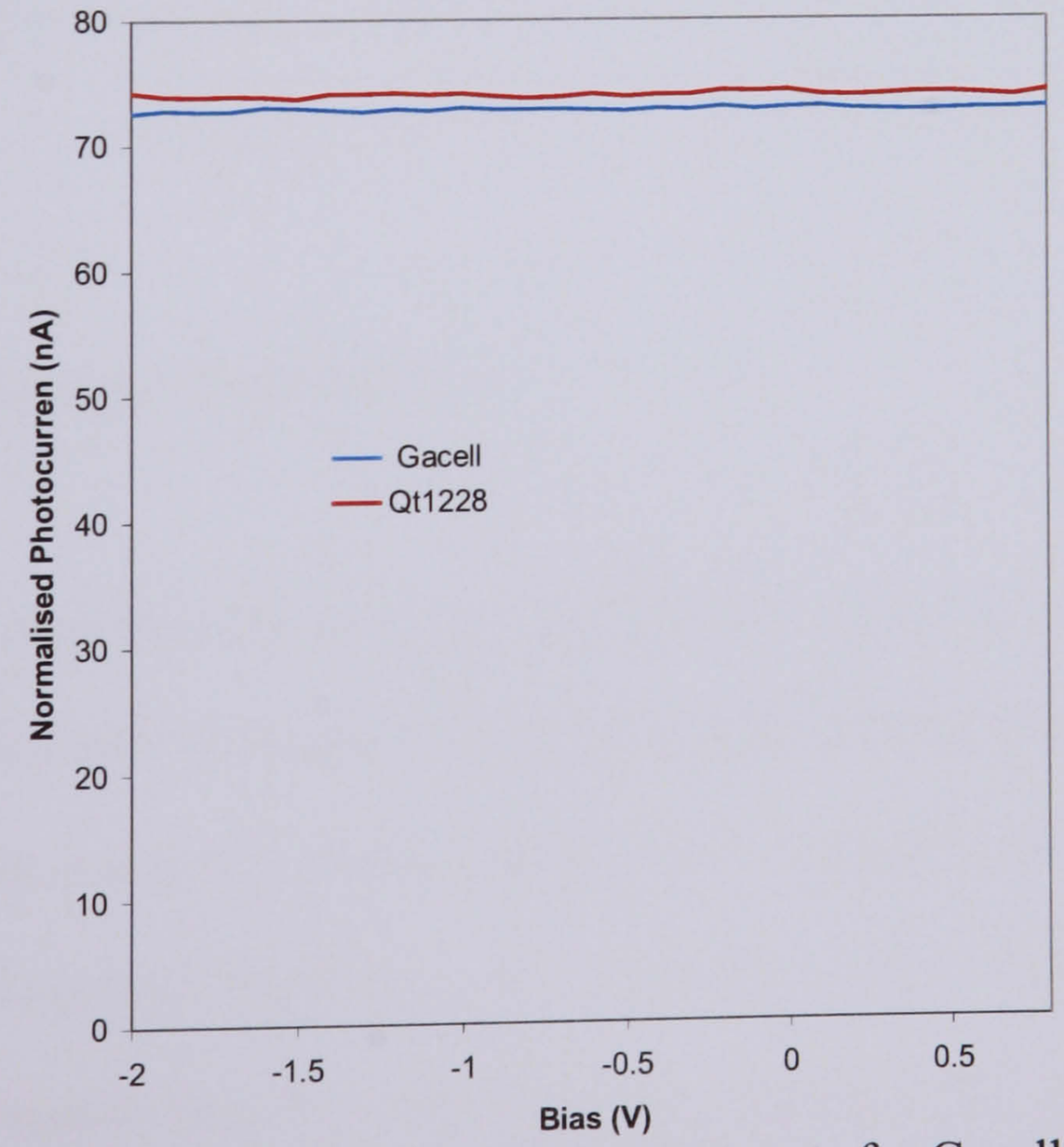

Figure 3.2.4. Monochromatic IV measurements for Gacell and Qt1228

The fill-factor and AM 1.5g projected efficiency of Gacell are the same as those of Qt1228 and Gacell possess a slightly higher open circuit voltage due to its lower dark current (see Table 3.2.1). This suggests that it is possible to substitute arsine with TBAs in the growth process without reducing material quality, and that the use of TBAs may even be preferable to that of arsine.

	Gacell	Qt1228
V_{mp} (V)	0.84	0.82
J_{mp} (Am^{-2})	254±13	254±13
Fill Factor (%)	82.5	81.7
AM1.5g projected efficiency (%)	21.4±1.0	20.9±1.0

Table 3.2.1. Maximum power voltages and current densities, fill-factors and AM1.5g projected efficiencies of Gacell and Qt1228

3.2.4 Conclusions and Further Work

The fill-factors and AM1.5g projected efficiencies of Gacell (grown using TBAs) were found to be the same as those of Qt 1228, an otherwise identical cell grown using arsine. The dark current of Gacell was found to be significantly lower than that of Qt1228, suggesting better material quality, leading to a higher V_{oc} and maximum power voltage. This suggests that TBAs is an effective substitute for arsine in the growth of GaAs solar cells and can be used without reduction in material quality or cell efficiency

and may even lead to an increase in overall cell performance due to a reduction in background doping. The next logical step in this work would be to grow MQW cells using TBAs and compare them to control cells grown using arsine. The low background doping observed in Gacell suggest that this growth technique could also be successfully utilised in the fabrication of multi-quantum well cells. A strain-balanced GaInP/GaAs lattice matched MQW cell has been grown using TBAs but was not fully characterised due to problems with background doping in the device. It is hoped that a new version of this cell will be grown in the near future. It would also be useful to investigate cells grown using TBAs with differing growth temperatures in order to ascertain an optimum growth temperature. Additionally, it would be interesting to study the effects of substituting tertiary butyl phosphine for phosphine in the growth of InGaAs/GaAsP devices [17-19].

References

[1] K.W.J. Barnham and G. Duggan "A New Approach to High-Efficiency Multi-Band-Gap Solar Cells", J. Appl. Phy s **67**. p3490. 1999

[2] N J Ekins-Daukes et al., "Strain-balanced GaAsP/InGaAs quantum well solar cells" Appl. Phys. Lett., **75** (26). p4195-4197. 1999

[3] D.B. Bushnell et al. "Effect of barrier composition and well number on the dark current of quantum well solar cells", J. Appl. Phys. 97, 124908 . 2005

[4] W. Shockley and W T Read Jr. "Statistics of recombination of holes and electrons" Phys Rev., **87**, p835-842. 1952

[5] K.W.J. Barnham et al. "Recent results on quantum well solar cells." Journal of Material Science: Materials in Electronics **11** p531-536. 2000

[6] C. Gueymard et al. "Proposed reference irradiance spectra for solar energy systems testing." Solar Energy **73** (6) p443-467. 2002

[7] J. Nelson et al. "Observation of suppressed radiative recombination in single quantum well p-i-n photodiodes." J. Appl. Phys. **82** (12). 1997

[8] D. Johnson et al. Submitted to the proceedings of the 4th I.E.E.E. World Conference on Photovoltaic Energy Conversion. pp 26-31.2006.

[9] V. Fthenakis et al. "Environmental health and safety issues in III-V solar cell manufacturing." www.pv.bnl.gov/art_168.pdf

[10] Dr Massimo Longo, Istituto Nazionale per la Fisica della Materia, Parma, Italy, private communication.

[11] M. Longo et al. "Controlled intrinsic carbon doping in MOVPE-grown GaAs by using TMGa and TBAs". J Crystal Growth. **248** pp 119-213. 2003

[12] J. Derlyun et al. "Comparison of MOVPE grown solar cells using different substrates and group V precursors." J Crystal Growth. **247** pp 237-244. 2003

[13] C. Agert et al. "High efficiency AlGaAs/GaAs solar cells grown by MOVPE using TBAs at low temperatures and low V/III ratios." Solar Energy Materials and Solar Cells. **66** pp 637-644. 2001

[14] M. Begotti et al. "Electrical and Photoelectrical properties of a GaAs based p-i-n structure, grown at low temperature, by MOVPE, using TBAs, for photovoltaic applications." Submitted to the proceedings of the AIC Conference 2004.

[15] L. Hoffman et al "MOVPE growth of (InGa)P gratings for GaAs based DBR lasers" Proc. IEEE 11th International conference on InP and related materials. p119. 1999

[16] B. Mao et al. "MOCVD-grown 0.25 μm MEFSETs using TBAs as the arsenic source." IEEE Elec. Device Letters. **11** (9). p397-399. 1990.

[17] P. Chan et al. "High performance InP/$Ga_{0.47}In_{0.53}As$/InP metal-semiconductor-metal photodetectors with $Al_{0.1}In_{0.9}P$ barrier enhancement layer." App. Phys. Lett **67** (12), p1715. 1995

[18] Z. Jinghua et al "MOVPE growth of $Al_xIn_{(1-x)}P$ using tertiarybutylphosphine in pure N_2 ambiant " Thin Solid Films. **515**, p4454. 2007.

[19] A. Mathur et al. "Fabrication, Characterization and Analysis of Low threshold current density 1.55 μm strained quantum well lasers." IEEE J. Quant. Elec. 32 (2) p222-226. 1996

4. Modelling the dark currents of strain-balanced multi-quantum well solar cells

4.1 Introduction

As described in Chapter 1, device efficiency and dark current characteristics are inextricably linked. Moreover, a detailed understanding of the radiative portion of the dark current is required to assess device suitability for photon recycling schemes [1]. Significant differences between the dark currents of strained and strain balanced devices are observed due to the larger concentration of defects found in strained samples. Similarly, the dark currents of SB MQW solar cells cannot be directly compared to those of homojunctions due to the differences in bandgap between these two types of devices [2].

It should be noted that the work detailed in this chapter was carried out before the refinements documented in Chapter 5. Hence the absorption in the i region of the cell is calculated by assuming a starting value of 1% per level per well and then adjusting this value to produce a theoretical QE that fits well to the experimental results. Additionally, precise compositions of the samples studied in this chapter have yet to be determined using the improved model of the confined states in the quantum wells.

4.2 Overview of dark current model

The dark current of a multi-quantum well solar cell may be evaluated by separately considering the dark current in the depletion region and in the field free regions of the cell. The current originating from the depletion region results from the recombination of electrons and holes in the wells and barriers. This current has both a radiative and non-radiative component [3]. An expression for the radiative component is derived using

Detailed Balanced Theory [4] which states that the absorptivity and emissivity of any material in quasi-thermal equilibrium are equal. The radiative current is thus given by [5]

$$J_{rad} = \int_0^{\infty} \int_s a(E, \vartheta, s) F(E, \Delta E_F) d\Omega . dS . dE \qquad (4.1)$$

where $a(E, \theta, s)$ is the probability that a photon of energy E will be emitted on some point on the surface, s, at angle θ to normal incidence, and $F(E, \Delta E_F)$ is the spectral photon flux density due to spontaneous emission at s, and ΔE_F is the quasi-Fermi level separation [5].

The flux $F(E, \Delta E_F)$ is determined by evaluation of the generalised Planck expression for spontaneous emission from a non-black body

$$F(E, \Delta E_F) dE = \frac{2 n_r^2 E^2}{h^3 c^2 (\exp[(E - \Delta E_F) / kT] - 1)} dE \qquad (4.2)$$

where $F(E, \Delta E_F)$ is the flux emitted from the body, ΔE_F the quasi-Fermi level separation, n_r the refractive index of the medium surrounding the body, h is Planck's constant, c the speed of light, k is Boltzmann's constant and T is absolute temperature [6].

Due to the circular shape of the solar cells under consideration and the fact that any emission from the sides of the device is believed to be negligible, the surface integral in Equation 4.1 may be expressed as

$$\int_s a(E, \theta, s) d\Omega . dS = \int_S \int_0^{\theta_c} a(E, \theta, s) \cos\theta (2\pi \sin\theta d\theta) ds = a_{tot} \qquad (4.3)$$

When calculating the total emissivity of the solar cell, photon emission under three different sets of circumstances are considered (see Figure 4.1).

1. Photons emitted from the front surface. Due to the semiconductor-air interface photons emitted at the front surface are subject to a critical angle, beyond which no emission at the front surface takes place. The emission from the front surface is thus

$$a_{front}(E, \theta) = (1 - r(E, \theta)[1 - \exp\left(\frac{-\alpha z}{\cos \theta}\right)] \qquad \text{for } 0 < \theta < \theta_c \quad (4.4)$$

where α is the absorbance of the sample which is obtained by fitting the quantum efficiency as described above.

2. Photons emitted at the back surface. The back surface of the solar cell consists of the interface between the GaAs n region and substrate, which are assumed to have identical refractive indices. Therefore, there is no critical angle for photon emission at the back surface. The emission from the back surface is sub-divided into two sections.

   i. Photons that have impinged on the front surface with an incident angle greater than θ_c, which are all lost through the back surface apart from those that are reabsorbed in the cell.

   ii. Secondly, photons with an incident angle less than θ_c, of which only the reflected fraction are loss at the back surface. The total emission from the back surface is thus

$$a_{back}(E, \theta) = [1 - \exp\left(\frac{-2\alpha z}{\cos \theta}\right)] \qquad \text{for } \theta > \theta_c \quad (4.5)$$

and

$$a_{back}(E, \theta) = r(E, \theta)[1 - \exp\left(\frac{-2\alpha z}{\cos \theta}\right)] + (1 - r(E, \theta))[1 - \exp\left(\frac{-\alpha z}{\cos \theta}\right)] \qquad \text{for } \theta < \theta_c \quad (4.6)$$

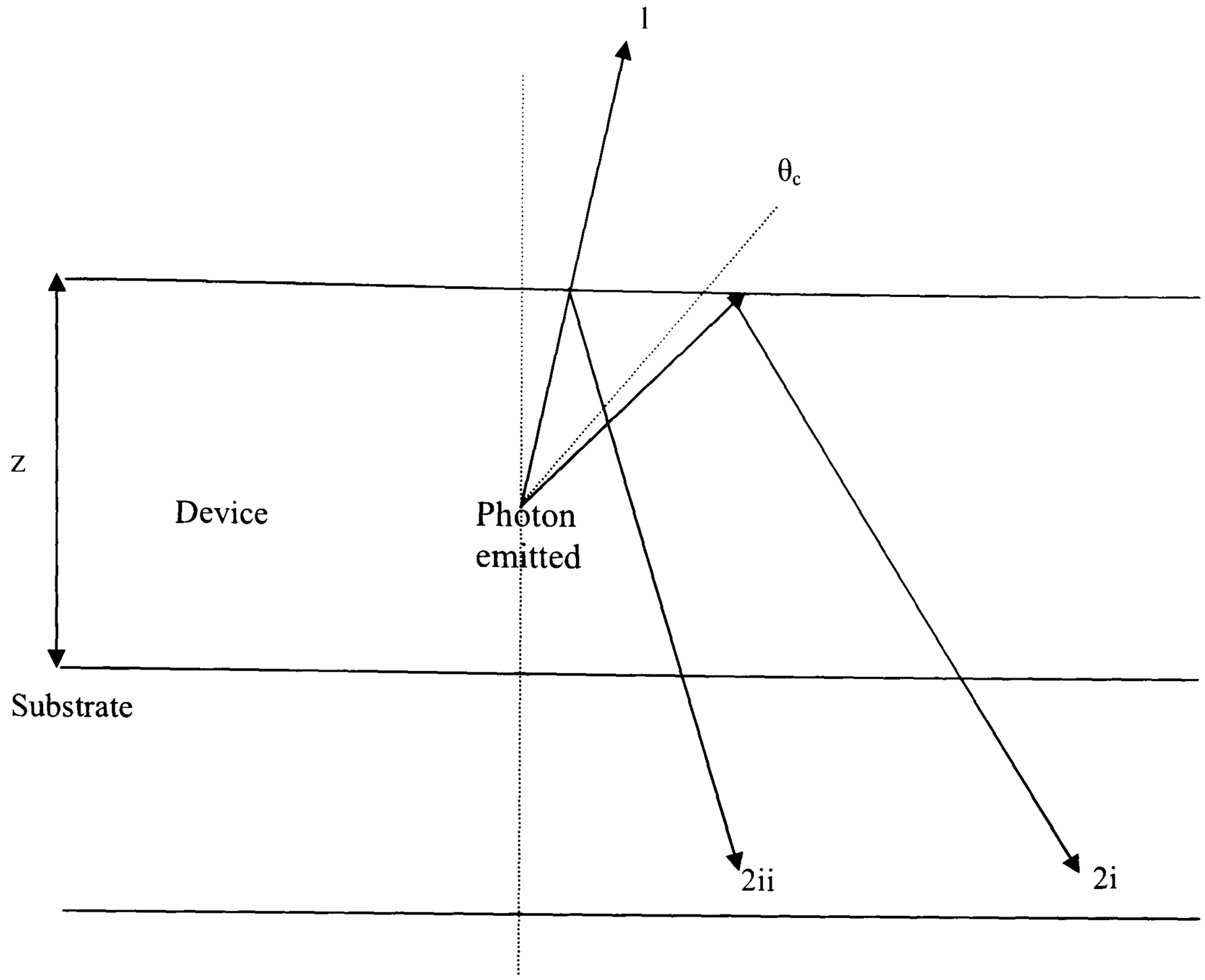

Figure 4.1. Schematic of the possible paths a photon emitted forward from a typical MQW device might take.

Substituting Equations 4.4, 4.5 and 4.6 into Equation 4.3 and changing the angular integration variable from θ to $cos(\theta)$ gives

$$
\begin{aligned}
a_{tot} &= 2\pi A_b \int_0^{\cos\theta_c} \left[1 - \exp\left(\frac{-2\alpha z}{\cos\theta}\right)\right] \cos\theta d(\cos\theta) \\
&+ 2\pi A_b \int_{\cos\theta_c}^{1} \left[1 - \exp\left(\frac{-\alpha z}{\cos\theta}\right)\right]\cdot\left[1 + r(E,\theta)\left(\frac{-\alpha z}{\cos\theta}\right)\right] \cos\theta d(\cos\theta) \qquad (4.7) \\
&+ 2\pi A_f \int_{\cos\theta_c}^{1} \cdot\left[1 - r(E,\theta)\left(\frac{-\alpha z}{\cos\theta}\right)\right] \cos\theta d(\cos\theta)
\end{aligned}
$$

where A_f and A_b are the areas of the front and back surfaces respectively [5].

Hence

$$J_{rad} = \frac{a_{tot} 2n^2 E^2}{h^3 c^2 (\exp[(E - \Delta E_F) / kT] - 1)} dEd(\cos\theta) \tag{4.8}$$

The non-radiative component of the dark current in the depletion region arises from the Shockley-Hall-Read recombination of carriers via mid-gap trap states. The current is given by [3]

$$J_{SHR} = -q \int_{-w_p}^{w_n} U(x) dx \tag{4.9}$$

where q is the magnitude of the electronic charge, w_n and w_p the limits of the depletion region and $U(x)$ is the Shockley-Hall-Read recombination rate which is given according to Reference 7 by:

$$U(x) = \frac{n_e p - n_i^2}{\tau_n (p + p_t) + \tau_p (n + n_t)} \tag{4.10}$$

where n_e and p are the densities of electrons and holes per unit volume, n_i the intrinsic carrier density, τ_n and τ_p the lifetimes of electrons and holes within the trap state, and n_t and p_t the carrier density when the carrier Fermi level is equal to the level of the interband trap [8]. For low indium and phosphorus fractions in our strain-balanced cells we find that it can be assumed τ_n is equal to τ_p [9]

The n=1 dark current of the minority electrons in the p region is given by

$$J_n(x) = qD_n \frac{dn}{dx} + q\mu_n F_n \tag{4.11}$$

where D_n is the electron diffusion coefficient, dn/dx the electron concentration gradient, μ_n is the electron mobility and F_n the electric field [8].

Similarly, the dark current of the minority holes in the n region is given by

$$J_p(x) = qD_p \frac{dp}{dx} + q\mu_p F_p \tag{4.12}$$

where D_p is the hole diffusion coefficient, *dp/dx* the hole concentration gradient and μ_p is the hole mobility.

In the charge neutral regions of the solar cell where no electric field is present the dark current is purely diffusive. Equations 4.11 and 4.12 therefore become

$$J_n(x) = qD_n \frac{dn}{dx} \tag{4.13}$$

$$J_p(x) = qD_p \frac{dp}{dx} \tag{4.14}$$

Solving Equations 4.13 and 4.14 with the appropriate boundary conditions leads to

$$J_n(x) = \frac{qD_n n_{p0}}{L_n} (e^{\frac{qV}{kT}} - 1) \tag{4.15}$$

and

$$J_p(x) = \frac{qD_p p_{no}}{L_p} (e^{\frac{qV}{kT}} - 1) \tag{4.16}$$

where n_{p0} and p_{n0} are the equilibrium electron and hole densities in the p and the n regions respectively, n_i is the intrinsic carrier density and L_n and L_p are the diffusion lengths of electrons and holes [10] (determined from fitting the quantum efficiency of the sample [3].)

There is also a small portion of the dark current that arises from recombination at the front and back surfaces of the device [3]. This is derived from the product of the excess minority carrier concentration in equilibrium and the surface recombination velocities. Thus the total ideal Shockley dark current modified to take surface recombination into account is then [4]

$$J_{IS}(x) = (e^{\frac{qV}{kT}} - 1)\left[\frac{qni_p^2 D_n}{N_A L_n} + \frac{qni_n^2 D_p}{N_D L_p} + S_N \frac{qni_p^2}{N_A} e^{-\frac{x_p}{L_N}} + S_P \frac{qni_n^2}{N_D} e^{-\frac{x_n}{L_p}}\right] \quad (4.17)$$

where S_N and S_P are the surface recombination velocities at the back and front surface, N_A and N_D are the acceptor and donor concentrations, ni_n and ni_p are the intrinsic carrier densities in the n and the p region and x_n and x_p are the widths of the charge neutral n and p region.

The total dark current within the solar cell is thus given by

$$J_{tot}(x) = J_{IS} + J_{SHR} + J_{rad} \quad (4.18)$$

4.3 Experimental details

The dark currents of a number of samples were measured using the method detailed in Chapter 2. A series of shallow well $In_xGaAs/GaAsP_y$ ($x \approx 0.1$ and $y \approx 0.09$) samples with well numbers between 1 and 50 were studied, in addition to an intermediate well depth sample ($x \approx 0.13$ and $y \approx 0.08$) containing 50 wells. A deep well series of 20, 30 and 40 well devices ($x \approx 0.17$ and $y \approx 0.07$) was also examined.

Measured dark currents were obtained for between 8 and 18 samples were obtained for each sample and were fitted using the iterative computer program described in Chapter 2 with n_1 fixed at unity and n_2 allowed to vary . The zero bias intercept of the $n_1 = 1$ portion of the dark current was obtained and used to estimate the $n_1 = 1$ reverse saturation currents. Errors on these values were obtained by finding the highest and lowest intercept that corresponded to a reasonable fit to the experimental data.

4.4 Results

The $n_1 = 1$ intercepts of several samples of varying well number are plotted against the energy of the e1-hh1 exciton in Figure 4.2. If the $n_1 = 1$ dark current were dominated by the Ideal Shockley contribution the intercepts would be directly proportional to square of the intrinsic carrier density and hence the exponential of the device bandgap, denoted by the dashed line in Figure 4.2. It is evident that the intercepts are significantly lower than predicted by this relationship, substantiating the hypothesis that the $n_1 = 1$ dark current cannot be fully described by the Ideal Shockley model.

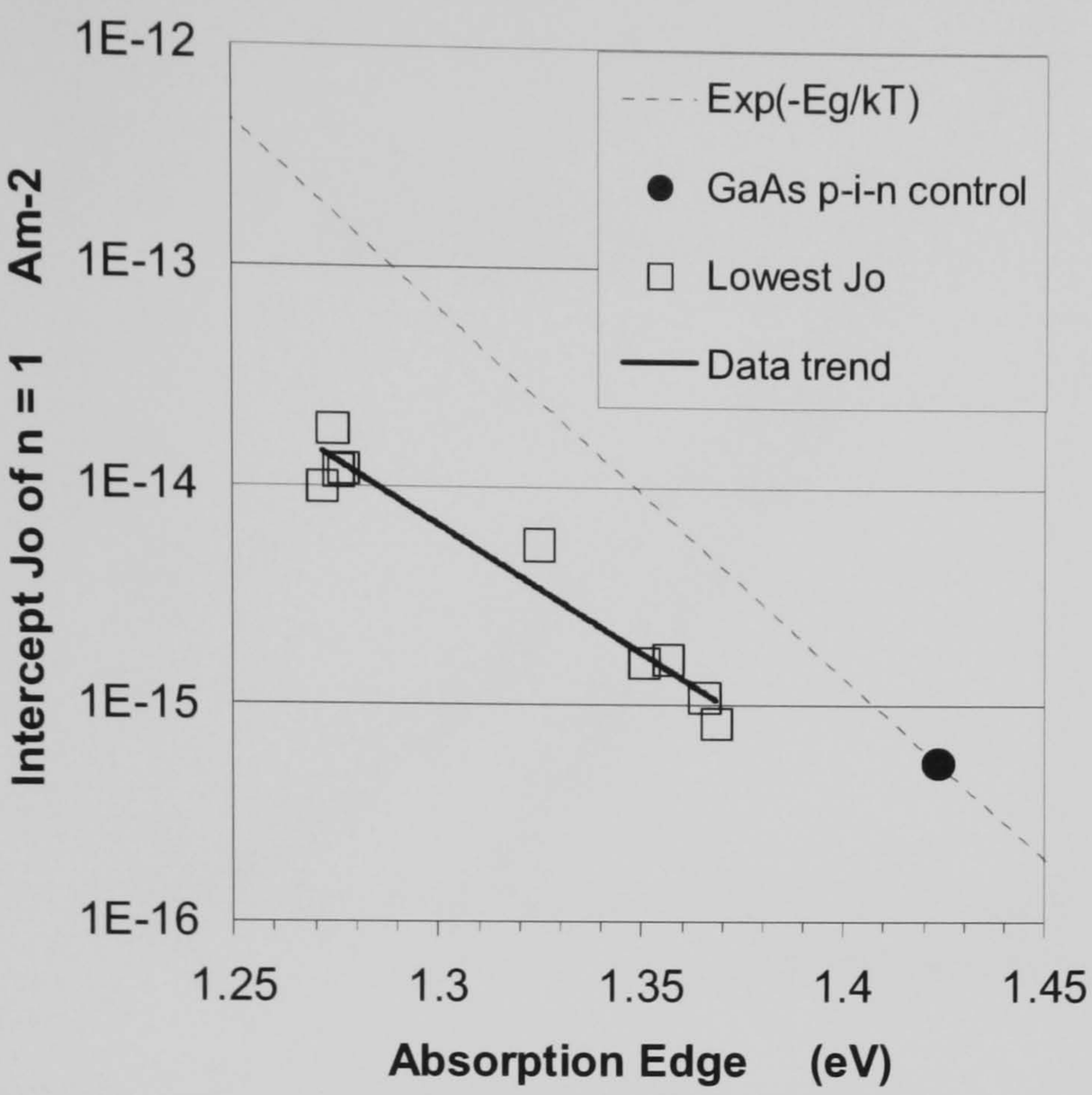

Figure 4.2.The $n_1 = 1$ intercepts of several SB-MQW solar cells plotted as a function of e1-hh1 excition energy. Also shown is the exponential of the bandgap of the well material (dashed line) [2].

A measured dark current for a 50 shallow well sample is displayed in Figure 4.3. Good agreement is observed between the experimental results and the output of the model.

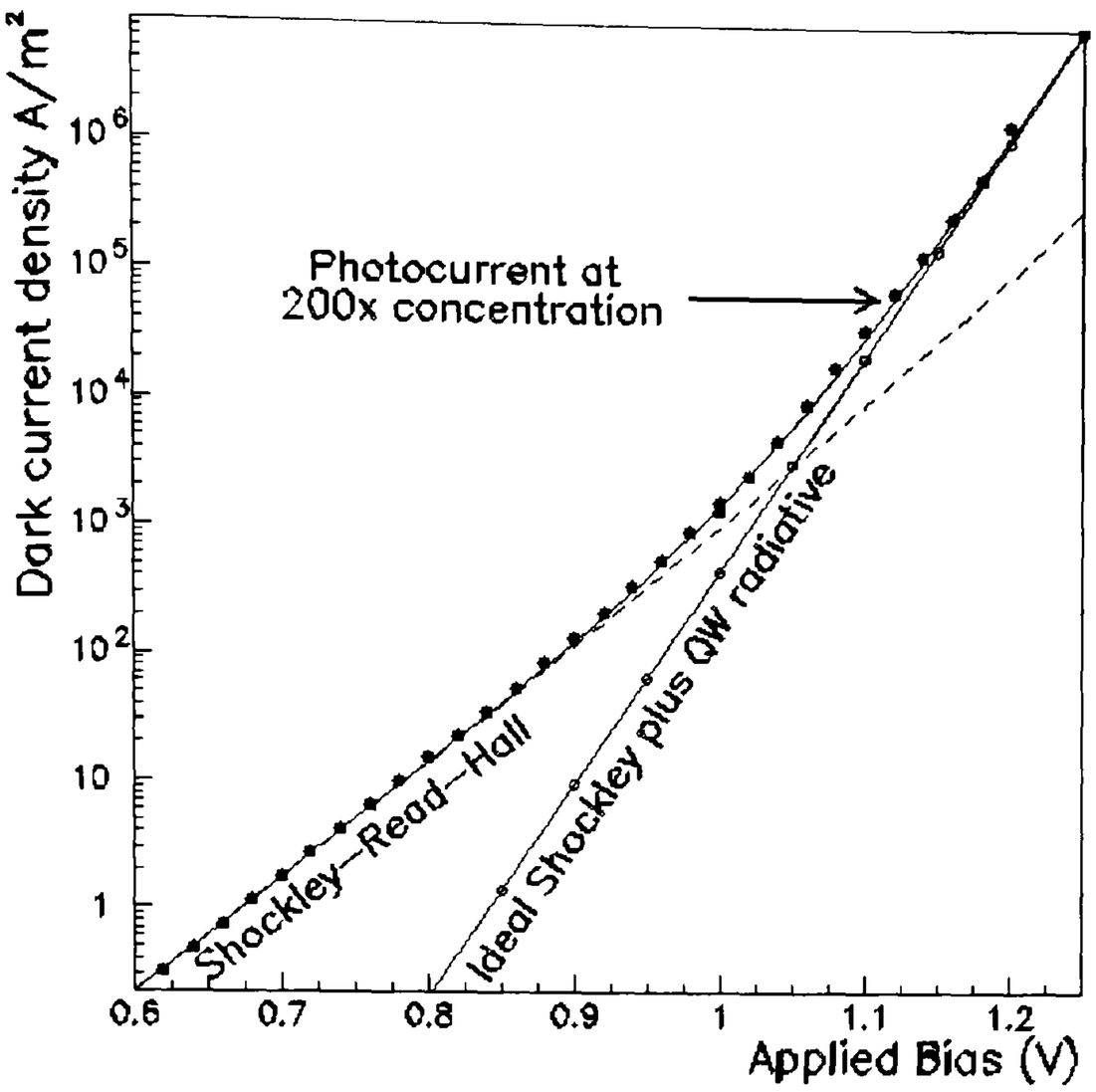

Figure 4.3. A measured dark current (solid dots) and the output of the dark current model [2].

The sum of the reverse saturation currents of the QW radiative and Ideal Shockley portions of the dark current calculated using the model and the mean $n_1 = 1$ intercepts obtained from fitting measured dark currents are compared in Figure 4.4. Again, good agreement is observed between the measured results and the model. It is interesting to note that for a given well depth the intercept displays only a weak dependence on well number.

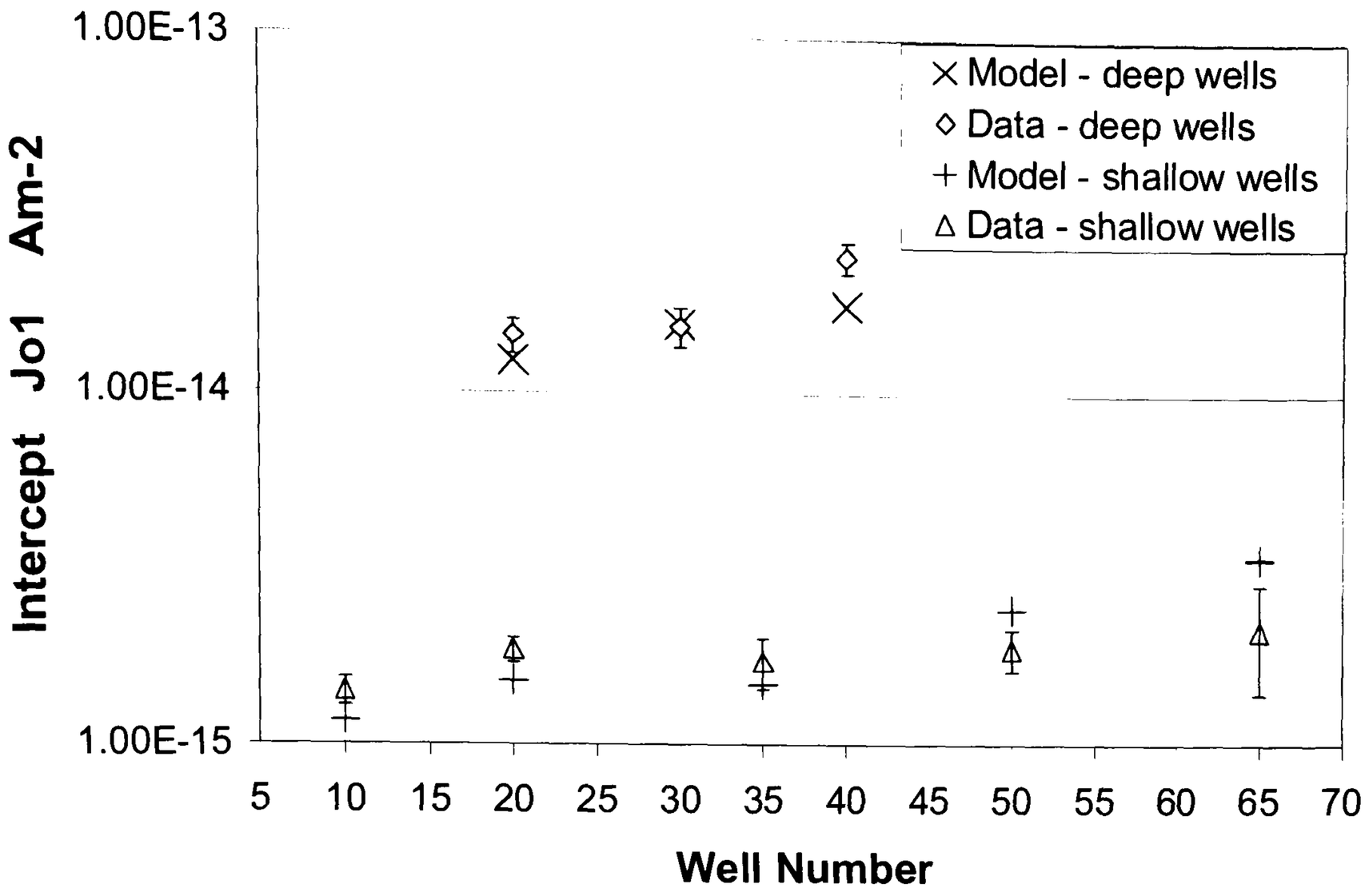

Figure 4.4. The mean $n_1 = 1$ intercepts obtained from fitting measured dark currents with Equation 1.5 compared to the sum of the QW radiative and Ideal Shockley portions of the dark current as a function of well number [2].

The ratio of the QW radiative intercept to the sum of the QW radiative intercept and the Ideal Shockley intercept is shown in Figure 4.5. The QW portion of the dark current is seen to increase with increasing well depth, becoming almost the entire contribution to the $n_1 = 1$ dark current for deep wells, suggesting that deeper well devices are more suited to use in photon recycling schemes. Again, for a given device bandedge the ratio is only weakly dependent on well number.

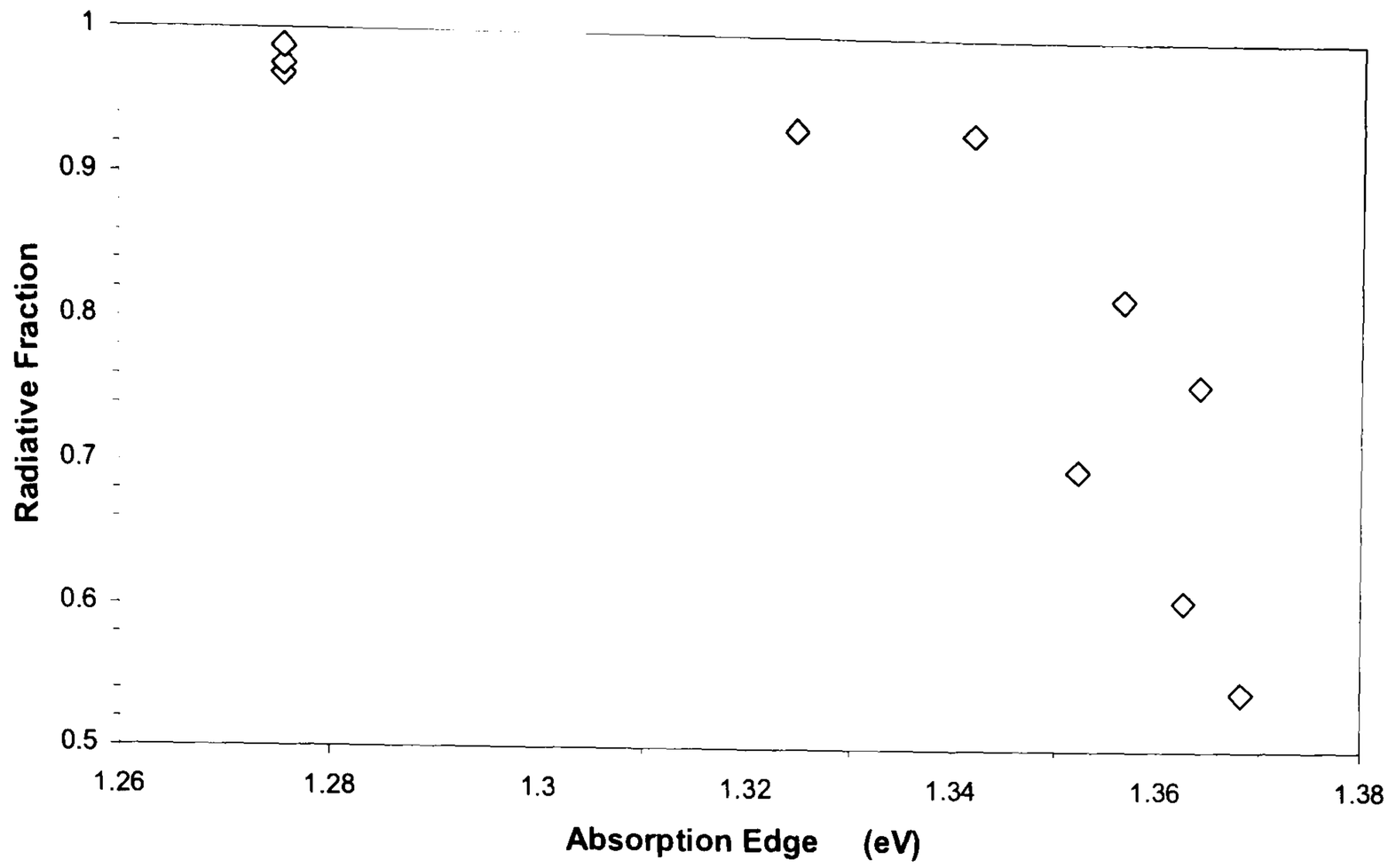

Figure 4.5. Ratio of the QW radiative intercept to the sum of the QW radiative and Ideal Shockley intercepts [2].

4.5 Conclusions and further work

The $n_1 = 1$ intercepts of a variety of SB-MQW solar cells were determined by fitting a double exponential to measured dark currents. The intercepts of these devices are found to be significantly different to those expect if the $n_1 = 1$ dark current were comprised solely of the Ideal Shockley current. We conclude that the $n_1 = 1$ dark currents of SB-MQW solar cells have two components; the Ideal Shockley dark current and a contribution arising from radiative recombination in the quantum wells. Good agreement is observed between the output of this model and measured device dark currents. The $n_1 = 1$ intercepts obtained from fitting experimental dark currents are also found to be in good agreement to those predicted by the model. The QW radiative fraction of the $n_1 = 1$ dark current is found to become dominant as well depth increases.

Clearly, the work documented in this chapter should be revised using the updated model for device absorption detailed in Chapter 5. It would also be useful to include the more accurate insight into device composition obtained using the new model for strain bandgaps and confined states. The comparison between the $n_1 = 1$ intercepts obtained from fitting experimental results and those predicted by the model could be extended to include a larger number of devices with a greater range of well numbers and depths. It would also be interesting to determine whether the QW radiative fraction of the $n_1 = 1$ dark current increases further towards unity as well depth continues to increase.

References

[1] D. Johnson et al.,Proceedings of the 4th I.E.E.E. World Conference on Photovoltaic Energy Conversion. pp 26-31., 2006.

[2] K.W.J. Barnham et al. "Observation of Ideal Dark-current behaviour in Strain-balanced Quantum Well Solar Cells", Proc. 19th European Photovoltaic Solar Energy Conf. Paris, pp, 328 – 331, 2004.

[3] J.P.Connolly et al.,"Efficiency Limits of Quantum Well Solar Cells", Proc. 19th European Photovoltaic Solar Energy Conf. Paris, pp 355 – 358, 2004.

[4] G. Araujo and A. Marti. "Absolute Limiting Efficiencies for Photovoltaic Energy Conversion." Sol. Energy Mater. Sol. Cells, 33, p 213. 1994

[5] J. Nelson *et al.* "Observation of Suppressed Radiative Recombination in Single Quantum Well p-i-n Diodes. **82** 12. p 6240. 1997.

[6] Tiedje *et al.*,"Limiting Efficiencies of Silicon Solar Cells." IEEE Trans. Electron Devices **31** (5), p711. 1984

[7] W. Shockley and W. Read. "Statistics of Recombination of Electrons and Holes." Phys. Rev. **82**:pp 835–842, 1952.

[8] J. Nelson. "Physics of Solar Cells" IC Press. 2002

[9] J. Connolly. "Simulating Multiple Quantum Well Solar Cells." Proc. 28th IEEE Photovoltaic Specialists Conference, Anchorage, Alaska, USA. p. 1304-1307. 2000.

[10] S. Sze. "Semiconductor devices; physics and technology." Wiley Interscience. 1981

5. Modelling the quantum efficiency of strain balanced multi-quantum well solar cells

5.1 Overview of original model

In order to produce photovoltaic devices of maximum possible efficiency it is essential to be able to model accurately the quantum efficiency (QE) of such devices in order to predict the photocurrent produced. Furthermore, as described in Chapter 4, the calculation of device absorption necessary for the QE model allows calculation of the radiative portion of the dark current [1] which forms the basis of quasi Fermi level studies [2].

To model quantum efficiency one must first calculate the photocurrent of the device. The photocurrent arising from the depletion region of an MQW device is proportional to the integral over the depleted region of the product of the absorption in the layer (α_i) and the flux at the surface of the depletion region [3]

$$J_{dr} \propto \int_0^{w_n + w_i + w_p} \alpha_i F_i dx \tag{5.1}$$

where F_i is the flux at the surface of the depletion region, x denotes position within the depleted region and w_p, w_i and w_n are as defined in Figure 5.1

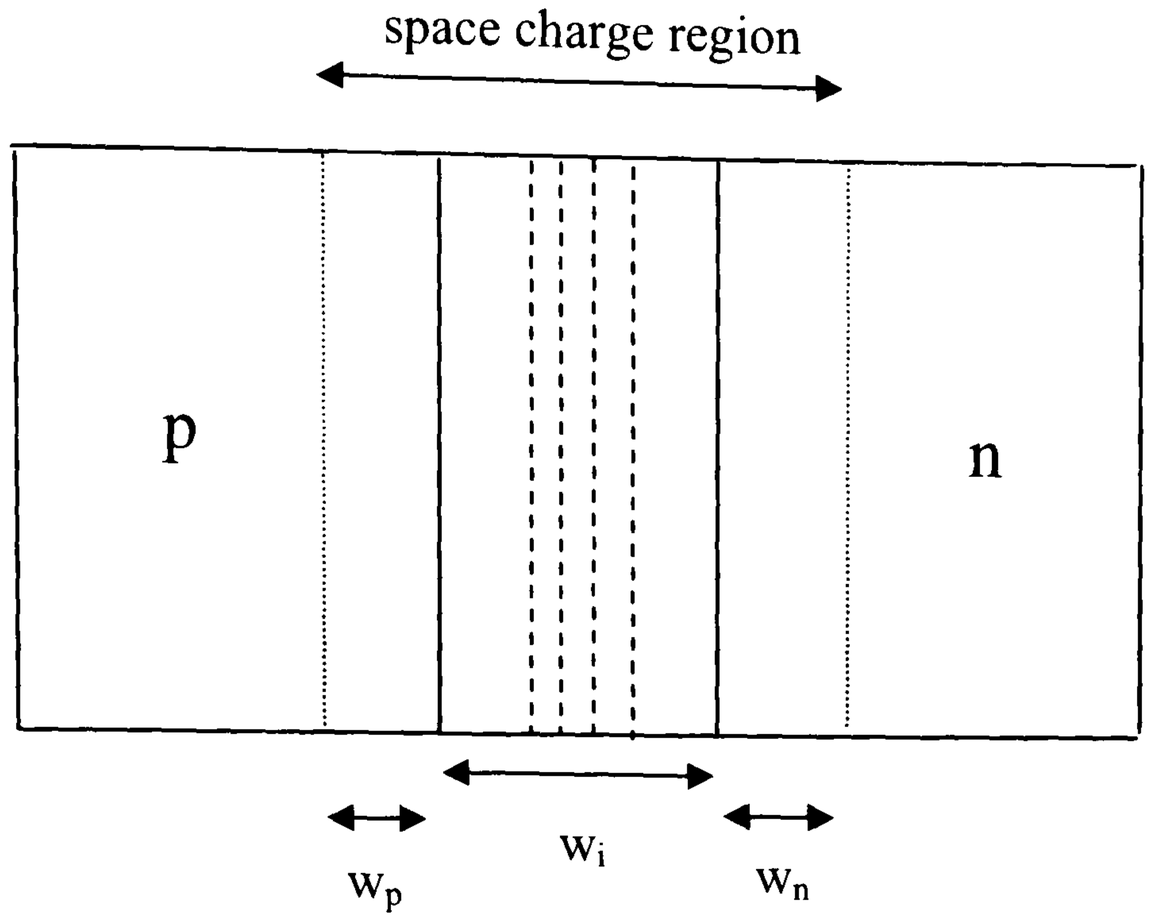

Figure. 5.1. Schematic of a quantum well solar cell showing the width of the intrinsic and space charge regions

The absorption coefficient of the quantum well layer is given by

$$\alpha_w(\lambda) = \sum_{n,m} \alpha_{en \to hhm}(\lambda) + \sum_{n,m} \alpha_{en \to lhm}(\lambda) \tag{5.2}$$

where n and m denote the index of the electron and hole states respectively. A useful quantity to consider is thus the absorption per level per well, which is given by

$$\gamma_{qw} = \alpha_{en \to jhm} L_w \tag{5.3}$$

where j denotes either a heavy or light hole transition [3].

The effects of excitonic absorption must also be included in the model. The exciton binding energy, E_{bind}, may be calculated using [3]

$$E_{bind} = -\frac{R^*}{(n-\nu)^2} \tag{5.4}$$

where ν is a dimensionality parameter that ranges from 0 for a purely three dimensional system to 0.5 for a purely two dimensional system and R^* is the effective Rydberg given by [4]

$$R^* = \frac{m^* R_o}{m_0 \varepsilon_r^2} \qquad (5.5).$$

where m^* is the reduced effective mass of the exciton in the confinement direction, m_0 is the free mass of the electron, ε_r is the permeability of the material and R_o is the Rydberg constant.

Similarly, the exciton oscillator strength, r, may be parameterised as [3]

$$r = \frac{2}{(n-\nu)^3} \qquad (5.6)$$

To account for thermal and phonon broadening, the exciton peaks are modelled as Lorentzian line shapes of width Γ, with typical values of Γ being ~ 10 meV.

The photocurrent created in the n and p layers, J_n and J_p respectively, is then calculated by solving the minority carrier transport equations subject to the appropriate boundary conditions; namely that the excess minority carrier concentration vanishes at the edge of the depleted region and is defined by surface recombination at the front and back surfaces of the cell. The photocurrent generated in the depletion region (J_{dr}) is then combined with the photocurrent arising from the n and p layers to give the total photo-current, J_{pc}

$$J_{pc}(\lambda) = f[J_n(\lambda) + J_p(\lambda) + J_{dr}(\lambda)] \qquad (5.7)$$

where f is the transport parameter which is a measure of the probability of an electron or hole crossing the intrinsic region without recombining. At room temperature f is assumed to be unity, i.e. the thermal energy of the carriers is greater than the well depth so that all carriers escape from the wells and contribute to the photocurrent

Finally, the quantum efficiency at a given wavelength is defined in terms of the incident flux $F(\lambda)$ as

$$QE(\lambda) = \frac{J_{pc}(\lambda)}{qF(\lambda)} \tag{5.8}$$

The FORTRAN program SOL was originally developed by Dr. Jenny Nelson and Dr. Bernd Braun to model AlGaAs/GaAs structures [3] and has since been developed to include InGaAsP/InP [5] and InGaAs/GaAs [6] devices by Dr. James Connolly and Dr. Jenny Barnes. Using SOL it is possible to model the quantum efficiency, dark current characteristics [7], electroluminescence and conversion efficiency of both multi-quantum well and p-i-n devices. This chapter describes refinements made by the author to the quantum efficiency model of the quantum well region of strain-balanced InGaAs/GaAsP devices since October 2003.

5.2 Refinements to the model

5.2.1 Calculation of strained bandgaps

In this section the calculation of the strained band edges is carried out within the framework of a multi-band **k.p** approach (see References 8-11 and Appendices 4 and 5). The application of strain alters the band-gap of the material, as shown in Figure 5.2. The strained conduction – heavy hole band-gap is taken from Reference 9 where it is given by

$$\mathrm{E_{conduction\text{-}hh}} = \mathrm{E_g} + \delta E_h^{gap} + \frac{1}{2}\delta E_s \tag{5.9}$$

and the strained conduction to light hole bandgap by

$$\mathrm{E_{conduction\text{-}lh}} = \mathrm{E_g} + \frac{\delta E_s + \delta E_{so}}{2} + \frac{1}{2}\left[3\delta E_s{}^2 - 2\delta E_s E_{so} + E_{so}{}^2\right]^{\frac{1}{2}} \tag{5.10}$$

where E_g is the unstrained band-gap, δE_h^{gap} is the hydrostatic shift of the conduction to heavy hole band-gap, δE_s the shear shift of the conduction to heavy hole band-gap and E_{so} the difference in energy between the heavy hole and spin-orbit band-edges (see Figure 5.2). The shear component of the strain lifts the degeneracy of the heavy and light hole band-edges. A detailed derivation of the strained band-gaps may be found in Appendix 4.

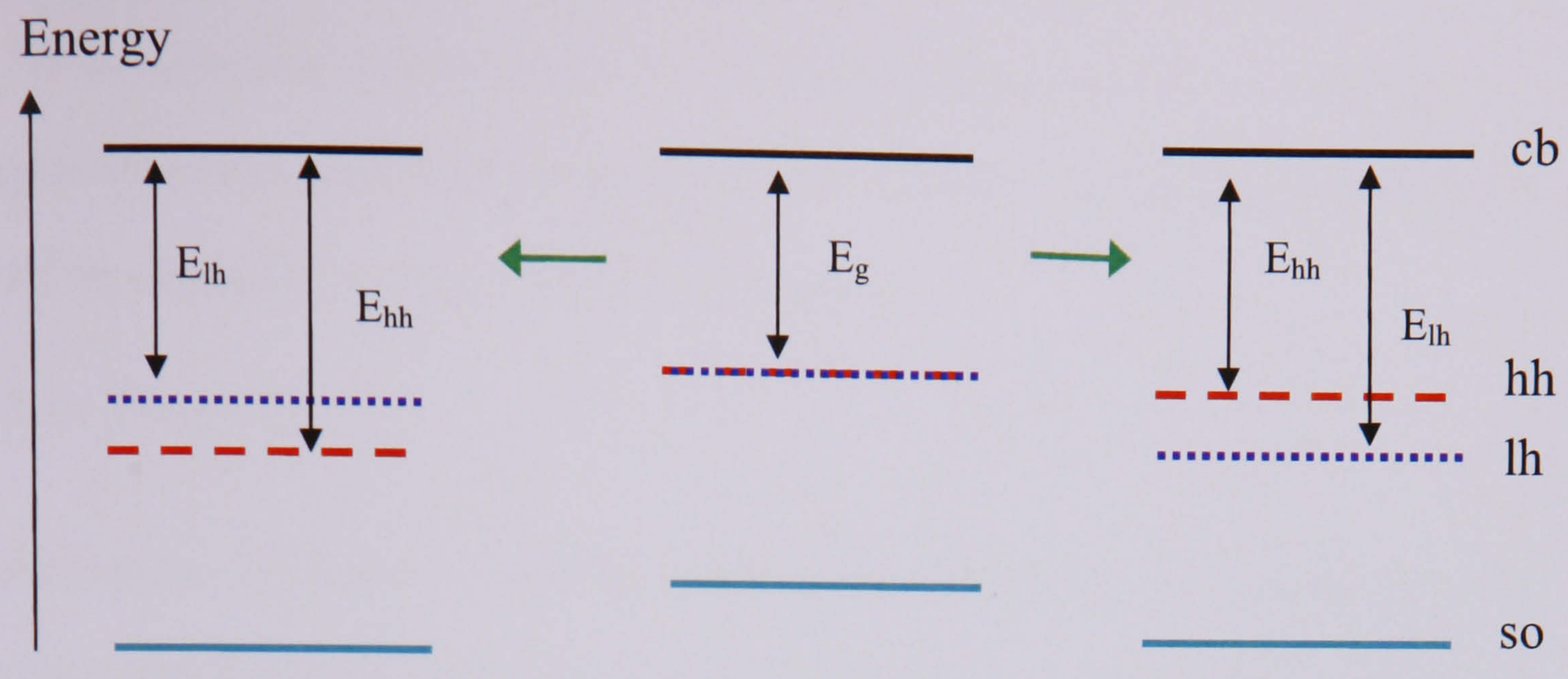

Fig. 5.2. The effect of compressive (r) and tensile (l) strain on the conduction band (cb), heavy hole (hh), light hole (lh) and spin-orbit (so) band-edges. The bulk bandgap, E_g, the conduction to heavy hole band-gap, E_{hh}, and the conduction to light hole band-gap E_{lh}, are also shown. The position of both valence bands are depicted relative to the conduction band.

For compressively strained material, the heavy hole band-edge is higher in energy than the light hole band-edge, with the converse applying in material under tensile strain [8]. A bandedge profile of a typical InGaAs/GaAsP SB-MQW is shown in Figure 5.3

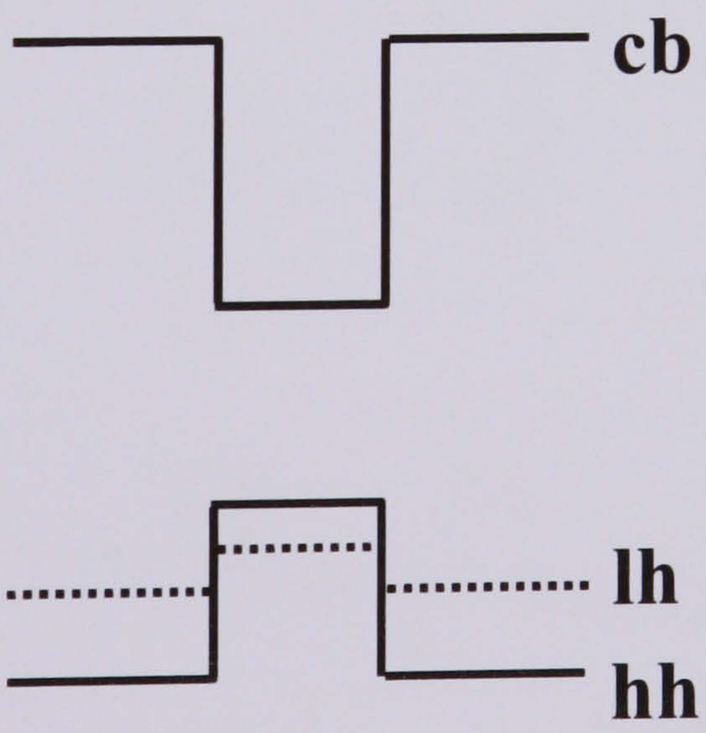

Fig. 5.3. Band-edge profile of a typical InGaAs/GaAsP quantum well and barrier

The value of the conduction to heavy hole strained band-gap of a $In_{0.1}GaAs$ well is 1.319 eV, compared to a value of 1.278 eV obtained when the effects of strain are neglected, emphasizing the importance of proper calculation of the strained band-gaps.

5.2.2 Determination of the conduction band offset

5.2.2.1 Theory

As mentioned in Chapter 1, a critical parameter in obtaining the confined energy levels within a finite quantum well is the well depth. However, an essential parameter in obtaining the well depth, the conduction band offset or Q_c, is not well known for the InGaAs/GaAsP material system. Q_c is defined as the extent to which the difference in energy between the well and barrier material is apportioned between the conduction and valence bands (see Figure 5.4). Mathematically

$$Q_c = \frac{W_e}{E_{gb} - E_{gw}} \tag{5.11}$$

where W_e is the well depth, E_{gb} the band-gap of the barrier material and E_{gw} the band-gap of the well material

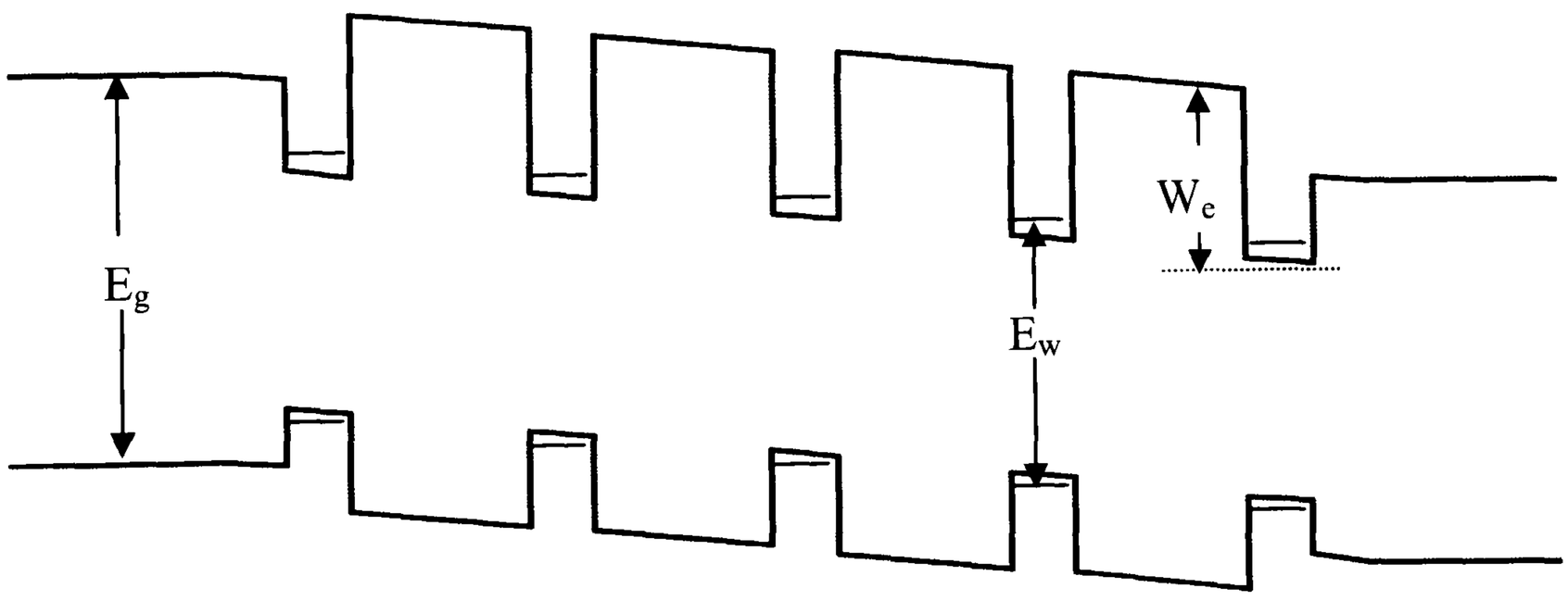

Figure 5.4. The conduction band offset

One parameter that is very sensitive to the value of the valence band offset is the splitting between the heavy and light hole exciton peaks, which also depends on the indium content of the material (and hence the strain). Thus, Q_c is a function of the light hole – heavy hole peak splitting Δ(hh-lh). We note in passing that if the value of Q_c becomes large enough the light hole will become unbound (see Figure 5.5).

In previous work the value of Q_c has been assumed to be the same as that of bulk InGaAs, namely 0.67. Using this value one would expect the light hole to be unbound, as was observed for strained InGaAs wells in GaAs [14]. However, a light hole state is visible in the experimentally determined quantum efficiencies of almost all InGaAs/GaAsP values, suggesting that the value of Q_c needs to be refined.

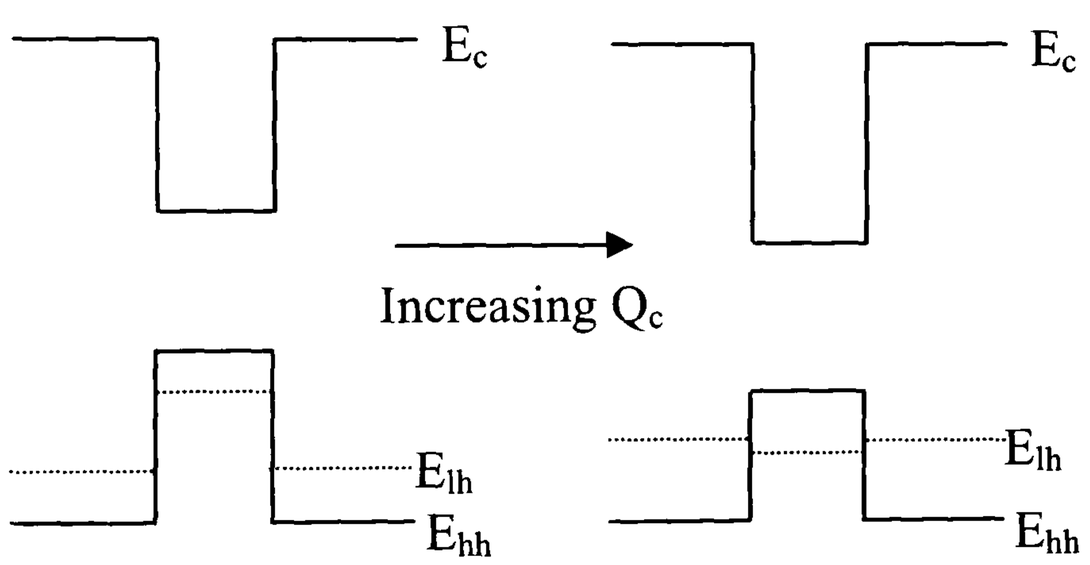

Figure 5.5. The effect of strain on the heavy and light hole band edges in a strain-balanced system consisting of compressively strained wells and tensile strained barriers.

5.2.2.2 Experimental work

The photocurrents of three SB-MQW samples were measured using a tungsten filament lamp coupled to a 30cm Bentham monochromator. The photocurrent was then determined using a lock-in amplifier and voltage stabilizing electronics as described in Section 2.3.2. A closed-cycle cryostat was used to maintain the sample at (10±1) K. For each device, spectra were recorded at a number of different voltages to allow

identification of forbidden transitions to aid the identification of each observed exciton peak. The composition of each sample is shown in Table 5.1.

Sample Name	Well width (nm)	Barrier width (nm)	Well indium fraction	No. of wells
Qt1858D	8.3	16.4	0.11	65
Qt1838R	8.3	16.4	0.125	65
Qt1747C	10.0	29.3	0.185	30

Table 5.1. Compositions of samples studied. The Indium content of all samples was determined from fits to room temperature quantum efficiencies

5.2.2.3 Results

A typical photocurrent spectrum is displayed in Figure 5.6. Two exciton peaks (at 865nm and 835nm) arising from allowed transitions and one from a forbidden transition (seen at 845nm) can be observed in the spectra. The forbidden peak is absent at forward biases close to flat band but becomes noticeable as the field increases in reverse bias.

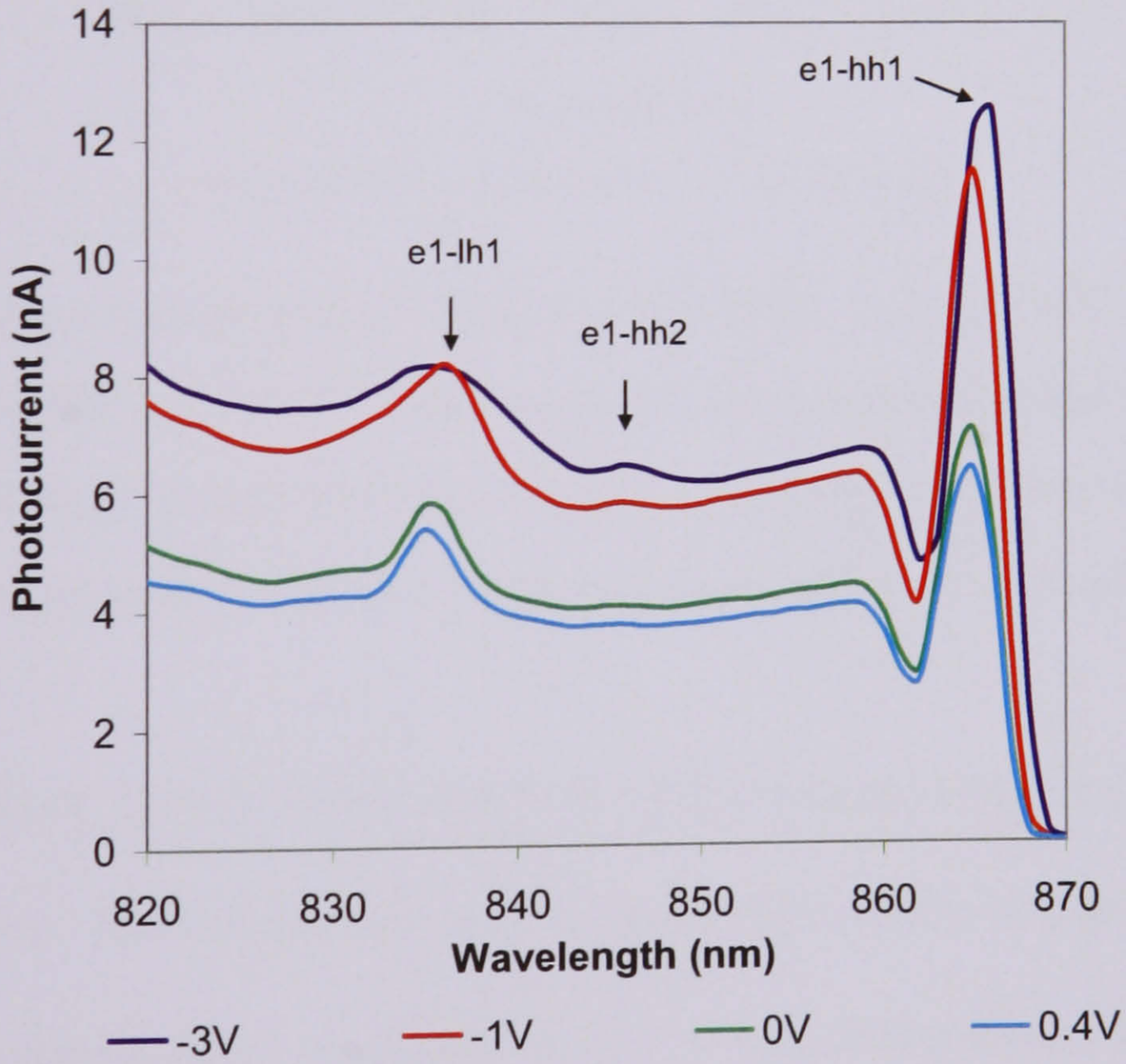

Figure 5.6. Low temperature photocurrent of Qt1858D recorded at 10K

The photocurrent spectra of Qt1858D, Qt1838R and Qt1747C measured at 1.1V forward bias are displayed in Figure 5.7. As expected the e1-hh1 exciton peak shifts to

longer wavelength as the indium content of the wells, and therefore strain, is increased. Also, the splitting between the e1-hh1 peak and the e1-lh1 peak increases with increasing indium fraction.

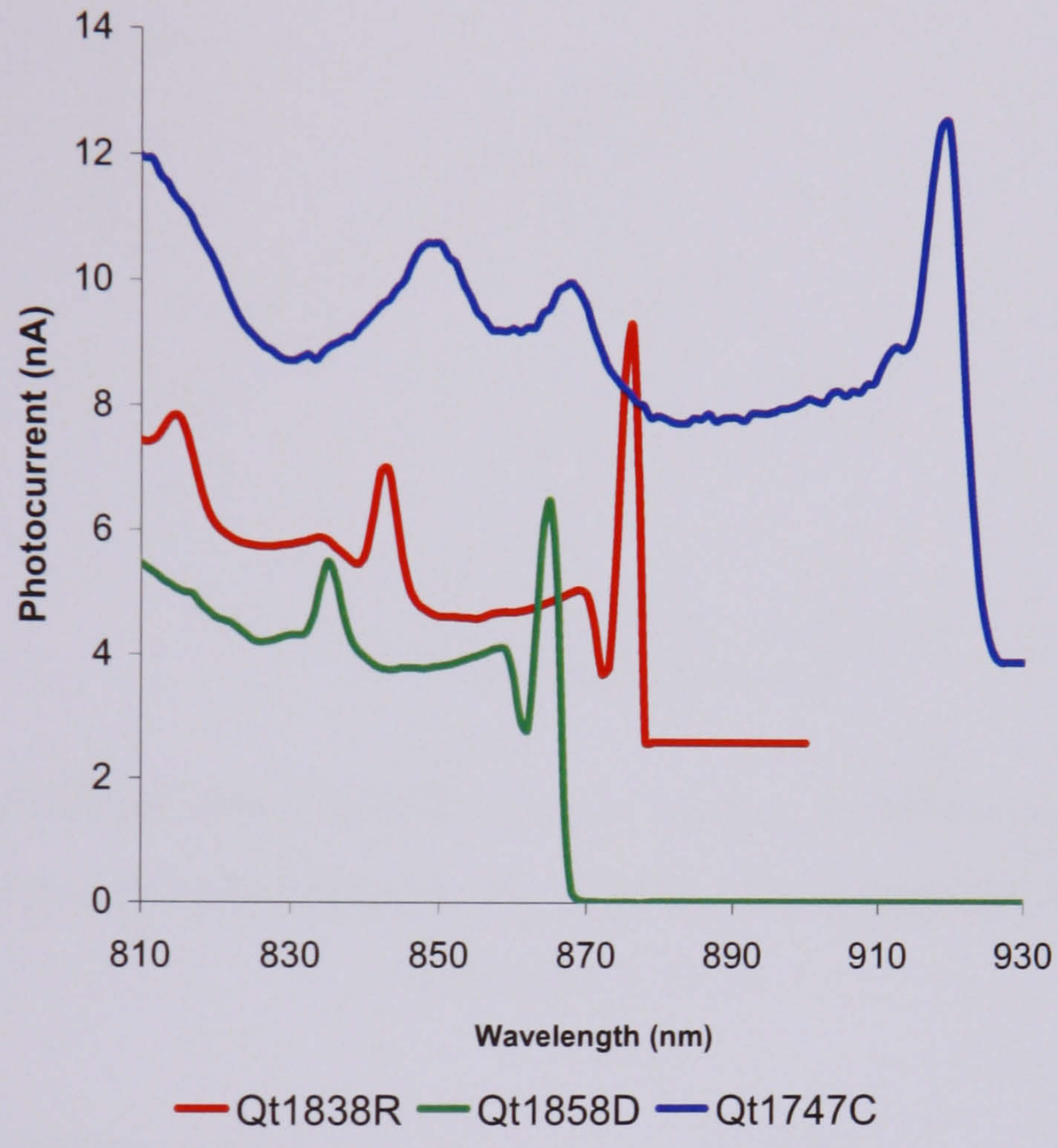

Figure 5.7: Flat band spectra of Qt1858D, Qt1838R and Qt1747C at 10 K, with the spectra of Qt1838R and Qt1747C vertically and horizontally offset for clarity. The e1-hh1 exciton peak is seen to shift to longer wavelengths and the e1-hh1 to e1-lh1 splitting is seen to increase with increasing indium in the well material.

Measured values of Δ(hh-lh) observed in the three samples were obtained from the photocurrent scan. Theoretical values of Δ(hh-lh) were then calculated as a function of indium fraction for Q_c values ranging from 0.6 to 0.4, as shown in Figure 5.8. The measured values of Δ(hh-lh) are also displayed. By comparison between the calculated and measured values of Δ(hh-lh) a value of $Q_c = 0.53 \pm 0.05$ was obtained c.f. the previously assumed value of 0.67.

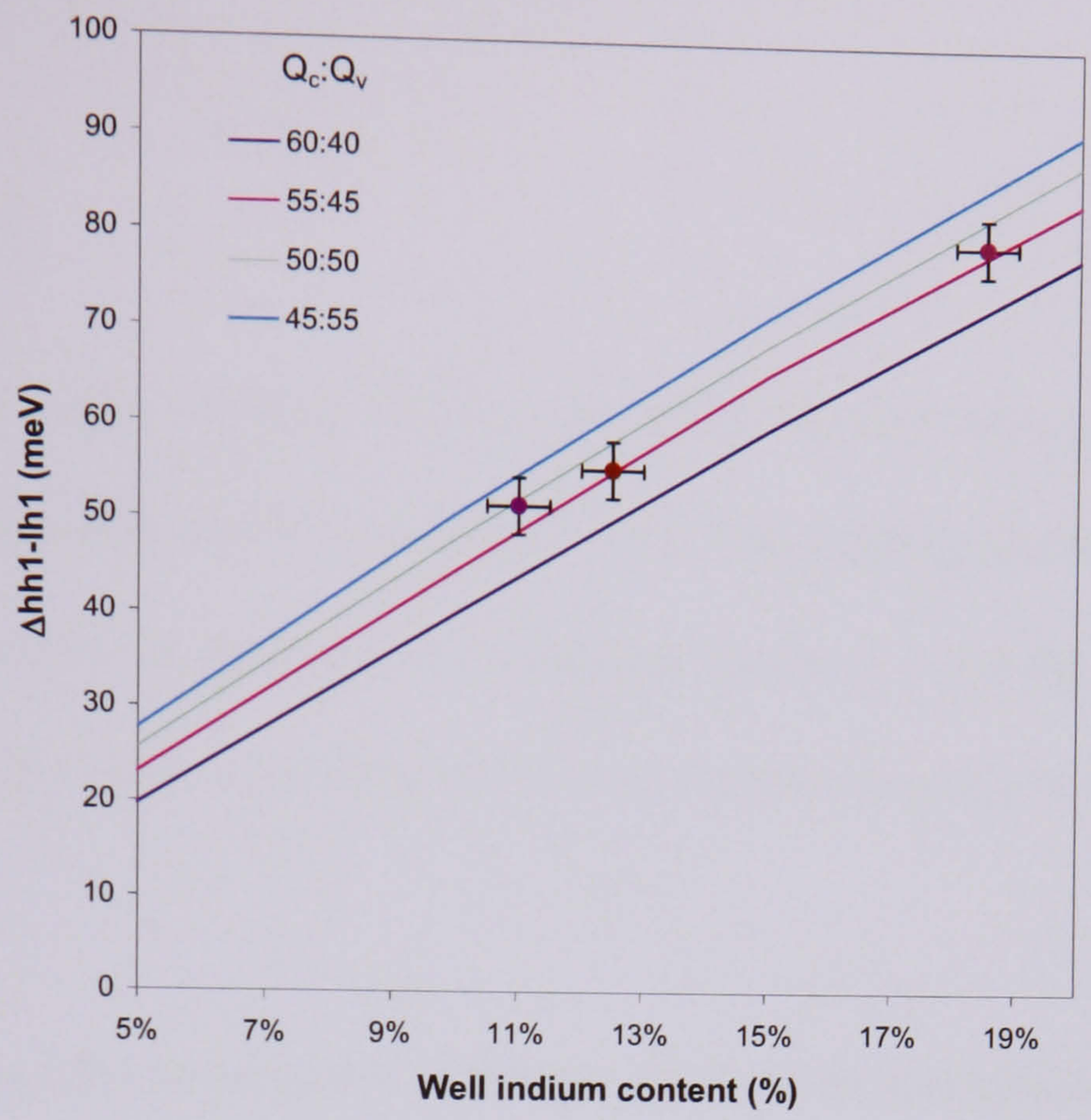

Figure 5.8: Calculated values of Δ(hh-lh) as a function of indium fraction for a series of values of Q_c. The solid dots represent the experimentally determined values of Δ(hh-lh) measured at 10 K.

5.2.2.4 Consideration of errors

In using the splitting between the exciton peaks as a measure of the difference in energy between the heavy and light hole confined states we have assumed that the exciton binding energies for the each respective transition are the same in each sample. This is not seen as a significant source of error due to the small magnitude of the exciton binding energies (~ 8 meV). Additionally, there is uncertainty in the well width, as only the well/barrier period is directly measured using X-ray diffraction. Again this is not seen as a significant source of error as a 20Å change in well width leads to a change of only 0.5meV in Δ(hh-lh). The Bentham monochromator used in the experimental work has a resolution of 1nm, corresponding to an energy of ~ 3 meV. The largest source of error is taken to be the uncertainty in the indium content of the sample with a 1%

absolute change in indium fraction producing ~10% change in Δ(hh-lh). The overall error in the value of Q_c is thus taken to be 10%.

5.2.2.5 Conclusions

The results suggest that $Q_c = 0.53 \pm 0.05$ in this material system, significantly different to the previously used value of 0.67. This is in broad agreement with previous work, which suggested the light hole becomes unbound at $Q_c \approx 0.6$ for InGaAs/GaAs [9] and that the value of Q_c is between 0.57 and 0.7 for this material system [15-19]

5.2.3 Calculation of the absorption of the quantum wells and effective mass study

5.2.3.1 Theory

In the original model the absorption per level per well was assumed to be the value of 1%, which applies to AlGaAs/GaAs wells, and then adjusted as a free parameter to fit the experimental data.

The expression absorption coefficient used in this work is [8]

$$\alpha_{e1-hh1} = \frac{N\pi e^2 m_{red,ll} E_p \left|\langle F_{hh} \mid F_e \rangle\right|^2}{\hbar^2 \omega n_r L_w c m_0} \theta[\hbar w - E_e - E_{hh} - E_g] \qquad (5.12)$$

for e1-hh1 transitions and

$$\alpha_{e1-lh1} = \frac{N\pi e^2 m_{red,ll} E_p \left|\langle F_{lh} \mid F_e \rangle\right|^2}{3\hbar^2 \omega n_r L_w c m_0} \theta[\hbar w - E_e - E_{hh} - E_g] \qquad (5.13)$$

for e1-lh1 transitions with normal incidence being assumed. E_p is the Kane matrix element which is proportional to $\langle U_c | \boldsymbol{p} | U_v \rangle$ (see Equation 1.30), N is the number of

quantum wells, n_r the refractive index of the well material which is approximately equal to $\sqrt{\varepsilon_r}$ where ε_r is the relative permittivity of the well material, L_w is the well width and $m_{red,//}$ is the reduced in-plane effective mass (see Section 1.5.12) and θ denotes the step function [8].

As can be seen from Equations 5.12 and 5.13, the reduced in-plane effective mass, $m_{red,//}$ is a critical parameter in calculating the absorption. Existing approaches used in SOL considered the effective masses in the growth and in-plane directions to be equal. While this is a valid approximation for an unstrained system in which the E-k dispersion is isotropic along the confined and in-plane directions (the reader is reminded that the effective mass is inversely proportional to the curvature of the E-k curve), once strain is applied the dispersion is significantly altered. Although the conduction band remains relatively isotropic the heavy and light hole bands become significantly anisotropic, with the heavy hole band displaying light hole characteristics (i.e. a lighter mass) in the in-plane direction and the light hole band displaying heavy hole characteristics [20] (see Figure 5.9).

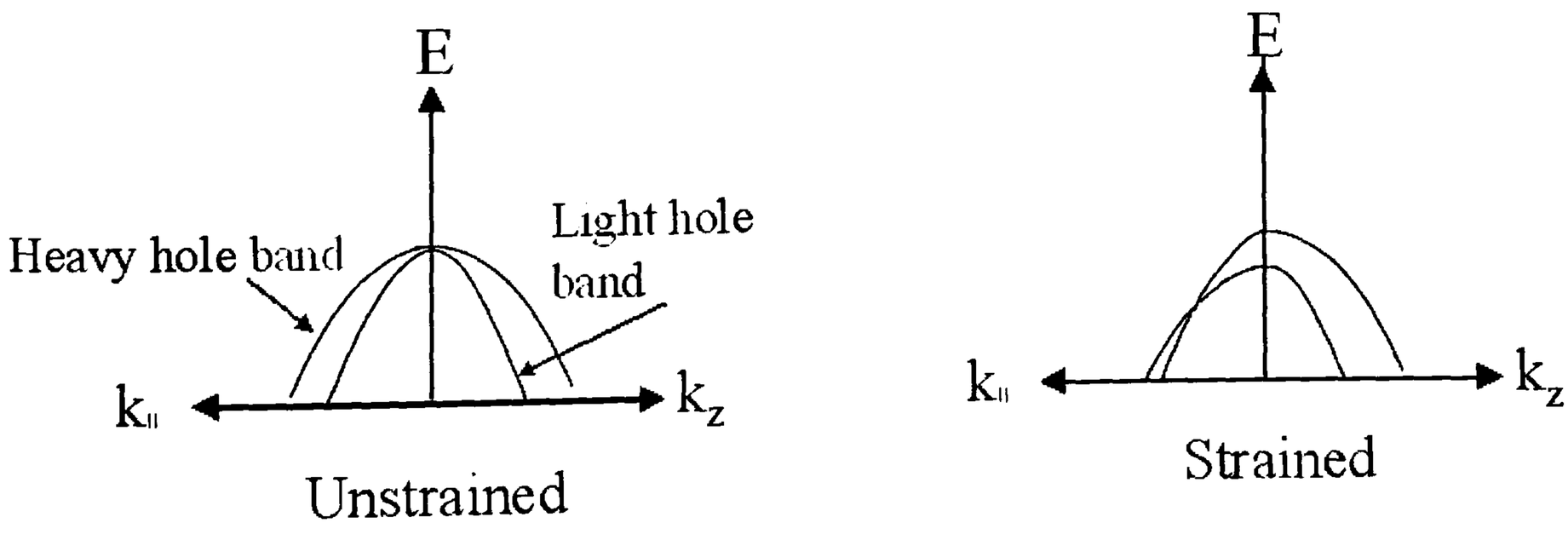

Figure 5.9: The E-k dispersion of the heavy hole and light hole bands for an unstrained and strained bulk system.

Due to the anisotropy of the valence band the in-plane and growth direction hole masses can no longer be assumed to be the same. One of the key results of the work presented in this section is to obtain and parameterize the hole in-plane effective masses and incorporate them into the SOL framework.

5.2.3.2 Overview of the ***k.p*** *model*

In this work accurate values for the effective masses of the first confined heavy and light hole states are sought by examining the E-k dispersions generated using a multiband **k.p** model (an overview of the basic principles of **k.p** theory may be found in Appendix 5). The model includes the interaction between the heavy and light hole valence bands but the effect of the spin orbit band, ~ 300 meV away, is neglected when calculating the dispersion but included when calculating the confined levels. The interaction between the sub-band scales inversely with distance between sub-bands.

It is interesting to compare the effective masses obtained from the calculated dispersions to those obtained using the expression [21]

$$m^*_{i,\parallel} = \frac{4m^*_{i,z}m^*_{j,z}}{m^*_{j,z}+3m^*_{i,z}} \quad . \tag{5.14}$$

Here $m^*_{i,\parallel}$ is the hole in-plane effective mass and $m^*_{i,z}$ and $m^*_{j,z}$ are the heavy and light hole masses in the confinement direction which are determined using linearly interpolated Luttinger parameters, γ_1 and γ_2 as in Reference 22 by:

$$m^*_{hh,z} = \frac{1}{\gamma_1 - 2\gamma_2} \tag{5.15}$$

and

$$m^*_{lh,z} = \frac{1}{\gamma_1 + 2\gamma_2} \tag{5.16}$$

We denote effective masses determined in this way as interpolated masses and will compare them with the values extracted by our preferred procedure in Section 5.2.3.4

5.2.3.3 Extraction of valence band in-plane effective masses

The E-k dispersions for each confined state of quantum well structures with a range of indium contents and well widths were calculated (using a MATLAB program written by Dr. P.N. Stavrinou) along the <10> and <11> directions (defined in Figure 5.10). Due to the symmetry of the zinc-blende crystal structure the <10>, <01>, $<\bar{1}0>$ and $<0\bar{1}>$ directions and the <11>, $<1\,\bar{1}>$, $<\bar{1}\,1>$ and $<\bar{1}\,\bar{1}>$ directions may be considered to be equivalent [23], as illustrated in Figure 5.11.

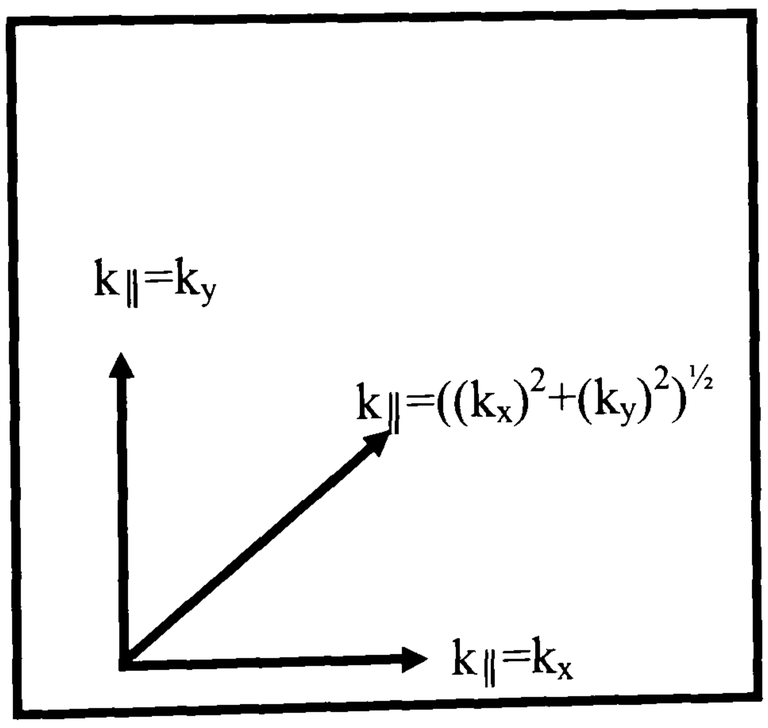

Figure 5.10. Schematic of the in-plane wave-vectors

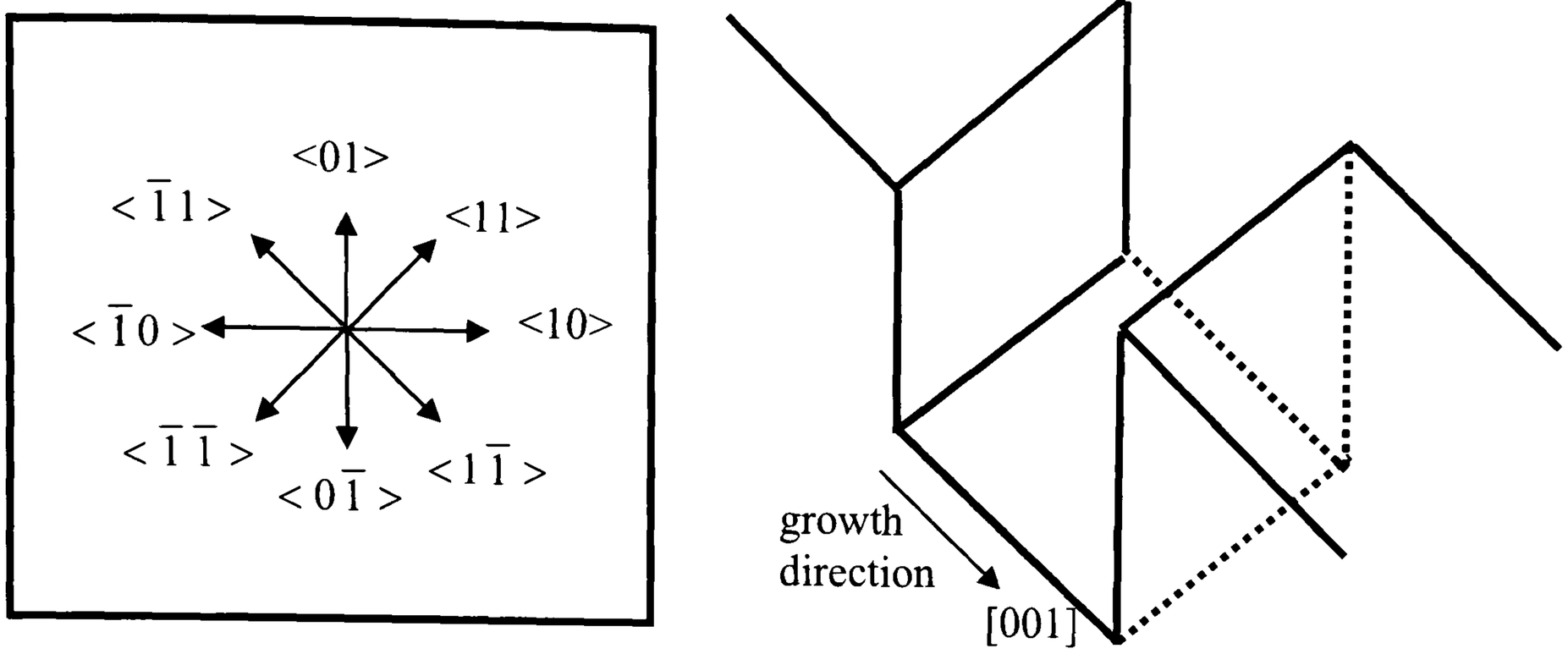

Figure 5.11. Schematic of the in-plane directions and the growth direction

A value of the conduction band offset of 0.55 and a barrier composition of $GaAs_{0.81}P_{0.09}$ were assumed. The identification of the different confined states is non-trivial. Clearly, due to the fact the well material is under compressive strain, the first heavy hole sub-band is highest in energy. Also, the light hole sub-band must be removed from the heavy hole band-edge by an amount of energy greater than the splitting between the heavy and light hole band edges. However, obtaining the nature of the other sub-bands is less straightforward and therefore these states were then identified using a separate "particle in a box" MATLAB program, also written by Dr P.N. Stavrinou. A number of calculated dispersions are shown in Figure 5.12

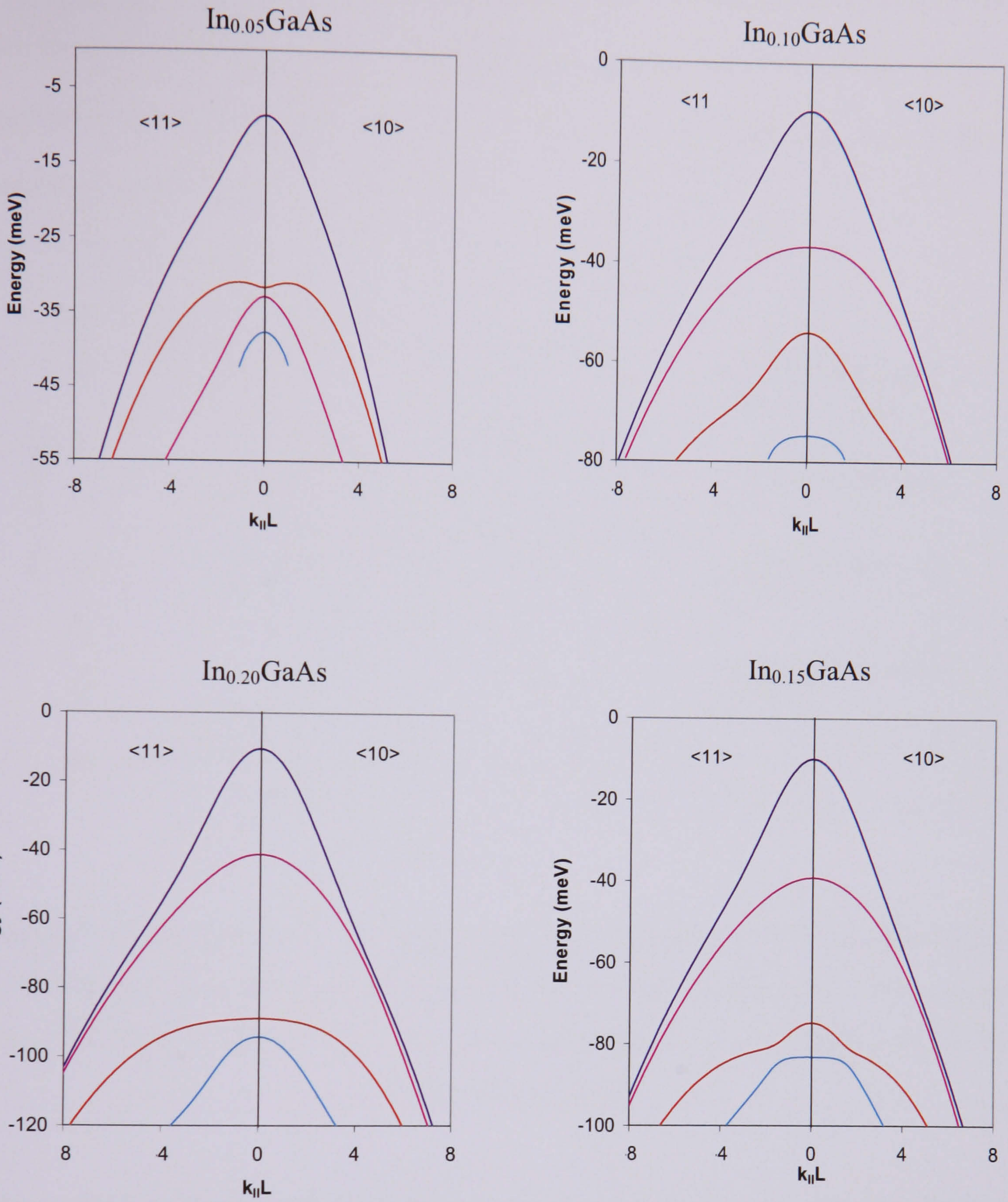

Figure 5.12. In-plane valence band dispersions calculated using a multi-band **k.p** program for an 80 Å compressively strained Indium In_xGaAs quantum well enclosed by a 9% Phosphorous tensile strained $GaAsP_y$ barrier for indium fraction of 0.05, 0.1, 0.15 and 0.2. Sub-bands shown are first heavy hole sub-band (dark blue), first light hole sub-band (red), second heavy hole sub-band (purple) and third heavy hole sub-band (light blue). The strained heavy hole band-edge is taken as the zero point of energy.

As can be seen from Figure 5.13, the curvature of the calculated dispersion, and hence the value of the in-plane effective mass, changes over the energy range spanned by the quantum well. Thus for an accurate calculation of the in-plane effective mass, the mass should be modelled as a function of energy.

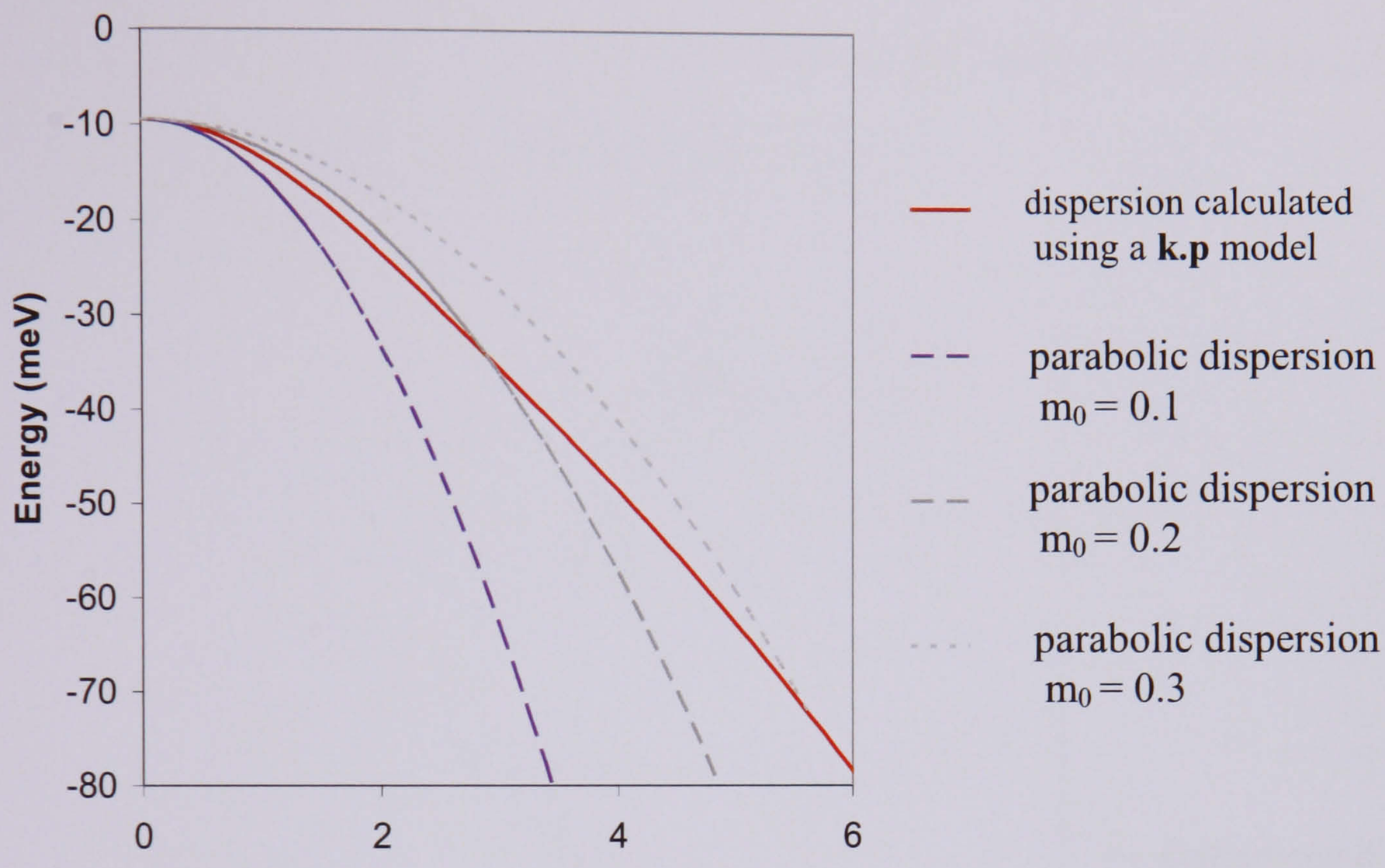

Figure 5.13. E-k dispersion calculated using a multi-band **k.p** model for the first heavy hole sub-band of an 80Å $In_{0.1}GaAs$ quantum well enclosed in a $GaAsP_{0.09}$ barrier along the <10> direction and parabolic dispersions using values of 0.1, 0.2 and 0.3 m_0 for the in-plane effective mass.

Due to the fact that the in-plane effective mass is needed as an input parameter for SOL which is a highly complex modelling program, a single value for the in-plane effective mass is more conducive to computational efficiency i.e. the SOL framework. It must also be remembered that the quantity ultimately needed to calculate absorption is the density of states, which is proportional to the area enclosed by the dispersion E-k curve. An energy independent value of the in-plane effective mass was therefore extracted by calculating the area enclosed by the **k.p** dispersion curve, and hence the density of states associated with the sub-band, using the trapezium rule. A parabolic dispersion was then

generated and the effective mass used to generate the parabola was adjusted until the area under the parabolic curve equalled that enclosed by the **k.p** dispersion (see Figure 5.14). Referring back to Figure 5.12, the dispersion and hence the effective mass along two different directions must be considered. This was achieved by extracted values for the in-plane effective mass along the two in-plane directions ($m_{<01>}$ and $m_{<11>}$) and then finding the average in-plane effective mass, m_{av} via

$$m_{av} = \frac{1}{2}\left(m_{<01>} + m_{<11>}\right) \tag{5.17}$$

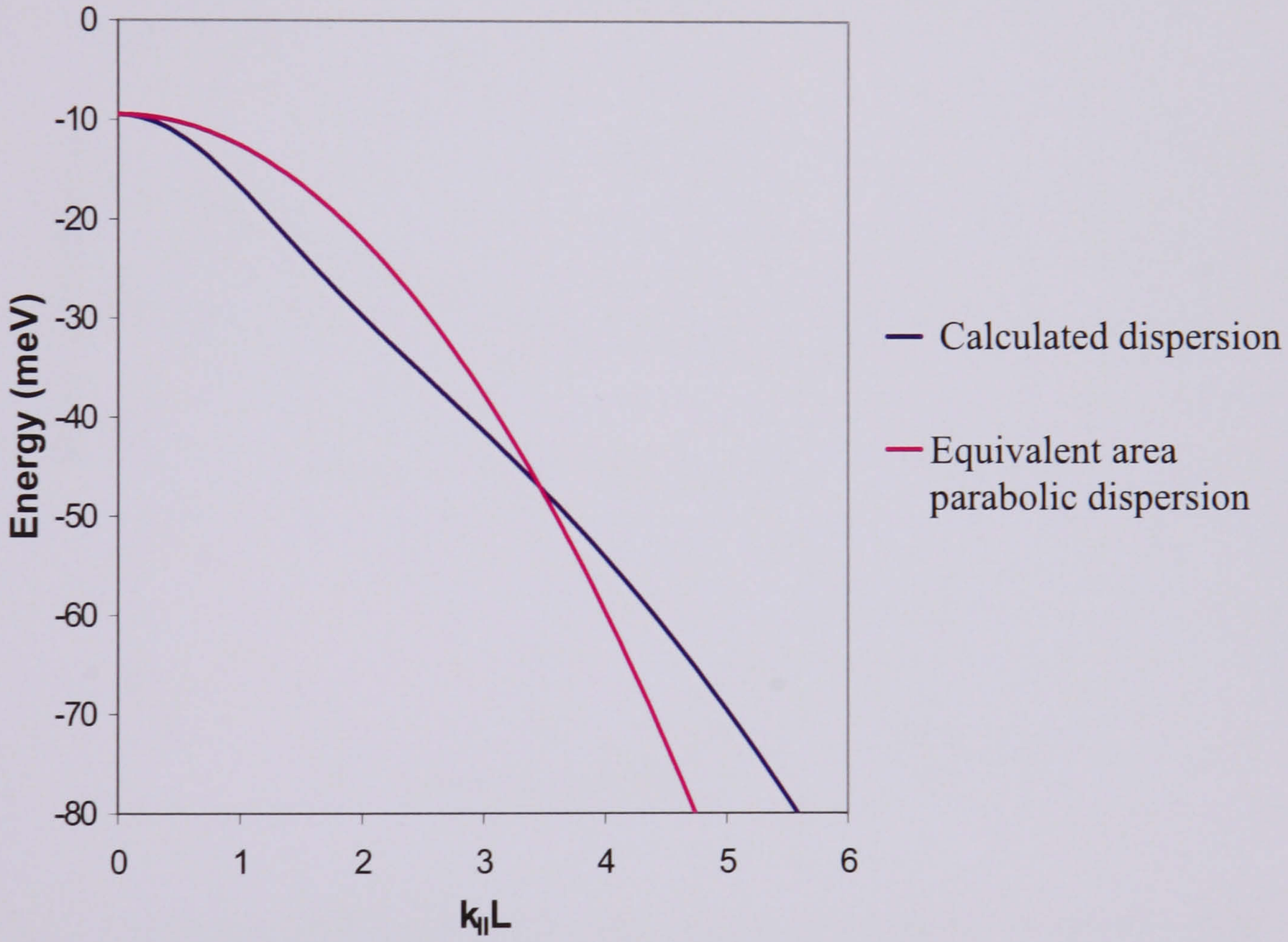

Figure 5.14 An equivalent area parabolic fit to the calculated **k.p** dispersion for an $In_{0.1}GaAs$ quantum well. The constraint used for the fit is that the area enclosed by the two curves, and hence the density of states associated with the two dispersions, should be equal.

5.2.3.4 Results

First heavy hole state

The extracted in-plane effective masses obtained from a parabola of equivalent area being fitted to a dispersion calculated using the multiband **k.p** program, together with interpolated in-plane effective masses obtained using Equation 5.14 for the first heavy hole state are displayed in Figure 5.15.

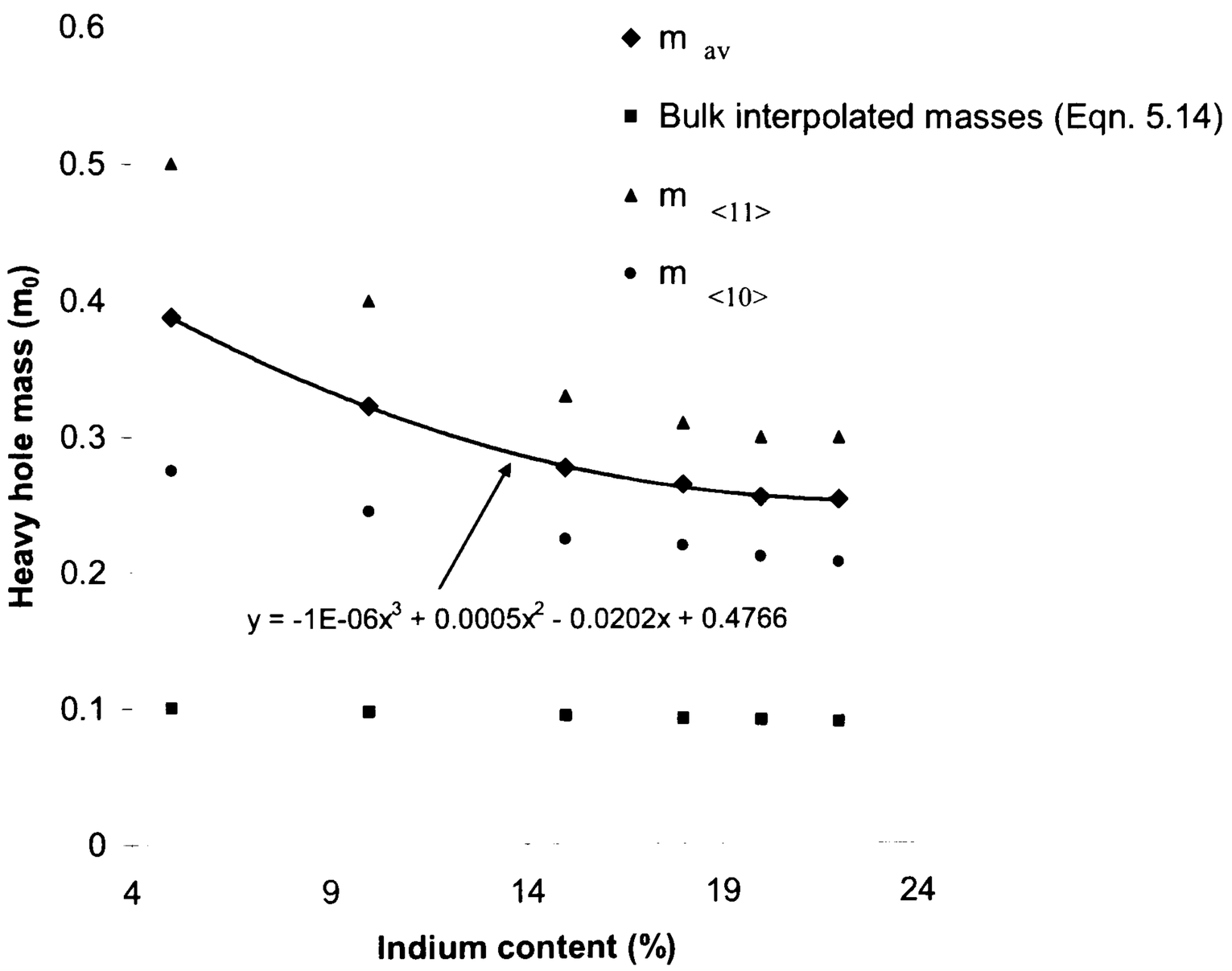

Figure 5.15: Interpolated and extracted in-plane masses as a function of indium content for the first heavy hole sub-band for an 80Å In_xGaAs quantum well enclosed by a $GaAsP_{0.09}$ barrier.

As can be seen in Figure 5.15 the extracted in-plane masses obtained from fits to the calculated dispersions are significantly higher than the interpolated masses found using the method discussed in Section 5.2.3.2. The average extracted masses are up to four times the magnitude of the interpolated values, corresponding to around a 40% difference in $m_{red,//}$ and hence absorption. Also, the relationship between effective mass

and indium content for the extracted masses is not the same as the linear relationship observed for the interpolated masses. Additionally, the extracted masses are observed to be significantly different along the <10> and <11> directions, with the in-plane effective masses being up to 66% higher along the <11> direction. This is to be expected as the in-plane wave-vector is a factor of $\sqrt{2}$ longer along the <11> direction, thus increasing the density of states associated with the E-k curve. The average extracted in-plane mass can be modelled as a polynomial function, as displayed in Figure 5.15.

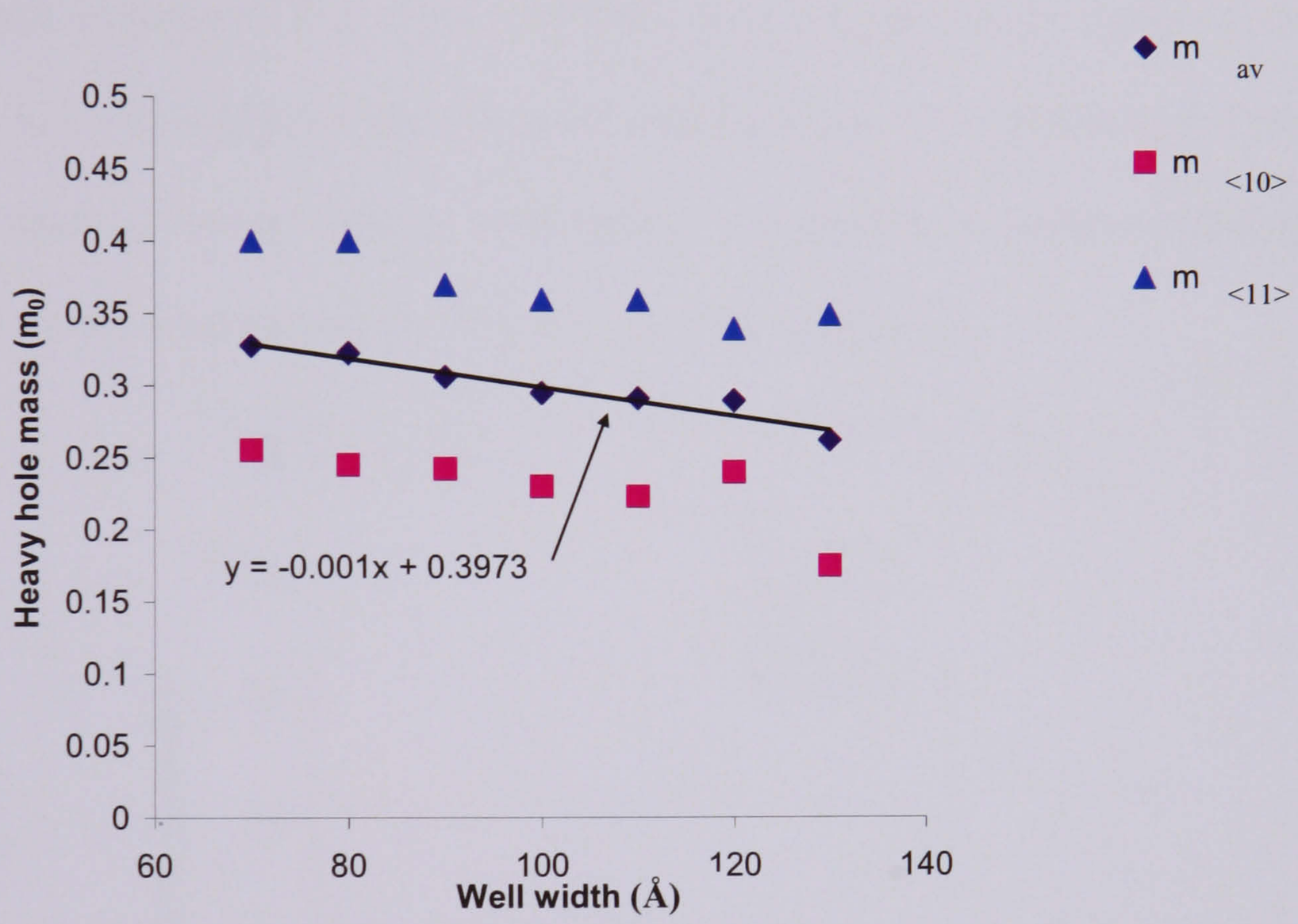

Figure 5.16: Relationship between numerically extracted heavy hole mass and well width for the first light hole sub-band of an $In_{0.1}GaAs$ quantum well enclosed by a $GaAsP_{0.09}$ barrier.

The relationship between extracted heavy hole mass and well width is displayed in Figure 5.16. The extracted mass is seen to vary with well width, again displaying different behaviour to the interpolated effective masses which are independent of well width. The variation of extracted effective mass with well width is caused by the increase in the distance between the sub-band levels with increasing well width, which reduces the interaction between the sub-bands. However the change in hole effective

mass with well width is relatively small (~10% change over a well width range of 30nm) and thus may be neglected to a first approximation, given that the total range of well widths studied is from 70 nm to 130 nm.

First light hole state

For certain values of well indium content (5% indium and 18% indium) the first light hole sub-band is brought into very close proximity to the second and third heavy hole sub-bands respectively (see Table 5.2). This causes the sub-band to distort, as shown in Figure 5.17, (c.f. the dispersion obtained when the heavy and light hole sub-band are further apart, as shown in Figure 5.18) making it impossible to extract a meaningful effective mass from a parabolic fit to the calculated dispersion.

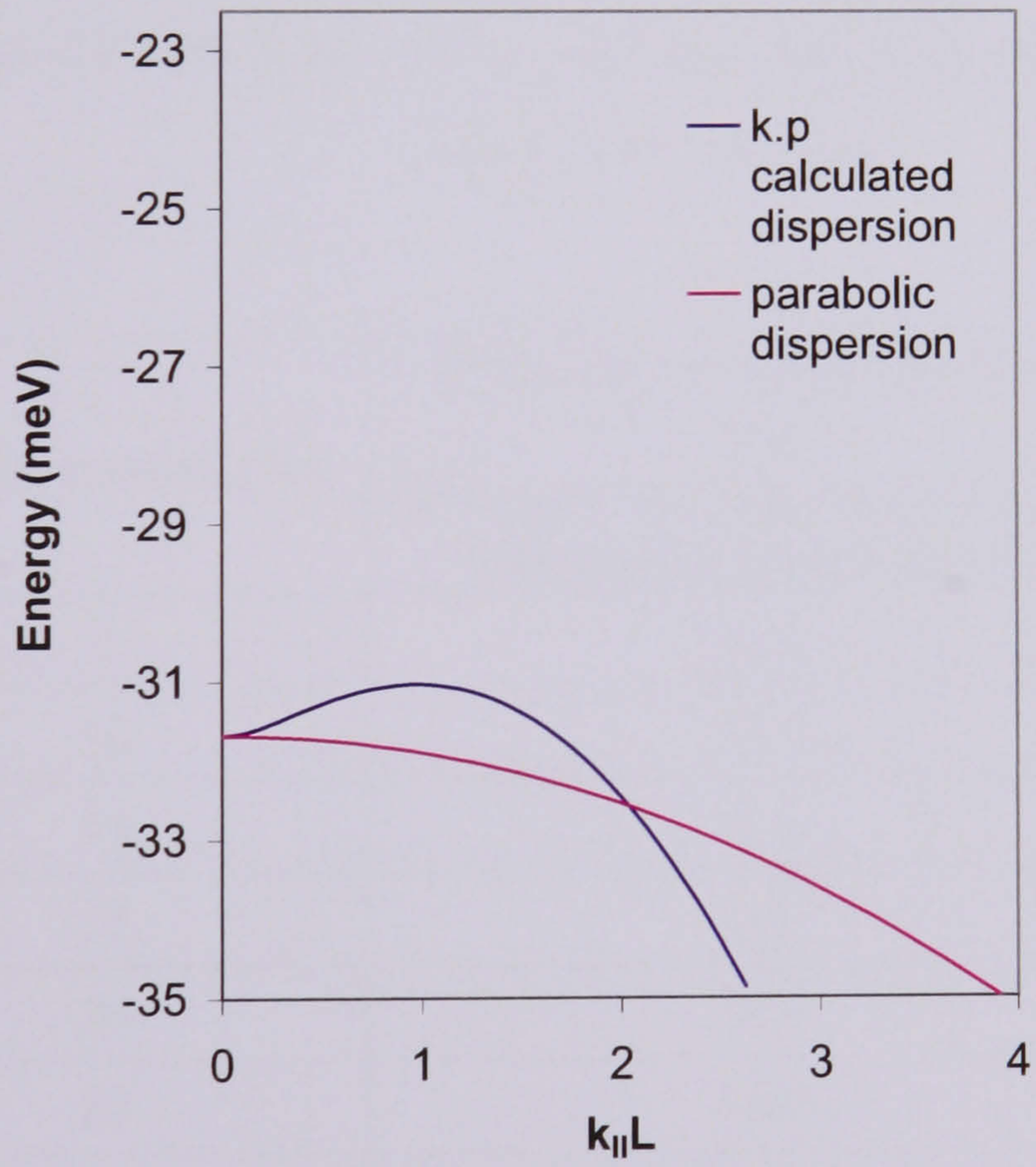

Figure 5.17: Calculated and parabolic dispersions for the first light hole state along the <10> direction for a 80 Å $In_{0.05}GaAs$ quantum well enclosed by a $GaAsP_{0.09}$ barrier. Note that the well has become an indirect structure. The zero of energy is the strained heavy hole band-edge.

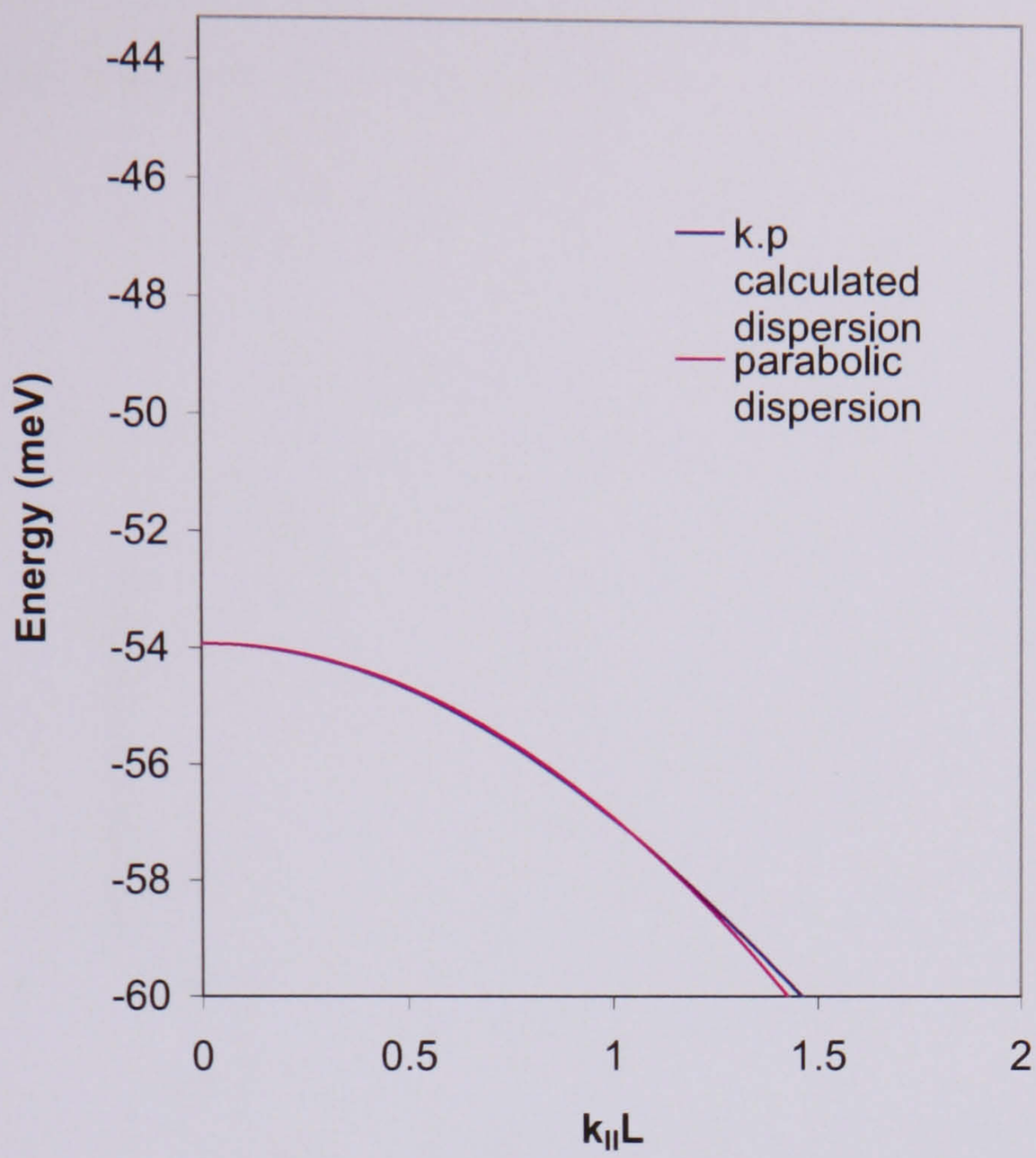

Figure 5.18: Calculated and parabolic dispersions for the first light hole state along the <10> direction for a 80 Å $In_{0.1}GaAs$ quantum well. The zero of energy is the strained heavy hole bandedge.

Indium content (%)	Difference in energy between the first light hole sub-band and next nearest neighbour (meV)	Well behaved extracted effective mass?
5	1.2	No
10	18.7	Yes
15	8.4	Yes
18	0.8	No
20	20.1	Yes
22	10.7	Yes
24	16.0	Yes

Table 5.2: Difference in energy between the first light hole sub-band and the next nearest band as a function of well indium content for an 80 Å In_xGaAs quantum well enclosed by a $GaAsP_{0.09}$ barrier.

The relationship between the extracted and interpolated in-plane light hole masses and indium content is displayed in Figure 5.19

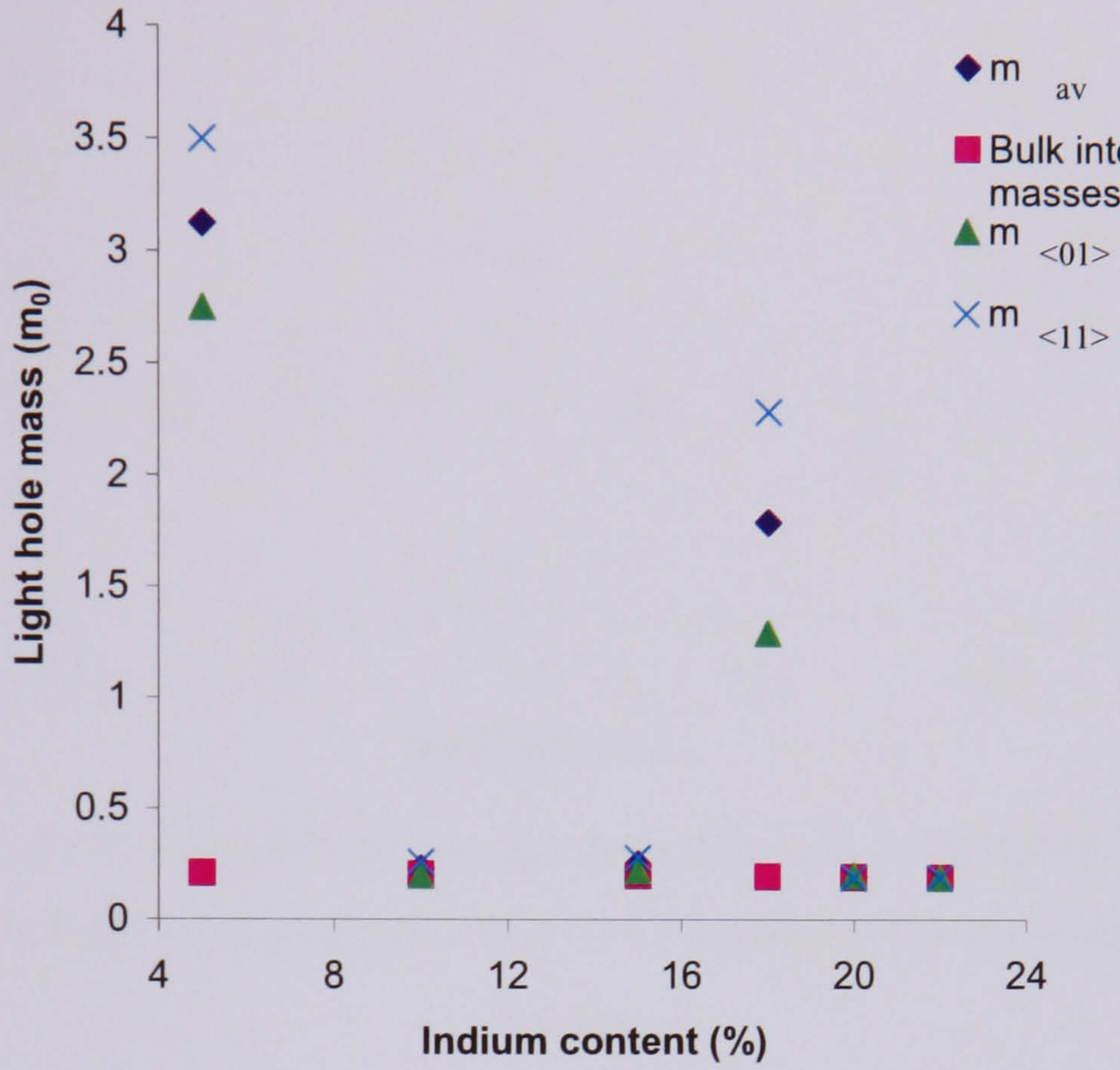

Figure 5.19: Relationship between extracted and interpolated in-plane effective masses as a function of indium content for the first confined light hole state for an 80 Å In_xGaAs quantum well enclosed by a $GaAsP_{0.09}$ barrier.

The dependence on indium content of the extracted in-plane mass is not monotonic, with the extracted mass being approximately ten times the interpolated mass for a 5% indium quantum well and an 18% indium quantum well (i.e. where the light hole sub-band displays non-parabolic behaviour) and being almost equal to the linearly interpolated mass for all other indium contents where parabolic behaviour is displayed by the light hole sub-band.

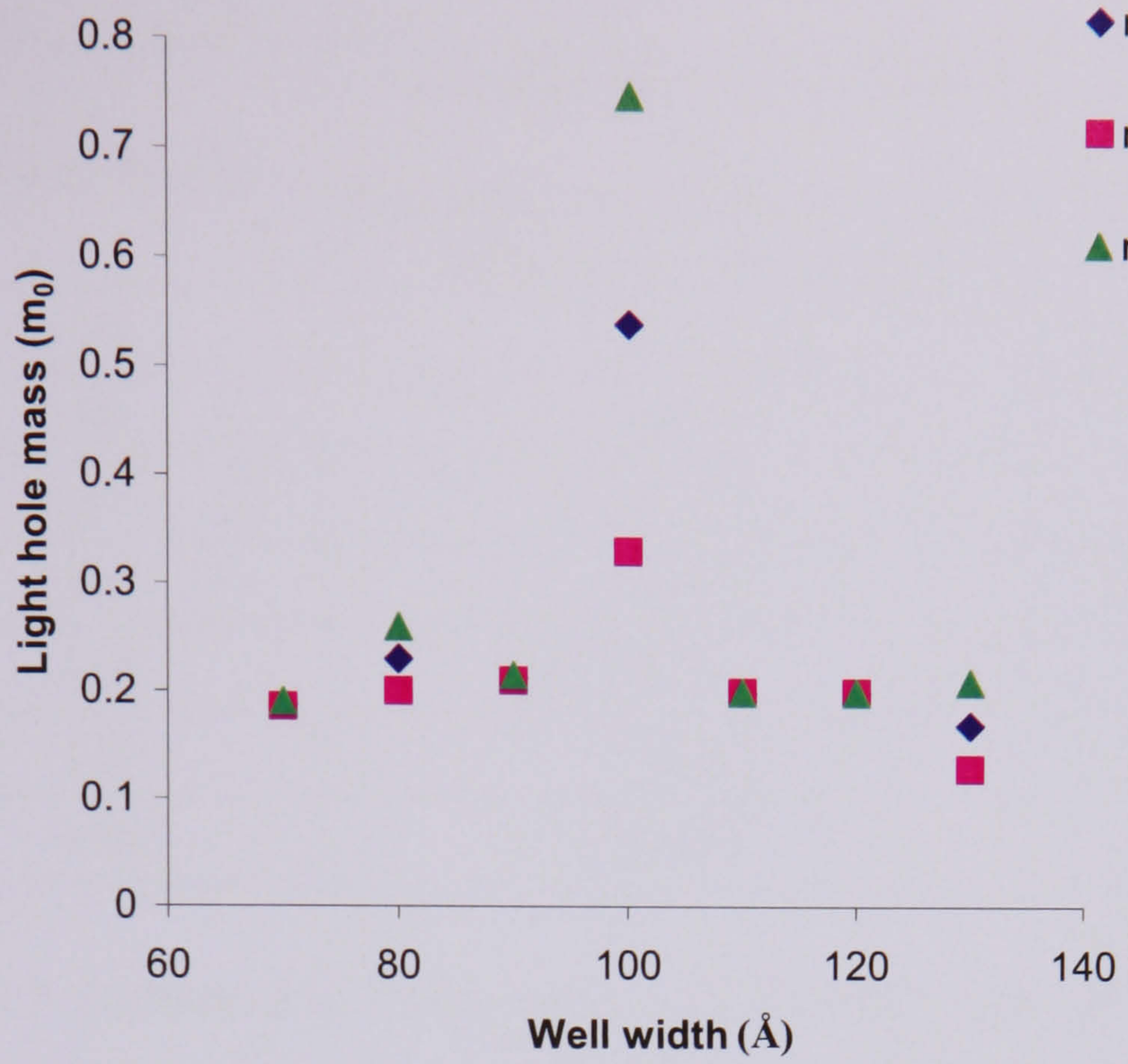

Figure 5.20: Relationship between average extracted light hole effective mass and well width for the first light hole states of a $In_{0.1}GaAs$ quantum well enclosed by a $GaAsP_{0.09}$ barrier.

The relationship between average extracted in-plane effective mass and well width is displayed in Figure 5.20. Again, a non-monotonic relationship between the extracted mass and well width is observed, with the extract light hole mass being largest when the light hole sub-band is in close proximity to the third heavy hole sub-band (see Table 5.3), although, curiously the light hole mass corresponding to the smallest inter sub-band distance is relatively low, perhaps due to the influence of other, more distant heavy hole sub-bands.

Well width (Å)	Difference in energy between the first light hole sub-band and next nearest neighbour (meV)	Well behaved extracted effective mass?
70	10.56	Yes
80	18.70	Yes
90	11.97	Yes
100	4.01	No
110	2.70	Yes
120	8.26	Yes
130	14.00	Yes

Table 5.3: Difference in energy between the first light hole sub-band and the next nearest sub-band as a function of well width for a 80Å $In_{0.1}GaAs$ quantum well enclosed by a $GaAsP_{0.09}$ barrier.

Due to the lack of a clear relationship between the light hole extracted in-plane mass and either well depth or width the light hole in-plane mass is determined using the linear interpolation given in Equation 5.14.

Finally, the extracted and interpolated in-plane effective masses are used to calculate the reduced in-plane effective mass and incorporated into the quantum efficiency calculation in SOL. An overview of of this calculation is given in Figure 5.21

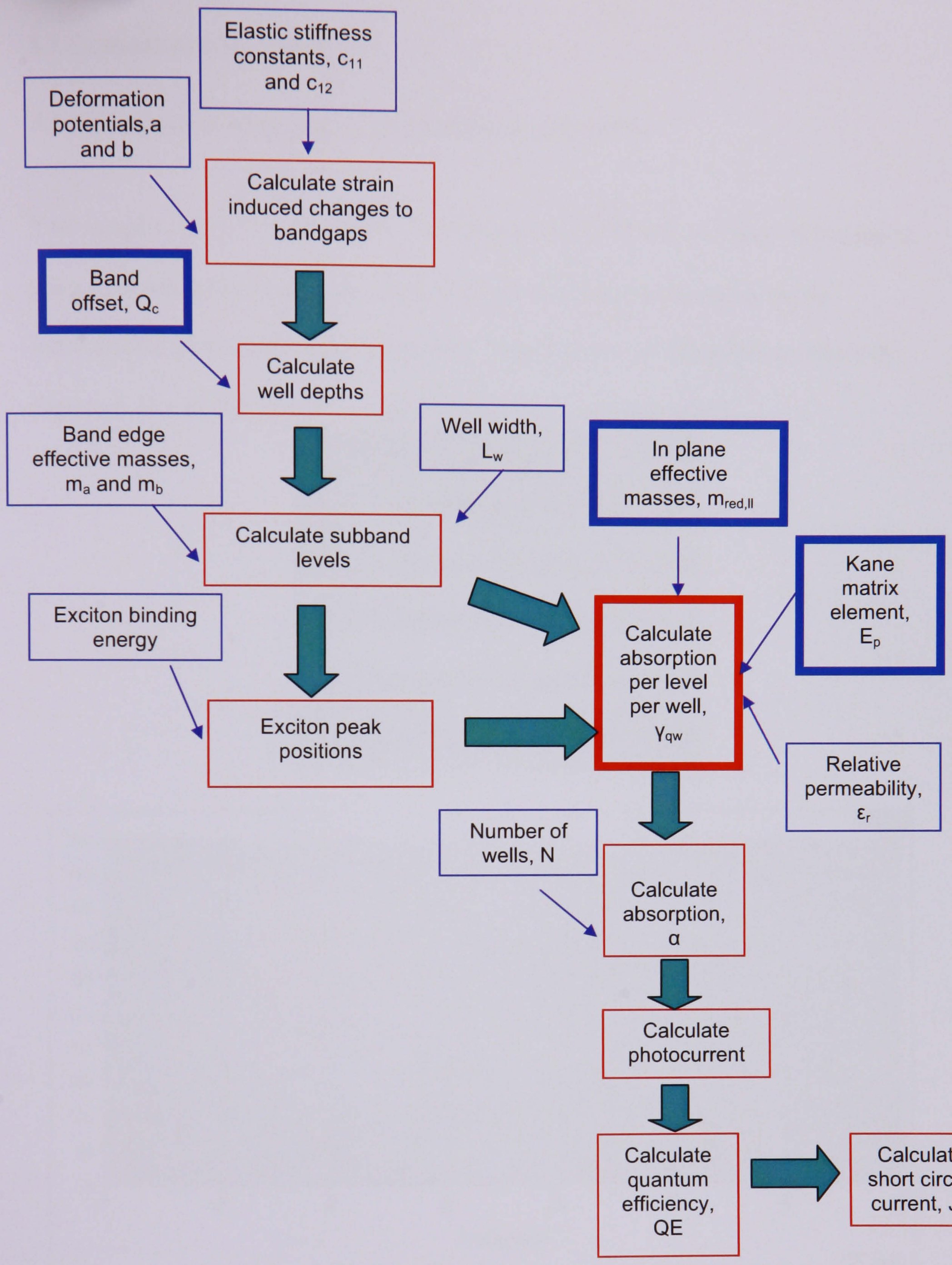

Figure 5.21: Overview of SOL. Input parameters are shown in blue boxes and calculations are displayed in red boxes. The parts of the program refined during this work are highlighted.

5.3 Evaluation of the model

5.3.1 Comparison of predicted and measured well widths

Two samples, Qt1840 (a 50 shallow well sample) and Qt1897B (a 5 deep well sample), were analysed at Bookham Laboratories Ltd. using TEM to permit an accurate measurement of the well and barrier widths. Images of the two samples are shown in Figures 5.22 and 5.23. For full sample compositions, see Appendix 1.

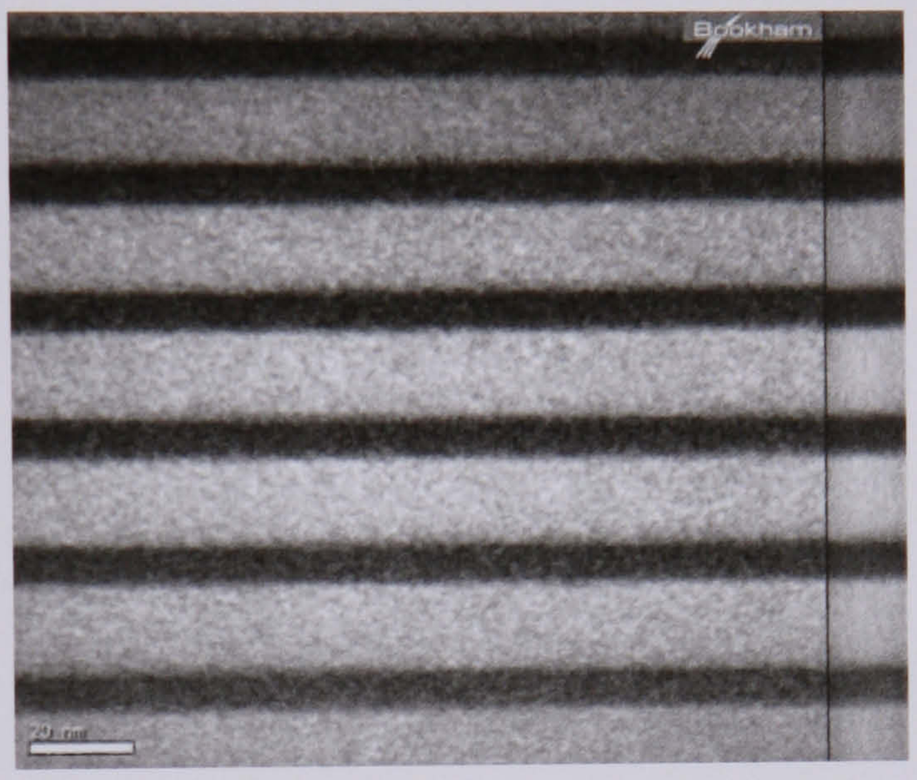

Figure 5.22 TEM and measured well and barrier widths for Qt1840

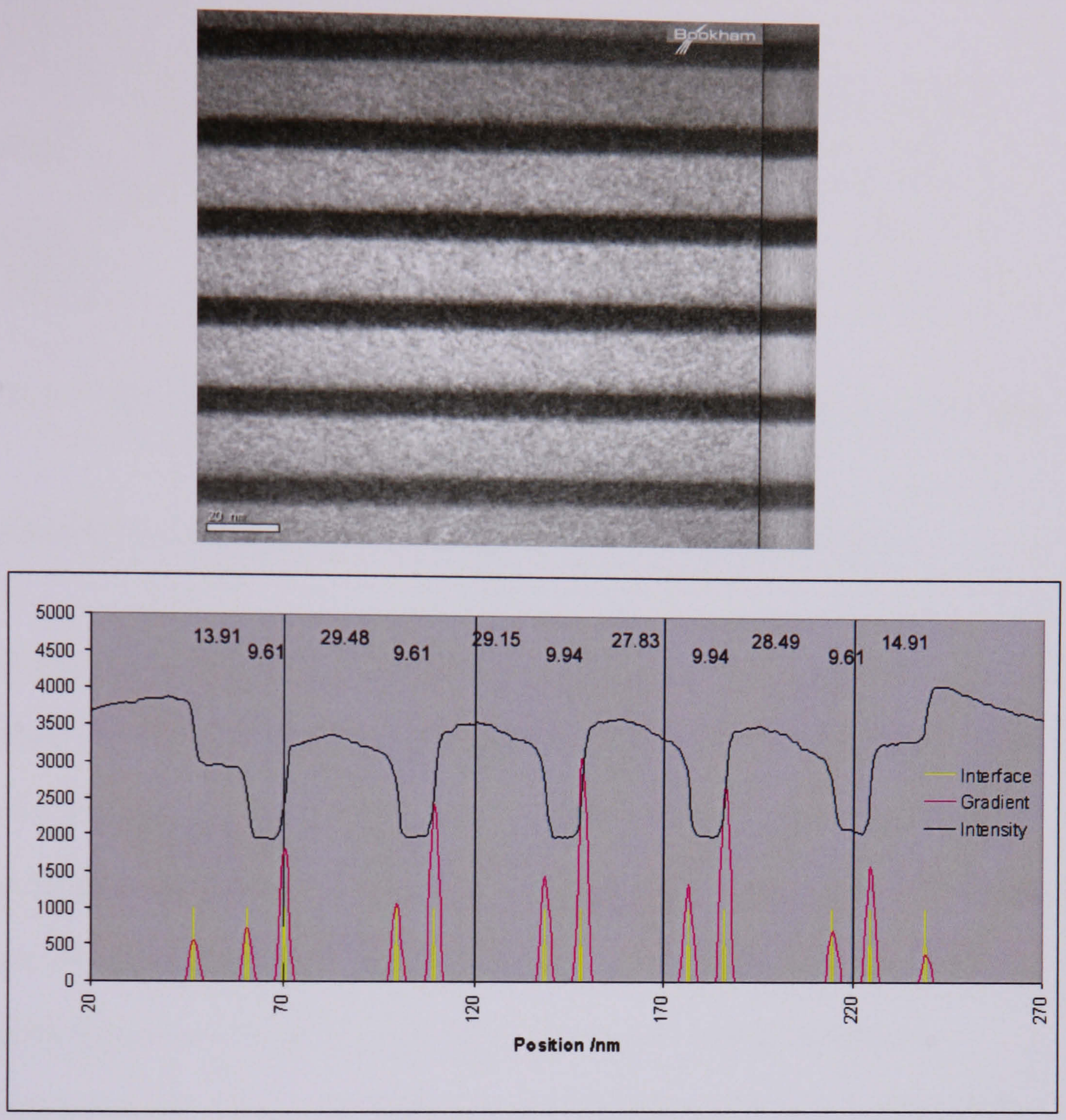

Figure 5.23 TEM and measured well and barrier widths for Qt1897B

First estimates of the well and barrier widths were obtain from values of the well/barrier period obtained using XRD and the fact that the well and barrier widths must satisfy strain balanced condition given in Equation 1.15. These estimates are then used as input parameters in SOL and refined to give the best possible fit to the exciton peak positions. These values are compared to the well and barrier widths obtained from the TEM scans in Table 5.4. Good agreement is observed between the predicted and measured values, although some discrepancy is unsurprising as the wells and barriers are not perfectly square. Also, there is a slight variation in well and barrier width across both samples.

Sample	Well width obtained using Sol (Å)	Well widths measured using TEM (Å)	Barrier width obtained using Sol (Å)	Barrier widths measured using TEM (Å)
Qt1840	83	79.6 - 83	157	167
Qt1897B	100	96.1-99.4	296	285-295

Table 5.4 Well and barrier widths of Qt1840 and Qt1897B obtained using SOL and measured using TEM.

5.3.2 Comparison of predicted and measured exciton binding energies

The binding energy of an exciton in a quantum well system can be measured experimentally as the difference in energy between the continuum edge and the centre of the exciton peak. An accurate value of the exciton binding energy is required to predict the position of the exciton peaks and hence control the device structure to make the most efficient use of the incident solar spectrum. As the e1-hh1 exciton peak is always the highest absorbing excitonic feature we are particularly interested in obtaining an accurate value of the binding energy for this transition. The effect of the e1-hh1 exciton peak position on device efficiency is highlighted in Chapter 3.

In this work we have determined an experimental value of 10.0 ±1.5 meV for the exciton binding energy for the e1-hh1 exciton for samples Qt1858D and Qt1838R (both 65 shallow well samples). The fact that a value for the exciton binding energy can be obtained from such large well number samples is indicative of excellent material quality. These values were determined from low temperature photocurrent scans to minimize thermal broadening of the exciton peaks (see Figure 5.23). To the author's knowledge this is the only measured value of the exciton binding energy for this material system.

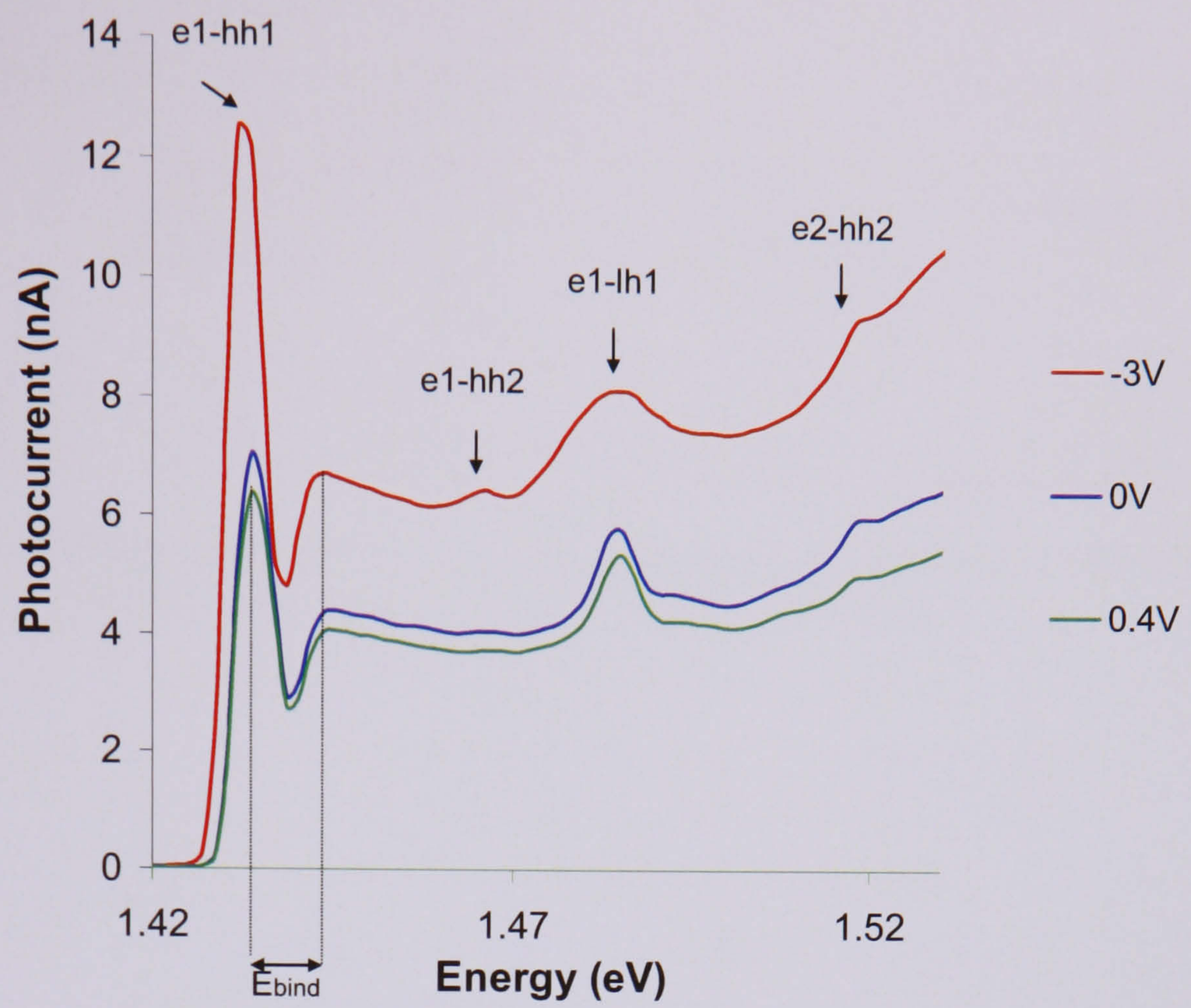

Figure 5.24. Photocurrent spectra of Qt1858D for a range of biases taken at 10K. The positions of a number of excitons are clearly visible. The small HWHM (3meV) of the e1-hh1 exciton peak is indicative of excellent material quality. The exciton binding energy (E_{bind}) of the e1-hh1exciton is measured to be 10.0 ±1.5meV

The calculated and measured values of the e1-hh1 exciton binding energy are displayed in Table 5.5. Broad agreement is observed between the predicted and measured values indicating that the simple, parameterised form of the exciton binding energy used in SOL is, for the purposes of this work, an adequate representation of the complex, many body nature of the exciton. The value of the exciton dimensionality is found to fall between that of a purely three dimensional and a purely two dimensional exciton (c.f. Equation 5.4) although the dimensionality of exciton becomes closer to the two dimensional limit as well indium content, and hence well depth and confinement, increase [12].

Sample	Well indium content (%)	Measured exciton binding energy (meV)	Predicted exciton binding energy (meV)	Dimensionality ν (meV)
Qt1858D	11	10.0±1.5	8.05	0.1
Qt1838R	12.5	10.0±1.5	8.72	0.15

Table 5.5: Measured and predicted exciton binding energies and exciton dimensionality for the e1-hh1 exciton of Qt1858D and Qt1838R

5.3.3 Comparison of measured and predicted quantum efficiency

Naturally, the most rigorous test of the quantum model is to compare measured and predicted quantum efficiencies. However, there is one complication that makes such a comparison non-trivial; the fact that a fraction of the light which reaches the back surface of the device, which is an annealed contact formed from an alloy of In and Ge stuck to a gold-loaded epoxy T05 header, is reflected back into the sample (see Figure 5.25). The nature of the back surfaces leads one to expect a significant variation of direct and diffuse reflectivity from sample to sample. Previous work has suggested that there is both a direct (normal incidence) and diffuse contribution to the back surface reflectivity, and estimated the direct back surface reflection at 30% and the diffuse rear surface reflection between 3.8% and 25%. When diffuse light is reflected at angles greater than the critical angle for the top surface the light makes repeated passes through the wells. [24].

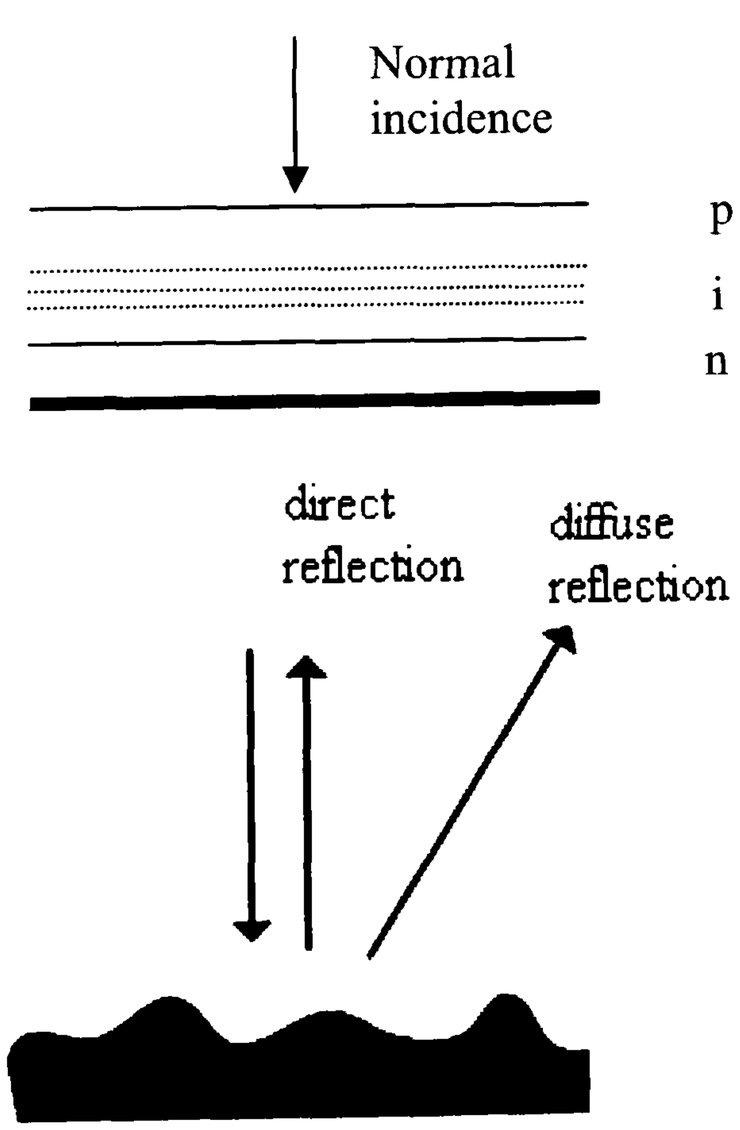

Figure 5.25: Schematic illustrating the diffuse and direct components to the back surface reflectivity (not to scale).

In order to compare SOL's prediction for the well absorption without any reflection from the back surface the model was compared with two strained InGaAs/GaAs samples, Qt957b and Qt957c (for sample details see Appendix 1), which had been processed with black paint on the back surface to remove as much direct and diffuse scattering as possible. The comparison between the predicted and measured quantum efficiencies is shown in Figure 5.26.

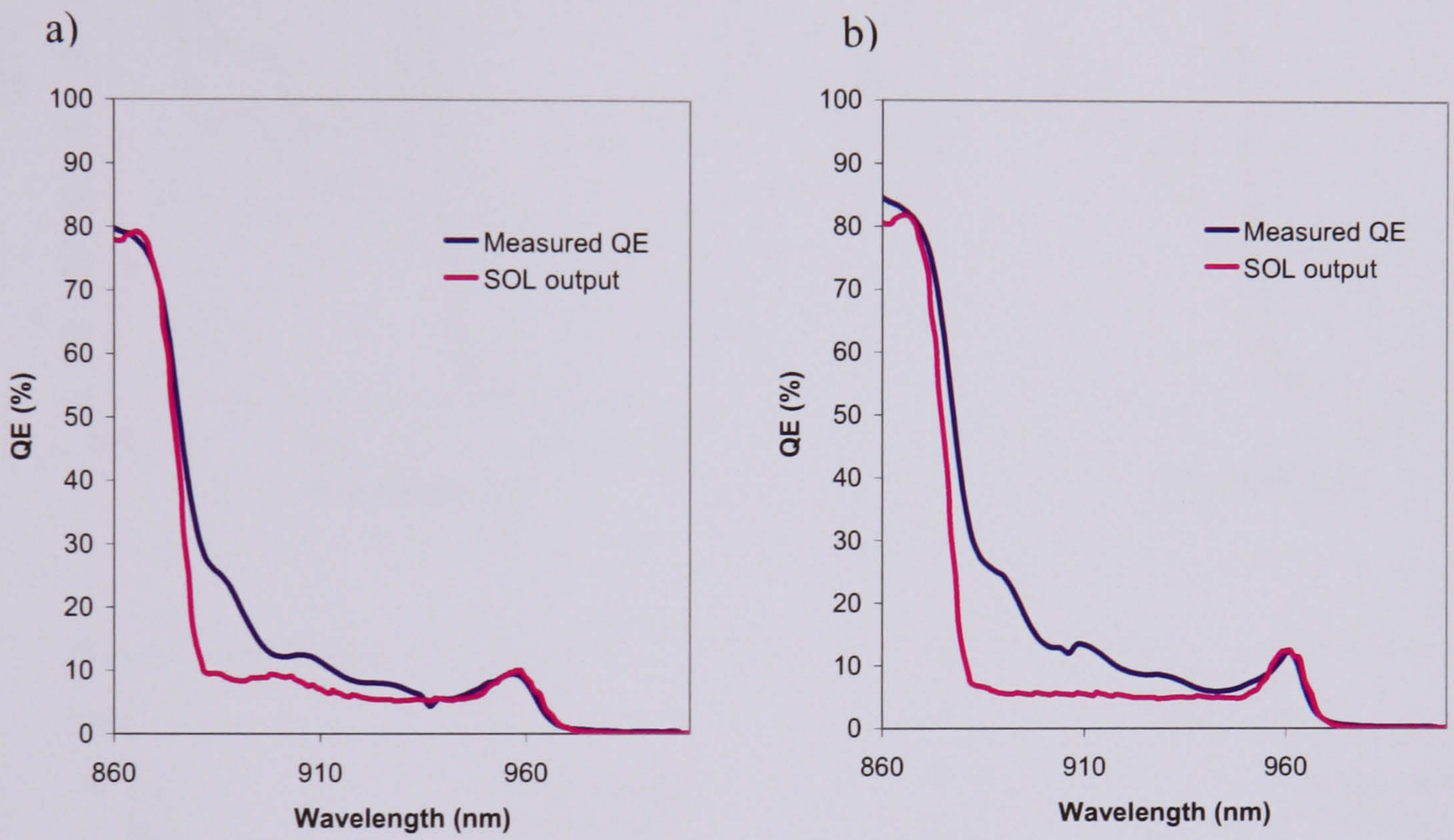

Figure 5.26 Predicted and measured quantum efficiencies for a) Qt957b and b) Qt957c. Good agreement is observed between the predicted and measured exciton peaks and e1-hh1 continuum level.

The model is able to accurately reproduce the e1-hh1 exciton peak and the first continuum level for these samples. It should be noted that, in contrast to earlier versions of SOL where the absorption per level per well was fitted, these predictions are absolute. The QE level depends strongly on the effective masses giving confidence in the approach described in Section 5.2.3. However, the features corresponding to transitions higher in the well are not so well described. This is unsurprising as the band offset and in-plane effective masses have yet to be rigorously examined for the

InGaAs/GaAs material system (in particular the light hole is unbound in this system) [9].

The quantum efficiencies of a number of standard processed samples are compared to those predicted using SOL (see Figure 5.27).

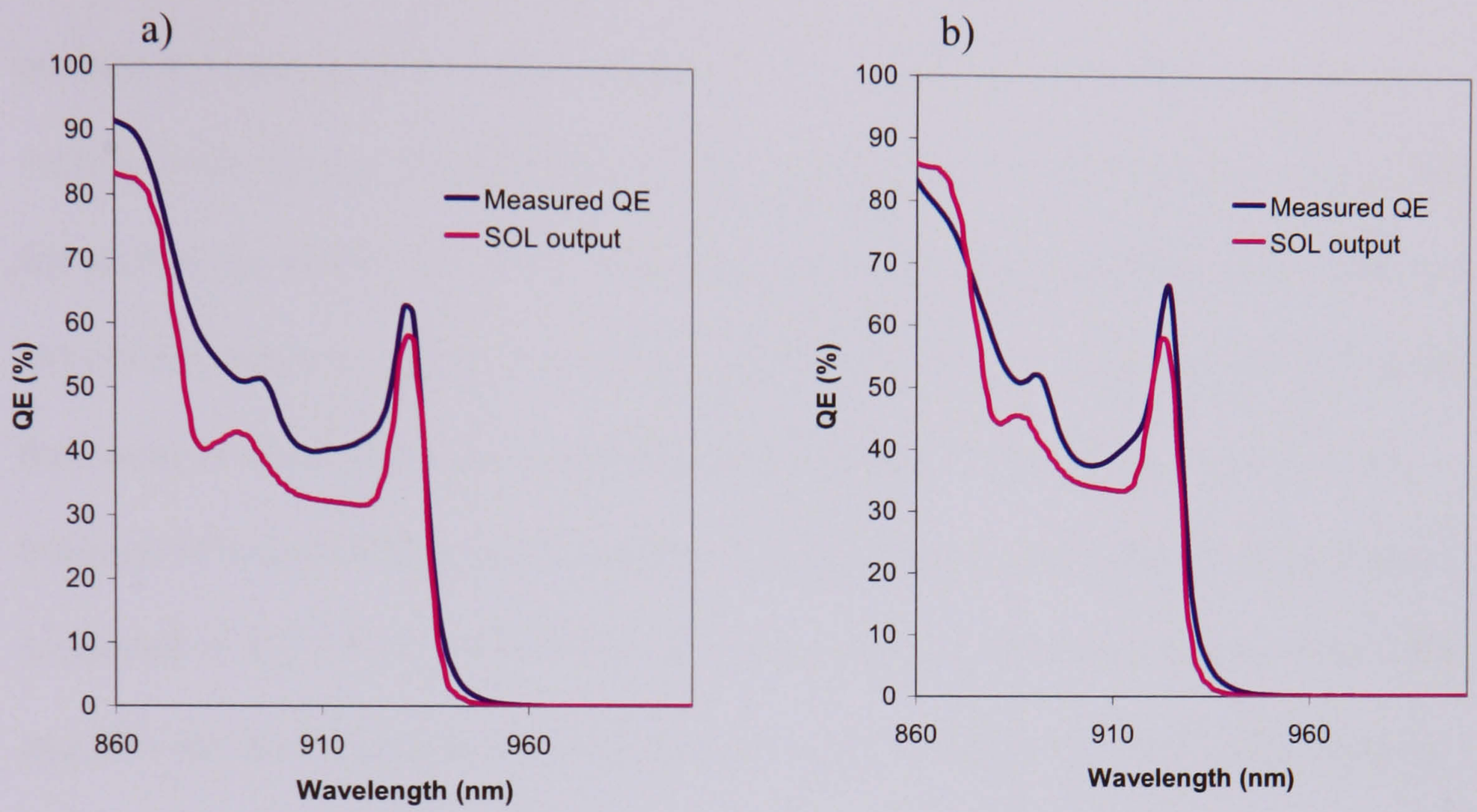

Figure 5.27: Measured and predicted quantum efficiencies of a) Qt1838R, b) Qt1858D, c) Qt1897AD and d) Qt1910U (see Appendix 1 for sample compositions). In all cases SOL underestimates the quantum efficiency due to the contribution of the reflection from the back surface to the QE.

Very good agreement is observed between the predicted and measured position of the exciton peaks, although naturally the experimental QE is higher than the predicted QE due to the unaccounted for reflections from the back surface. The slight discrepancy between the e1-lh1 exciton peak position predicted by SOL and the measured peak position in some samples is not unexpected and is likely to be due to the fact that the wells are non-square. The absorption at the first continuum level obtained from the SOL fits and the absorption determined from experimentally determined quantum efficiency have been compared for a number of strain-balanced samples and it has been found that the extent to which SOL underestimates the absorption at the first continuum level is between 34% and 55% for most samples, broadly consistent with the range of values suggested in Ref [19] of 30% for the direct back surface reflectivity and between 3.8% and 25% for the diffuse back surface reflectivity (see Figures 5.28 and 5.29). There is little variation in the ratio with either well number or Indium fraction, giving confidence in approach used here to determine the effective masses.

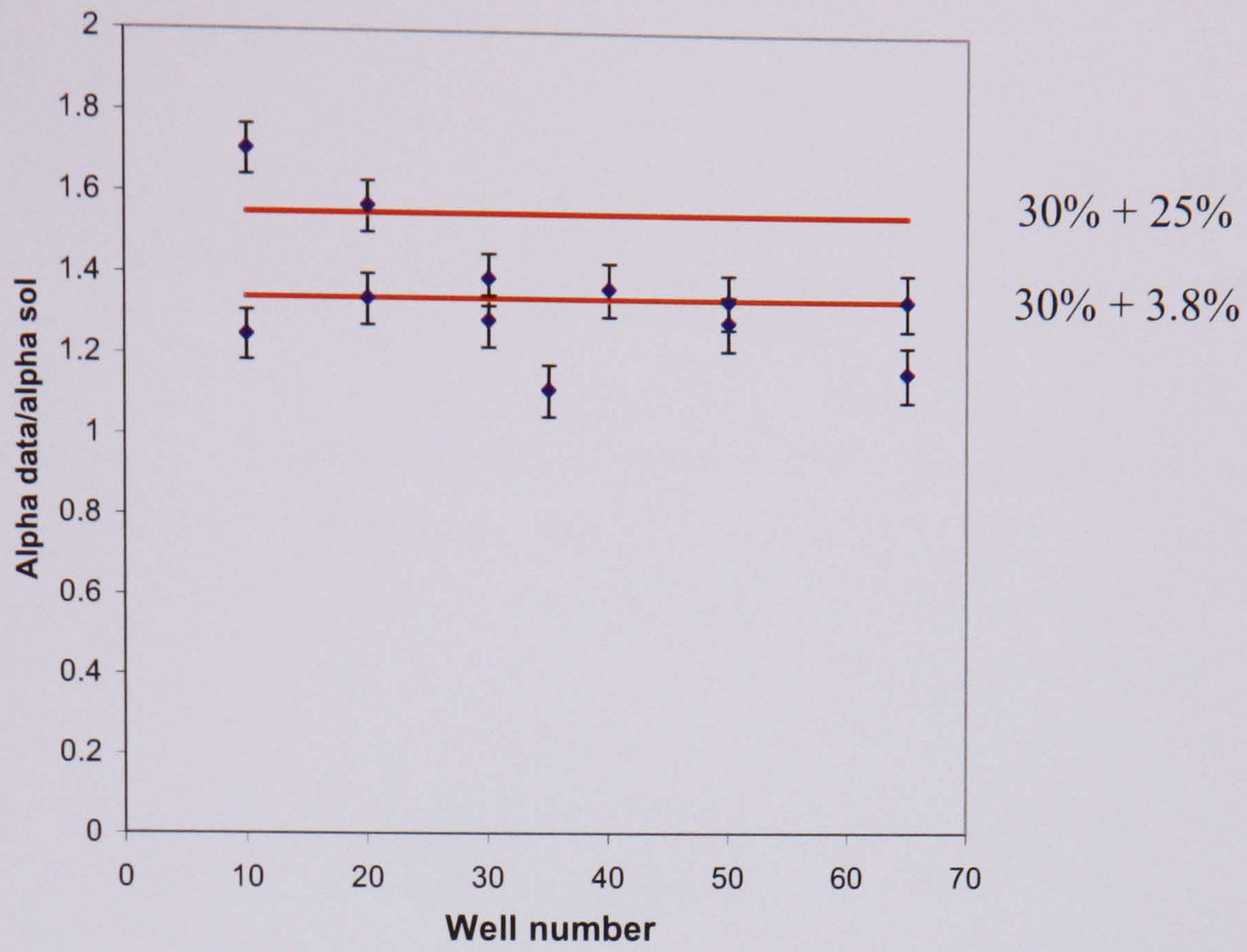

Figure 5.28 Ratio of experimentally determined absorption coefficient (alpha) to absorption coefficient determined from SOL predictions of quantum efficiency as a function of well number for a number of strain balanced samples. The red lines denote the range of values the ratio occupies assuming a direct back surface reflection of 30% and a diffuse back surface reflection of 3.8% and a direct back surface reflection of 30% and a diffuse back surface reflection of 25% as suggested in Ref [19].

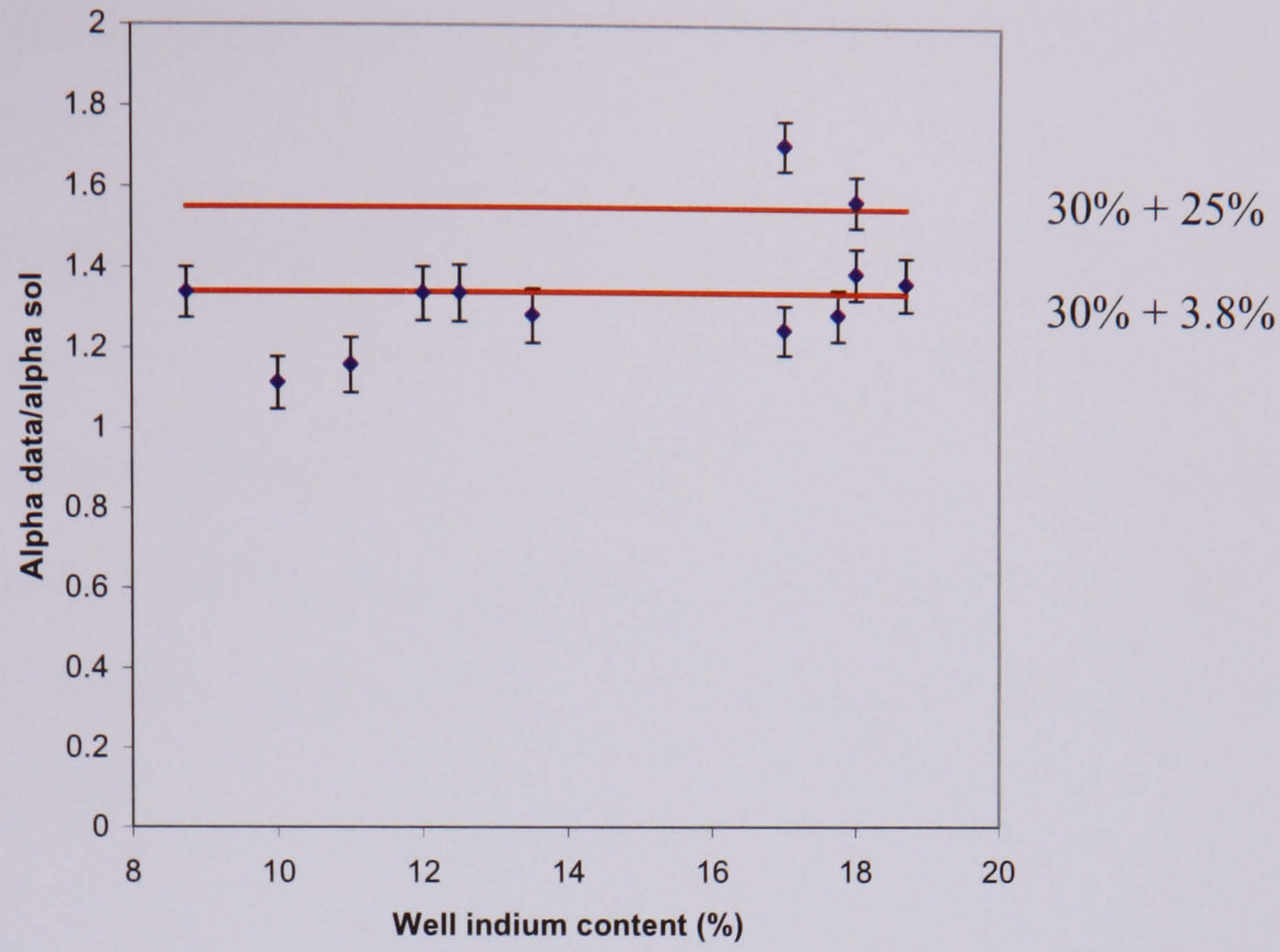

Figure 5.29: Ratio of experimentally determined absorption coefficient (alpha) to absorption coefficient determined from SOL predictions of quantum efficiency as a function of well indium content for a number of strain balanced samples. Again, the red lines denote the range of values the ratio occupies assuming a direct back surface reflection of 30% and a diffuse back surface reflection of 3.8% and a direct back surface reflection of 30% and a diffuse back surface reflection of 25% as suggested in Ref [19].

5.3.4 Structural optimisation and comparison of predicted and measured conversion efficiency

SOL has been used to project the efficiencies of a range of structures with different well widths and depths, with a view to finding an optimum structure for a SB-MQW solar cell. A barrier composition of $GaAsP_{0.12}$, a barrier width of 122.9Å and a band offset of 0.55 are assumed, incident spectrum is taken to be AM1.5D at 300 suns concentration (230100 Wm^{-2}) and the sample contains 65 wells. The predicted conversion efficiencies are shown in Figure 4.30

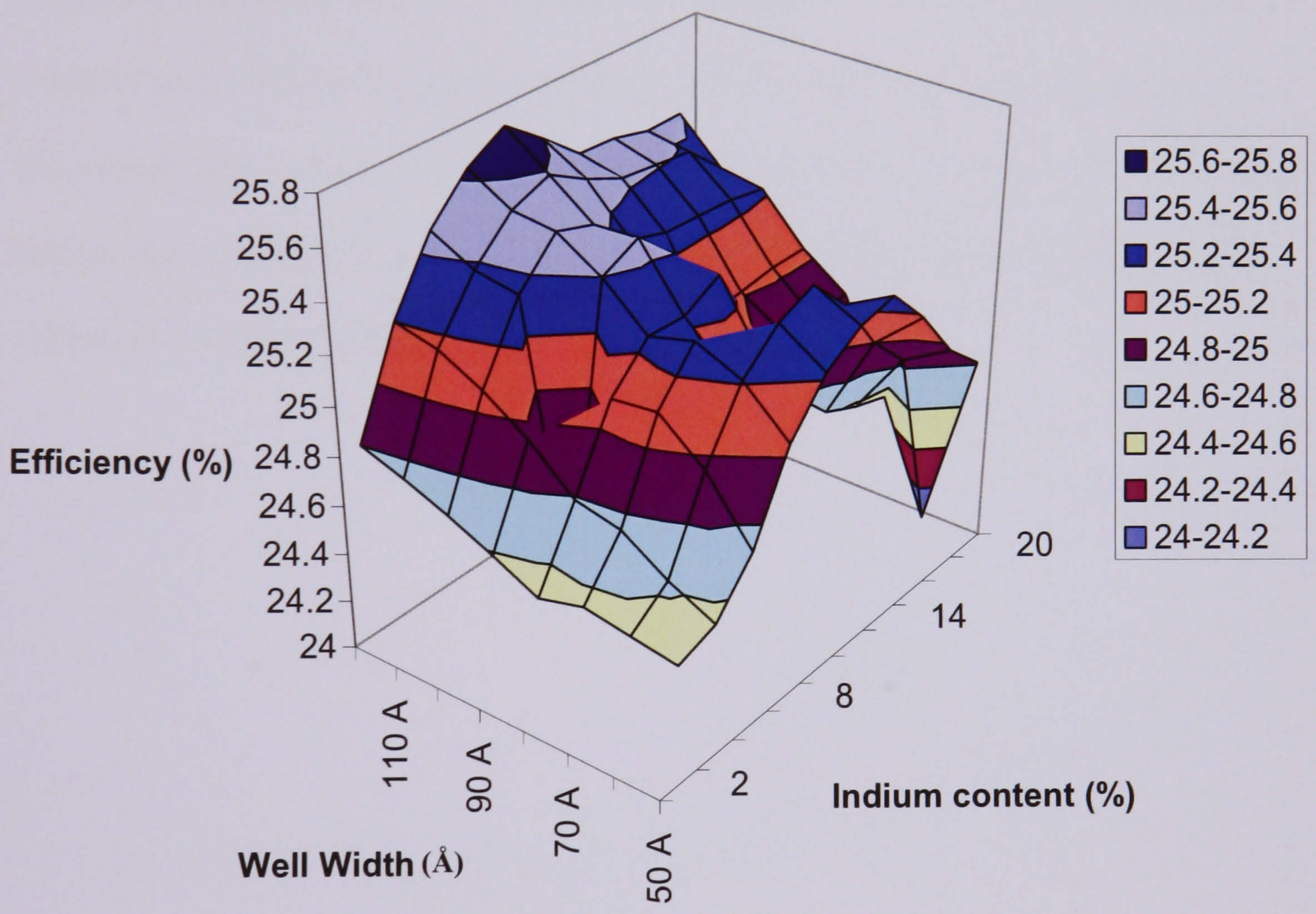

Figure 5.30: Conversion efficiencies predicted using SOL for a variety of well widths and depths. A barrier composition of $GaAsP_{0.12}$, a barrier width of 122.9Å and a band offset of 0.55 are assumed. The incident spectrum used is AM1.5D at 300 suns intensity (an incident power of 230100 Wm^{-2}) and the sample contains 65 wells.

The optimum well composition is found to be a 120Å well of $In_{0.1}GaAs$, which has a projected efficiency of 25.7% when illuminated by the AM1.5D spectrum at 300 suns intensity. For comparison, a GaAs p-i-n junction which has an equal i region width has a projected efficiency of 23.6%.

Additionally, the conversion efficiency for a concentrator version of sample TS98 (see Appendix 1 for full details) illuminated by the AM1.5D spectrum at 317 suns concentration predicted by SOL has been compared to the value obtained using independent measurements at the Fraunhofer Institute in Germany. The SOL prediction is obtained by fitting a measured quantum efficiency and dark current to obtain theoretical values for J_{sc} and V_{oc}. Good agreement is observed between the predicted and measured values, 25.3% and 25.7% respectively, giving added confidence in the refinements made to SOL.

5.4 Conclusion and further work

Substantial refinements have been made to the model of the quantum efficiency of the well region of multi-quantum well solar cells. A rigorous calculation of the strain bandgaps has been included into the model. The conduction band offset for the InGaAs/GaAsP material system has been determined by examining the splitting between the e1-hh1 and e1-lh1 exciton peak and comparing it to the splitting predicted for a range of values of conduction band offsets, obtaining a value of $Q_c = 0.53 \pm 0.05$. The binding energy for the e1-hh1 exciton has been measured for two samples with 65 wells and found to be 10.0 ± 1.5 meV. An absolute calculation of the quantum well absorption coefficient has been included and an extensive study of the in-plane mass of both the first heavy and light hole sub-bands has been undertaken. This study has provided a parameterization of the relationship between heavy hole in-plane mass and well indium content, while the light hole in-plane mass displays no clear relationship with either well depth or width. The new model has been tested in the following experimental situations:

1) The well and barrier widths predicted by the refined model are found to be broadly consistent with those obtained from TEM scans from two samples.

2) The exciton binding energy for the e1-hh1 exciton calculated using a simple parameterization is in broad agreement with the experimentally determined value.

3) Good agreement is seen between the absolute SOL prediction and the measured values of the quantum efficiencies at the e1-hh1 exciton peak and the level of the first continuum for two samples processed with black paint on the back surface to remove any back-surface reflections.

4) The predicted quantum efficiency is underestimated when compared to measured quantum efficiencies of samples which have undergone standard processing but the

level of underestimation observed for a number of strain-balanced samples is found to be broadly consistent with previous predictions of the magnitude of the back surface reflectivity.

5) The conversion efficiency of a sample predicted using SOL is compared to the value independently obtained at the Fraunhofer Institute. Good agreement is obtained between the two values (25.3% and 25.7% respectively for 317 suns AM1.5D). Additionally, a study of the projected conversion efficiencies for a range of quantum well structures containing 65 strain-balanced wells was undertaken and the optimum structure for illumination by the AM1.5G spectrum was found to a 120Å well of $In_{0.1}GaAs$. The conversion efficiency of this device was predicted to be 25.7%

This work identifies several promising avenues for further work. The effective mass study could be widened to include different barrier compositions and different values of the conduction band offset. It would also be useful to compare the measured quantum efficiency from strain-balanced samples processed with black paint on the back surface to the quantum efficiency predicted using SOL, and to the measured quantum efficiency of samples that have undergone standard processing to gain additional insight into the magnitude of the reflection from the back surface. Also, it would be appropriate to investigate cells grown on polished substrates (see section 3.2.3.2) as a means of increasing the amount of light entering the cell. Additionally, if material of sufficient quality becomes available, the heavy to light hole exciton peak splitting could be measured for more samples with a wider range of well indium fractions to obtain a better estimate of Q_c.

References

[1] J. Nelson et al. "Observation of Suppressed Radiative Recombination in Single Quantum Well p-i-n Diodes. **82** 12. p6240. 1997

[2] M. Fuher et al. "Quasi Fermi level splitting and evidence for hot carriers effects in strain-balanced quantum well concentrator solar cells at high bias." Proc. 21st European PV Solar Energy Conference, Dresden. 2006

[3] M. Paxman et al. "Modelling the spectral response of the quantum well solar cell." J. Appl. Phys. **74** (1). p614-621.1993

[4] J. Nelson. "Low-dimensional semiconductor structures." ed. K. Barnham and D. Vvedensky. Chapter 6. Cambridge University Press, 2001.

[5] J. Connolly et al. "Modelling Multi Quantum Well Solar Cell Efficiency", Proc. 17th European Photovoltaic Solar Energy Conference, Munich, Germany, pp 204-207.October 2001

[6] J Barnes et al. "Characterisation of GaAs/InGaAs quantum wells using photocurrent spectroscopy." J. Appl. Phys. **79**. p7775-7779. 1996

[7] J. Connolly et al. "Simulating multiple quantum well solar cells." Proc. 28th IEEE Photovoltaic Specialists Conference, Anchorage, Alaska, USA. p. 1304-1307. 2000.

[8]G. Bastard. "Wave mechanics applied to semiconductor heterostructures." Editions de Physique. 1988

[9] M. Cardona and P. Yu. "Fundamentals of semiconductors." Springer-Verlang. 1999

[10] J. Davies. "Low dimensional semiconductors: an introduction." Cambridge University Press. 1997

[11] P. Harison. "Quantum Wells, Wires and Dots: Theoretical and Computational Physics of Semiconductor Nanostructures, 2nd Edition." Wiley. 2005

[12] P.N. Stavrinou. "A study of InP based strained layer heterostructures." PhD thesis, UCL. 1995

[13] A. Khan et al. "Low-dimensional semiconductor structures." ed. K. Barnham and D. Vvedensky. Chapter 8. Cambridge University Press, 2001.

[14] J. Barnes et al. "Characterization of GaAs/InGaAs quantum wells using photocurrent spectroscopy." J. Appl. Phys. **79** (10). 1996.

[15]. S. Niki, et al. "Band-edge discontinuities in strained-layer $In_xGa_{1-x}As$ heterojunctions and quantum wells." Appl. Phys. Lett. **55** (13). 1989.

[16] A. Salokatve et al. "Room temperature photoconductivity of InGaAs/GaAs strained-layer superlattices." Appl. Phys. Lett. **58** (17). p1878. 1991.

[17] B. Jogai et al. "Valence band offset in strained $GaAsIn_xGa_{1-x}As$ superlattices". Appl. Phys. Lett. **59** (11). p1329. 1991.

[18] J. Reithmaier et al. "Band offset in elastically strained InGaAs/GaAs multiple quantum wells determined by optical absorption and electronic Raman scattering" Appl. Phys. Lett. **56** (6). p536. 1989.

[19] G. Duggan et al. "Reappraisal of the band-edge discontinuities at the AlxGa1-xAs-GaAs heterojunction." Phys. Rev. B. **32** (12). p8395. 1985.

[20] E. O'Reilly. "Valence band engineering in strained layer structures." Semicon. Sci. Tech. **4** p121-137. 1989

[21] P. J. Stevens et al. "Computer modelling of the electric field dependent absorption spectrum of multiple quantum well material." IEEE J. Quant. Elec., **24** p. 2007. 1988.

[22] I. Vurgaftman et al. "Band parameters for III-V semiconductors and their alloys." J. Appl. Phys. **89** (11). 2001.

[23] P. Yu and M. Cardona. "Fundamentals of Semiconductors." Spinger Verlag-Berlin. 1999

[24]. N. Ekins-Daukes. "An investigation into the efficiency of strained and strain-balanced quantum well solar cells." PhD thesis, Imperial College. 2000

5. Conclusions and further work

The inclusion of strain balanced InGaAs/GaAsP quantum wells into the intrinsic region of a GaAs p-i-n junction has been demonstrated to make more efficient use of the incident solar spectrum and hence increase device efficiency. In this thesis a number of experimental and modelling studies have been undertaken to enable one to quantify the performance of the cell and to optimise its efficiency.

In Chapter 3 the optimum number of wells to include in such devices was explored using a pair of otherwise identical strain balanced multi quantum well solar cells, one containing 50 wells and the other 65 wells. The 65 well sample was projected to achieve a lower efficiency than the 50 well sample, suggesting that the optimum well number is between these two values. Additionally, a second 65 well sample containing shallower quantum wells was also characterised and found to have an equal conversion efficiency to the 50 well sample. This was due to the position of the e1-hh1 exciton peak of the sample, which corresponds to a region of higher intensity in the incident spectrum. Additivity (in which the light IV characteristics of the device are equal to the dark IV characteristics minus the short circuit current) was observed, demonstrating that it is possible to grow a 65 well multi-quantum well device without loss of field over the intrinsic region. It is planned to further investigate the optimum well number by growing and studying devices containing between 50 and 65 wells and to examine varying well number series of devices for several well and barrier compositions and widths.

Additionally, devices grown using a novel growth precursor, tertiary butyl arsine (TBAs), in place of the conventional arsine as a source of arsenic were studied. A p-i-n solar cell grown using TBAs was found to display comparable projected conversion efficiency to a control device grown using arsine, while the dark current of the device

grown using TBAs was significantly lower than that of the control cell. This suggests that TBAs may be used as a substitute for arsine in the growth process without sacrificing device quality and may even have beneficial effects. It is planned to grow a number of strain balanced multi quantum well solar cells using TBAs to explore this hypothesis.

A two component model of the radiative dark current of SB-MQW solar cells is outlined in Chapter 4, with one component arising from radiative recombination in the wells and the other from the Ideal Shockley current. Good agreement was observed between the output of this model and experimentally determined intercepts of the $n_1 = 1$ dark current. The radiative dark current arising from recombination in the wells is found become increasingly dominant as the wells grow deeper. It is hoped that the work documented in Chapter 4 will be revised using the updated model for device absorption detailed in Chapter 5. It would also be useful to include the more accurate insight into device composition obtained using the new model for strain bandgaps and confined states. The comparison between the $n_1 = 1$ intercepts obtained from fitting experimental results and those predicted by the model could be included to include a larger number of devices with a greater range of well numbers and depths. It would also be interesting to determine whether the QW radiative fraction of the $n_1 = 1$ dark current increases further towards unity as well depth continues to increase.

In order to fabricate devices of the highest possible efficiency it is essential to be able to model the quantum efficiency of the quantum well region of SB-MQW solar cells. Several fundamental refinements to the existing quantum efficiency model SOL are detailed in Chapter 5. Firstly, a rigorous calculation of the strained band-gaps was introduced. Secondly, a value for the conduction band offset for the InGaAs/GaAsP material system was determined by calculating the difference in energy between the

heavy and light hole confined states for a number of band offsets and comparing these values to the distance between the e1-hh1 and e1-lh1 exciton peaks recorded using low temperature photocurrent measurements. A value was obtained of $Q_c = 0.53 \pm 0.03$.

It is planned to widen this study to include a larger number of samples containing a wider range of indium compositions to obtain a more accurate value of Q_c.

An absolute calculation for the absorption coefficient of the quantum wells was incorporated into the model and a study of the valence band in-plane effective mass undertaken. In this work the E-k dispersions along the <10> and <11> directions for quantum wells of varying widths and depths are obtained using a multiband **k.p** model. A parabola of equivalent enclosed area (and hence equivalent density of states) is then fitted to the calculated dispersion for the first heavy and light hole subbands and a value for the in-plane effective mass extracted from the fitted curve, with an average mass calculated from the masses obtained along the two different directions. This average extracted in-plane mass is then compared to the in-plane mass obtained by an interpolation of the confinement direction masses.

The extracted heavy hole mass is seen to decrease with increasing well indium content and also displays a weak dependence on well width. The light hole extracted in-plane mass displays a non-monotonic relationship with well depth and well width due to its close proximity to other sub-bands that makes the dispersion highly non-parabolic. Both the heavy and light hole extracted masses are significantly different to those obtained using the interpolation of confinement direction masses, with the heavy hole mass being up to five times heavier and the light hole mass being up to ten times heavier.

The relationship between the average in-plane effective mass and well indium content is modelled as a polynomial relationship. The weak dependence of heavy hole mass and well width is neglected to retain computational efficiency. Due to the lack of a clear relationship between the light hole effective mass and both well depth and width the

light hole in-plane mass is calculated from the interpolation of confinement direction masses.

The model was tested against experimental data with the following results:

1) The well and barrier widths obtained using SOL for two strain balanced samples were found to be broadly consistent with those measured using TEM.

2) The exciton binding energy for the e1-hh1 exciton calculated using a simple parameterization is in broad agreement with the experimentally determined value.

3) The model was used to make absolute predictions for the quantum efficiencies of strained InGaAs/GaAs samples processed with black paint on the back surface to remove any reflection for the gold epoxy layer at the rear contact. Excellent agreement was observed between the predicted and measured e1-hh1peaks and continuum levels.

4) The model was used to fit a large number of strain balanced samples and the absolute prediction was found to underestimate the absorption in these devices by between ~34% and ~55%, an amount consistent with previous work that suggested a direct back surface reflectivity of 30% and a diffuse back surface reflectivity of between 3.8% and 25%. No large trends in this ratio with well number or indium fraction were observed giving confidence in the procedure to extract the effective masses.

5) The conversion efficiency of a sample predicted using SOL is compared to the value independently obtained at the Fraunhofer Institute. Good agreement is obtained between the two values (25.3% and 25.7% respectively for 317 suns AM1.5D).

Additionally, a study of the projected conversion efficiencies for a range of quantum well structures was undertaken and the optimum structure for illumination by the AM1.5D spectrum was found to be a 120Å well of $In_{0.1}GaAs$ at 300 suns concentration.

It is planned further explore the validity of the model by processing several strain-balanced InGaAs/GaAsP samples with black paint on the rear surface and comparing the measured quantum efficiencies of these samples to those predicted using the model. Finally, it is proposed to extend the effective mass study by examining InGaAs quantum wells enclosed by GaAsP barriers of differing compositions and exploring the effect of changes in band offset on the in-plane effective mass of the heavy and light hole sub-bands.

Appendices

A1. Sample compositions

Qt1747C

Layer	No of repeats	Width (nm)	Composition	Dopant and Doping level (m^{-3})
Window	1	43	$Al_{0.80}GaAs$	Zn 1×10^{19}
Emitter	1	500	GaAs	C 8.5×10^{17}
½ barrier	30	14.7	$GaAsP_{0.11}$	
Well	30	10	$In_{0.185}GaAs$	
½ barrier	30	14.7	$GaAsP_{0.11}$	
Base	1	500	GaAs	Si 2.4×10^{17}

Qt1838R

Layer	No of repeats	Width (nm)	Composition	Dopant and Doping level (m^{-3})
Window	1	30	$Al_{0.80}GaAs$	C 2×10^{19}
Emitter	1	500	GaAs	C 2×10^{18}
½ barrier	65	8.7	$GaAsP_{0.11}$	
well	65	8.3	$In_{0.125}GaAs$	
½ barrier	65	8.7	$GaAsP_{0.11}$	
Base	1	3000	GaAs	Si 4×10^{17}
Base	1	300	GaAs	Si 1×10^{18}

Qt1840

Layer	No of repeats	Width (nm)	Composition	Dopant and Doping level (m^{-3})
Window	1	30	$Al_{0.80}GaAs$	C 2×10^{19}
Emitter	1	500	GaAs	C 2×10^{18}
½ barrier	50	7.4	$GaAsP_{0.11}$	
well	50	8.3	$In_{0.125}GaAs$	
½ barrier	50	7.4	$GaAsP_{0.11}$	
Base	1	3000	GaAs	Si 4×10^{17}
Base	1	300	GaAs	Si 2×10^{18}

Qt1858D

Layer	No of repeats	Width (nm)	Composition	Dopant and Doping level (m^{-3})
Window	1	43	$Al_{0.80}GaAs$	C 2×10^{19}
Emitter	1	400	GaAs	C 2×10^{18}
½ barrier	65	7.9	$GaAsP_{0.11}$	
well	65	8.8	$In_{0.11}GaAs$	
½ barrier	65	7.9	$GaAsP_{0.11}$	
Base	1	2000	GaAs	Si 4×10^{17}
Base	1	300	GaAs	Si 1×10^{18}

Qt1897BD

Layer	No of repeats	Width (nm)	Composition	Dopant and Doping level (m^{-3})
Window	1	4	$Al_{0.80}GaAs$	C 2×10^{19}
Emitter	1	500	GaAs	C 2×10^{18}
½ barrier	5	14.8	$GaAsP_{0.10}$	
well	5	10.0	$In_{0.17}GaAs$	
½ barrier	5	14.8	$GaAsP_{0.10}$	
Base	1	2000	GaAs	Si 4×10^{17}
Base	1	300	GaAs	Si 1×10^{18}

Qt1228 and Gacell

Layer	Width (nm)	Composition	Dopant and Doping level (m^{-3})
Window	41	$Al_{0.58}GaAs$	Zn 1×10^{19}
Emitter	500	GaAs	Zn 1×10^{18}
Intrinsic	1068	GaAs	Zn 2×10^{18}
Base	2000	GaAs	$< 1\times 10^{14}$
Buffer	300	GaAs	Si 1.5×10^{17}

Qt957b and Qt957c

Layer	No of repeats	Width (nm)	Composition	Dopant and Doping level (m^{-3})
Window	1	43	$Al_{0.80}GaAs$	C 2×10^{18}
Emitter	1	500	GaAs	C 2.6×10^{18}
½ barrier	10	23.8	GaAs	
well	10	10.0	$In_{0.145}GaAs$	
½ barrier	10	23.8	GaAs	
Base	1	1686	GaAs	Si 1.5×10^{17}

TS98

Layer	No of repeats	Width (nm)	Composition	Dopant and Doping level (m^{-3})
Window	1	43	$Al_{0.80}GaAs$	C 2×10^{18}
Emitter	1	150	GaAs	C 1.8×10^{18}
½ barrier	50	8.8	$GaAsP_{0.09}$	
well	50	9.5	$In_{0.115}GaAs$	
½ barrier	50	8.8	$GaAsP_{0.09}$	
Base	1	2000	GaAs	Si 2×10^{17}
Buffer	1	100	GaAs	> Si 2×10^{17}

A2. Material Parameters

Unless otherwise stated all parameters are taken from Reference [1]

Parameter	$In_xGa_{1-x}As$	$GaAs_{1-y}P_y$
Lattice constant a_0 (nm)	5.6533 + 0.40573x	5.6533×(1-y) + 5.4512y
c_{11} (10^{11} dyn/cm^2)	11.88 -3.55x	1.188×(1-y) + 1.412y
c_{12} (10^{11} dyn/cm^2)	5.38 - 0.85x	0.538×(1-y) + 0.6253y
a_{gap} (eV)	-8.3768 + 1.7686x	-8.3768×(1-y) -10.9y
b (eV)	-1.7 - 0.1x	-1.7×(1-y)-1.5y
Δ (eV)	0.341 - 0.09x + 0.14x^2	0.341×(1-y)+ 0.23y
γ_1	6.85×(1-x) + 19.67x	6.85×(1-y)+ 4.2y
γ_2	2.1× (1-x) + 8.37x	2.1×(1-y)+ 0.98y
Bulk bandgap E_g (eV)	1.424 - 1.5x+ 0.4x^2	1.424×(1-y)+ 2.74y
Kane Matrix element E_P (eV) [2]	28.8-6.6x	n/a
Relative permittivity ε_r [3]	13.1×(1-x) + 15.1x	13.1×(1-x) + 11.1x

[1] Landolt and Boernstien. New Series III, **17a** 1982

[2] I. Vurgaftman et al. "Band parameters for III–V compound semiconductors and their alloys" J. App. Phys. **89** (11). 2001

[3] F. Blatt. "Modern Physics" McGraw-Hill. 1992

A3. Derivation of the density of states in three and two dimensions

The derivation of the density of states for a bulk semiconductor and a quantum well is reviewed in this section following the approach in Reference 1 and 2.

The density of states is defined as the number of solutions to the Schrödinger equation per unit volume per unit energy.

Consider an electron confined within a cube of side L. The allowed wavenumbers are

$$k_x = \frac{n_x \pi}{L}\,;\, k_y = \frac{n_y \pi}{L}\,;\, k_z = \frac{n_z \pi}{L}\,; \tag{A3.1}$$

The volume of a single k state is thus

$$V_k = \left(\frac{\pi}{L}\right)^3 \tag{A3.2}$$

The volume of two spherical shells of radii k and k+dk is thus

$$V_{shell} = 4\pi k^2 dk \tag{A3.3}$$

The total number of states in the shell, g(k)dk is thus

$$g(k)dk = \frac{k^2 L^3 dk}{\pi^2} \tag{A3.4}$$

In obtaining Equation A3.4 a factor of 2 has been included to account for the twofold spin degeneracy of each electron state. A factor of 1/8 is also included as only positive values of k_x, k_y and k_z are considered [2].

To find the total states per unit energy we use the relationship

$$k = \left(\frac{2mE}{\hbar^2}\right)^{\frac{1}{2}} \tag{A3.5}$$

Differentiating with respect to E gives

$$dk = \left(\frac{2mE}{\hbar^2}\right)^{-\frac{1}{2}} \frac{m}{\hbar^2} dE \tag{A3.6}$$

Dividing by L^3 to obtain the number of states per unit energy per unit volume we find

$$g(E)dE = \frac{1}{2\pi^2}\left(\frac{2m^*}{\hbar^2}\right)^{\frac{3}{2}} E^{\frac{1}{2}} dE \tag{A3.7}$$

To derive the density of states for a two dimensional system a similar procedure is required, this time finding the number of solutions to the Schrödinger equation per unit area per unit energy

Consider an electron confined within a square of side L. The allowed wavenumbers are

$$k_x = \frac{n_x \pi}{L} ; k_y = \frac{n_y \pi}{L} \tag{A3.8}$$

The area of a single k state is thus

$$V_k = \left(\frac{\pi}{L}\right)^2 \tag{A3.9}$$

The area between two rings of radii k and k+dk is

$$A_{circle} = 2\pi kdk \tag{A3.10}$$

The total number of states in the ring, g(k), is thus

$$g(k) = \left(\frac{2mE}{h^2}\right)^{\frac{1}{2}} \left(\frac{2mE}{h^2}\right)^{-\frac{1}{2}} \frac{mL^2}{\pi\hbar^2} \tag{A3.11}$$

As before, in obtaining Equation A3.11 a factor of 2 has been included to account for the twofold spin degeneracy of each electron state. A factor of 1/4 is also included as only positive values of k_x and k_y are considered [2].

Again, finding dN/dE and then dividing by L^2L_w (where L_w is the well width) to obtain the number of states per unit energy per unit volume

$$\frac{dE}{dNdV} = \frac{m^*}{\pi\hbar^2 L_w} \tag{A3.12}$$

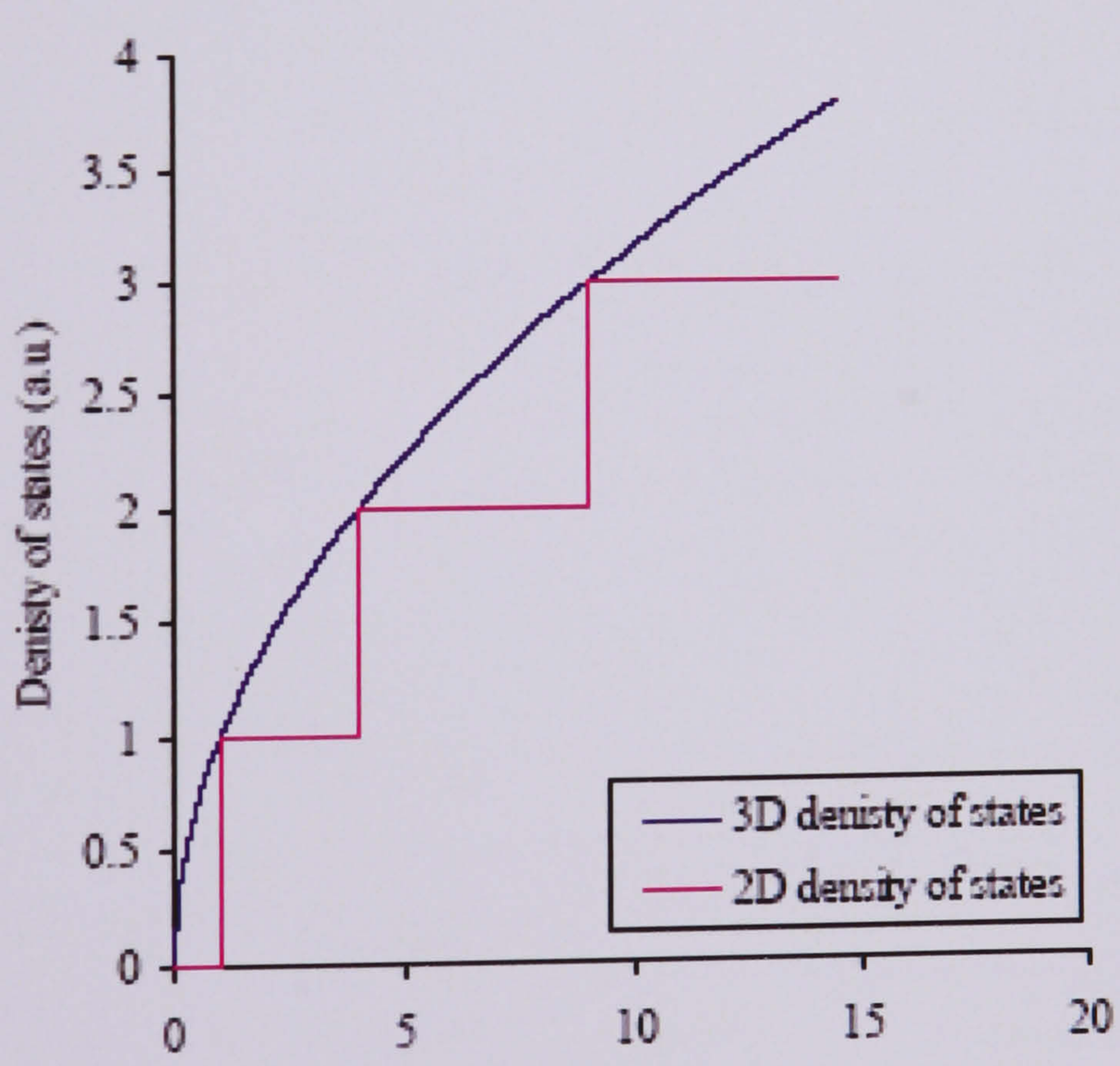

Figure A.1: The density of states for a bulk semiconductor and a quantum well system [3].

The density of states for a quantum well structure is hence independent of energy (above a threshold level) whereas the density of states of a bulk semiconductor varies with $E^{1/2}$. In a two dimensional system the density of states resembles a series of steps, with each step corresponding to a single sub-band.

[1] http://britneyspears.ac/physics/dos/dos.htm. 2000
[2] Donald A. Neaman. "Semiconductor physics and devices: basic principles."McGraw- Hill Professional. 2003.
[3] Dave Bushnell. "Optimisation of strain-compensated multi-quantum well solar cells." PhD thesis, Imperial College London, 2003.

A4. Derivation of strained bandgaps

The derivation in this section follows the method detailed in Reference1.

The time-independent Schrödinger equation has the familiar solution

$$H\Psi(r) = E\Psi(r) \tag{A4.1}$$

where H is the Hamiltonian, $\Psi(r)$ the wavefunction and E the energy eigenvalue. Considering just the conduction, heavy hole, light hole and spin-orbit bands, the Hamiltonian for an unstrained semiconductor at k=0 is

$$H_{unstrained} = \begin{array}{c} \\ \text{cb} \\ \text{hh} \\ \text{lh} \\ \text{so} \end{array} \begin{array}{c} \begin{array}{cccc} \text{cb} & \text{hh} & \text{lh} & \text{so} \end{array} \\ \begin{bmatrix} E_g & 0 & 0 & 0 \\ 0 & 0 & 0 & 0 \\ 0 & 0 & 0 & 0 \\ 0 & 0 & 0 & -\Delta \end{bmatrix} \end{array} \tag{A4.2}$$

where E_g is the unstrained bandgap and Δ is the spin-orbit splitting [2] (see Figure 1.13 in Chapter 1).

To include the effects of strain a second component, $H_{strained}$, must be added to the unstrained Hamiltonian

$$H_{strained} = \begin{bmatrix} \delta E_h^c & 0 & 0 & 0 \\ 0 & \delta E_h^v - \frac{1}{2}\delta E_s & 0 & 0 \\ 0 & 0 & \delta E_h^v + \frac{1}{2}\delta E_s & -\sqrt{\frac{1}{2}}\delta E_s \\ 0 & 0 & -\sqrt{\frac{1}{2}}\delta E_s & \delta E_h^v \end{bmatrix} \tag{A4.3}$$

The hydrostatic shifts of the conduction and valence band energies are defined as

$$\delta E_h^c = a_c(2e_{ll} + e_{zz}) \tag{A4.3}$$

$$\delta E_h^v = a_v(2e_{ll} + e_{zz}) \tag{A4.4}$$

where a_c and a_v are the hydrostatic deformation potentials of the conduction and valence band and the in plane strain, $e_{\parallel}$, is given by

$$e_{ll} = \frac{a_0^s - a_0^{layer}}{a_0^{layer}} \tag{A4.5}$$

where a_o^s and a_o^{layer} are the lattice constants of the substrate and the strained layer respectively. The strain in the growth direction, e_{zz}, is given by

$$e_{zz} = -\frac{2c_{12}}{c_{11}} e_{ll} \tag{A4.6}$$

where c_{12} and c_{11} are the bulk elastic coefficients of the material.

The shear energy shift is defined as

$$\delta E_s = 2b(e_{ll} - e_{zz}) \tag{A4.7}$$

where b is the shear deformation potential.

The combined Hamiltonian of the strained semiconductor is now given by

$$H_{combined} = H_{strained} + H_{unstrained} \tag{A4.8}$$

To facilitate easier quantum well calculations a constant, H_{shift}, is added to $H_{combined}$ to give the final Hamiltonian , H_{fin}, such that the heavy hole bandedge is defined as the zero point of energy [1].

$$H_{fin} = H_{combined} + H_{shift} \tag{A4.9}$$

H_{shift} is defined as

$$H_{shift} = \left(\frac{1}{2}\delta E_s - \delta E_h^v\right) I \tag{A4.10}$$

where I is the identity matrix.

H_{fin} is now given by [3]

$$H_{fin} = \begin{bmatrix} E_g + \delta E_h^c - \delta E_h^v + \frac{1}{2}\delta E_s & 0 & 0 & 0 \\ 0 & 0 & 0 & 0 \\ 0 & 0 & \delta E_s & -\sqrt{\frac{1}{2}}\delta E_s \\ 0 & 0 & -\sqrt{\frac{1}{2}}\delta E_s & -\Delta + \frac{1}{2}\delta E_s \end{bmatrix} \tag{A4.11}$$

we now define

$$\delta E_h^{gap} = \delta E_h^c - \delta E_h^v \tag{A4.12}$$

and

$$\mathrm{E_{gs}} = \mathrm{E_g} + \delta E_h^{gap} + \frac{1}{2}\delta E_s \tag{A4.13}$$

Additionally

$$E_{so} = -\Delta + \frac{1}{2}\delta E_s \tag{A4.14}$$

The final Hamiltonian can thus be written as

$$H_{fin} = \begin{bmatrix} E_{gs} & 0 & 0 & 0 \\ 0 & 0 & 0 & 0 \\ 0 & 0 & \delta E_s & -\sqrt{\frac{1}{2}}\delta E_s \\ 0 & 0 & -\sqrt{\frac{1}{2}}\delta E_s & E_{so} \end{bmatrix} \quad \text{(A4.15)}$$

The strained conduction – heavy hole bandgap is thus given by

$$\mathrm{E_{conduction\text{-}hh}} = \mathrm{E_g} + \delta E_h^{gap} + \frac{1}{2}\delta E_s \quad \text{(A4.16)}$$

The light hole and spin-orbit terms give rise to the equation

$$(\delta E_s - E)(E_{so} - E) - \frac{1}{2}\delta E_s^2 = 0 \quad \text{(A4.17)}$$

or

$$E^2 - E(\delta E_s + E_{so}) - \frac{1}{2}\delta E_s^2 + \delta E_s E_{so} = 0 \quad \text{(A4.18)}$$

which can be solved using the standard solution to a quadratic equation to give

$$\mathrm{E_{conduction\text{-}lh}} = \mathrm{E_g} + \frac{\delta E_s + \delta E_{so}}{2} + \frac{1}{2}\left[3\delta E_s{}^2 - 2\delta E_s E_{so} + E_{so}{}^2\right]^{\frac{1}{2}} \quad \text{(A4.19)}$$

and

$$\mathrm{E_{conduction\text{-}so}} = \mathrm{E_g} + \frac{\delta E_s + \delta E_{so}}{2} - \frac{1}{2}\left[3\delta E_s{}^2 - 2\delta E_s E_{so} + E_{so}{}^2\right]^{\frac{1}{2}} \quad \text{(A4.20)}$$

[1] P.N. Stavrinou. "A study of InP based strained layer heterostructures." PhD thesis, UCL. 1995

[2] J. Nelson. "Low-dimensional semiconductor structures." ed. K. Barnham and D. Vvedensky. Chapter 6. Cambridge University Press, 2001.

[3] E. P. O'Reilly. "Valence band Engineering in Strained-Layer Structures." Semicon. Sci. Tech. **4** pp 121-137. 1989

A5. *Overview of* **k.p** *theory*

An in-depth discussion of **k.p** theory may be found in References 1- 4 so only a brief overview of the necessary background is given here.

The work outlined in this section follows the discussion in Reference 1.

Neglecting the effects of spin the Schrödinger equation may be written as

$$H_o\psi(r) = E\psi(r) \tag{A5.1}$$

where H_o is the unperturbed Hamiltonian which is given by

$$H_o = \left(\frac{\nabla^2}{2m_o} + V(r)\right) \tag{A5.2}$$

and $V(r)$ is the potential of the crystal and $\psi(r)$ is the carrier wavefunction, which may be expressed as

$$\psi(r)=F(r)U(r) \tag{A5.3}$$

where F(r) is the envelope function and U(r) is the Bloch function that has the same periodicity as the crystal lattice.

The envelope function may be expressed as a plane wave, thus

$$\psi(r)=e^{ikr}U(r) \tag{A5.4}$$

Substituting this into Equation A5.3 yields

$$\left(\frac{\nabla^2}{2m_o} + V(r) + \frac{\hbar}{m}k.p + \frac{\hbar^2k^2}{2m_o}\right)\psi(r) = E\psi(r) \tag{A5.5}$$

or

$$[H_o+W]U(r)=EU(r) \tag{A5.6}$$

where

$$W = \frac{\hbar}{m}k.p + \frac{\hbar^2k^2}{2m_o} \tag{A5.7}$$

The Bloch functions can now be treated as separate summations of near and far states

$$U(r) = \sum_n C_n |n\rangle + \sum_f C_f |f\rangle \qquad \text{(A5.8)}$$

Equation A5.6 now becomes

$$(H_o + W)\left[\sum_n C_n |n\rangle + \sum_f C_f |f\rangle\right] = E\left[\sum_n C_n |n\rangle + \sum_f C_f |f\rangle\right] \qquad \text{(A5.9)}$$

which can be rewritten as

$$\sum_n C_n [E_n - E|n\rangle + W|n\rangle] + \sum_f C_f [E_f - E|f\rangle + W|f\rangle] = 0 \qquad \text{(A5.10)}$$

Multiplying Equation A5.10 by n' and integrating over the unit cell gives

$$\sum_n C_n [E_n - E]\delta_{nn'} + \langle n'|W|n\rangle + \sum_f C_f \langle n'|W|f\rangle = 0 \qquad \text{(A5.11)}$$

as $\langle n' \| f\rangle = 0$

Multiplying Equation A5.10 by f' and integrating over the unit cell gives

$$\sum_n C_f [E_f - E]\delta_{f'f} + \langle f'|W|f\rangle + \sum_n C_n \langle f'|W|n\rangle = 0 \qquad \text{(A5.12)}$$

As $[E_f - E] >> \langle f'|W|f\rangle$ [5], Equation A5.12 can be approximated to

$$\sum_n C_f = \frac{-1}{[E_f - E]} \sum_n C_n \langle f'|W|n\rangle \qquad \text{(A5.13)}$$

Substituting this into Equation A5.11 gives

$$\sum_n C_n (E_n - E)\delta_{nn'} + \langle n'|W|n\rangle + \frac{\sum_f \langle f'|W|n\rangle\langle n'|W|f\rangle}{E - E_f} = 0 \qquad \text{(A5.14)}$$

which reduces to

$$\sum_n C_n (E_n - E)\delta_{nn'} + \langle n'|W|n\rangle + \frac{\langle n'|W\sum_f|f\rangle\langle f'|W|n\rangle}{E - E_f} = 0 \qquad \text{(A5.15)}$$

The wavefunction can thus be expressed in terms of the near set of bands which have been appropriately modified to included the effects of the far set of bands. The key point

to obtain from equation A5.15 is that the wavefunction and hence the dispersion thus depend on both the distance between the subbands and the interaction between them. In the model used to calculate the dispersions in this work the heavy and light hole bands are neglected, apart from the spin-orbit band, which is included in the calculation of the confined energy levels, as detailed in Appendix 3.

[1]G. Bastard. "Wave mechanics applied to semiconductor heterostructures." Editions de Physique. 1988

[2] M. Cardona and P. Yu. "Fundamentals of semiconductors." Springer-Verlang. 1999

[3] J. Davies. "Low dimensional semiconductors: an introduction." Cambridge University Press. 1997

[4] P. Harison. "Quantum Wells, Wires and Dots: Theoretical and Computational Physics of Semiconductor Nanostructures, 2nd Edition." Wiley. 2005

[5] P.N. Stavrinou, private communication. 2007

A5. Publication List

As first author

- "Spectral response and IV characteristics of large well number multi quantum well solar cells." Journal of Materials Science, 40 **6** (2005) p1445-1449

- "Strain balanced quantum well solar cells for high concentration applications" Proceedings of the 20th European Photovoltaic Solar Energy Conference and Exhibition, Barcelona (2005) p523-526

- "Modelling the confined states in multi quantum well solar cells" Proceeding of the IEEE 4th World Conference on Photovoltaic Energy Conversion, Hawaii (2006) p67-70

As contributing author

- M. Begotti et al. "Electrical and photoelectrical properties of a GaAs based p-i-n structure grown by MOVPE." Crystal Research and Technology. 40 (**10-11**) (2005) p1033-1038
- T. Tibbits et al. "Demonstration of additivity in strain-balanced quantum well solar cells and efficiency enhancement at high concentration." IEEE Photovoltaics Specialists Conference. (2005) p587-590
- D. Johnson et al. "Advances in Bragg stack quantum well solar cells." Solar Energy Materials and Solar Cells. 87 (1-4). (2005) p169-179
- M Mazzer et al. "Progress in quantum well solar cells." Thin Solid Films. 511 (2006) p76-83
- J. Roberts et al. "Strain-balanced MQW pin solar cells grown using a robot-loading showerhead reactor." J Crystal Growth. 298 (2007) p754-757

A6. List of symbols used in this thesis

a, b	deformation potentials
a_0	average lattice constant
$a_{1,2}$	lattice constant of layer
A_f	front surface area
A_b	back surface area
AM	air mass
$c_{11,\ 12}$	elastic stiffness constants
D_n	electron diffusion length
D_p	hole diffusion length
$\boldsymbol{e}$	polarisation vector
E_{bind}	exciton binding energy
E_e	confined energy of an electron
E_g	unstrained bandgap
E_{gs}	strained bandgap
E_h	hydrostatic shift
E_{hc}	confined energy of an electron
E_p	Kane matrix element
EQE	external quantum efficiency
E_s	shear shift
F	flux
FF	fill factor
$\boldsymbol{H}$	the Hamiltonain operator
IQE	internal quantum efficiency
J_{pc}	photocurrent
J_{sc}	short circuit current

L_n	electron diffusion length
L_p	hole diffusion length
L_w	well width
m_z	confinement direction effective carrier masses
m_{red}	reduced effective carrier mass
$m_{\parallel}$	inplane effective carrier mass
m_0	free mass of electron
N	well number
n_e	electron density
n	ideality factor
n_i	intrinsic carrier density
n_{n0}	equilbrium electron density in p layer
n_{p0}	equilbrium hole density in p layer
n_r	refractive index
Q_c	conduction band offset
p	hole denstiy
$\boldsymbol{p}$	momentum operator
R	reflectivity
R^*	effective Rydberg constant
R_0	Rydberg constant
$t_{1,2}$	layer thickness
V_{mp}	maximum power voltage
V_{oc}	open circuit voltage
α	absoprtion
Δ	spin orbit splitting

ΔE_f	quasi Fermi level separation
Γ	exciton oscillator strength
γ_{qw}	absorption per level per well
η	device efficiency
τ_n	electron lifetime
τ_p	hole lifetime
υ	exciton dimensionality parameter